

AD-A055 760

NAVAL RESEARCH LAB WASHINGTON D C

F/G 4/1

UHF SCINTILLATION CHARACTERISTICS AS OBSERVED FROM KEFLAVIK, IC--ETC(U)

FEB 78 J M GOODMAN, P L WATKINS, C G MYERS

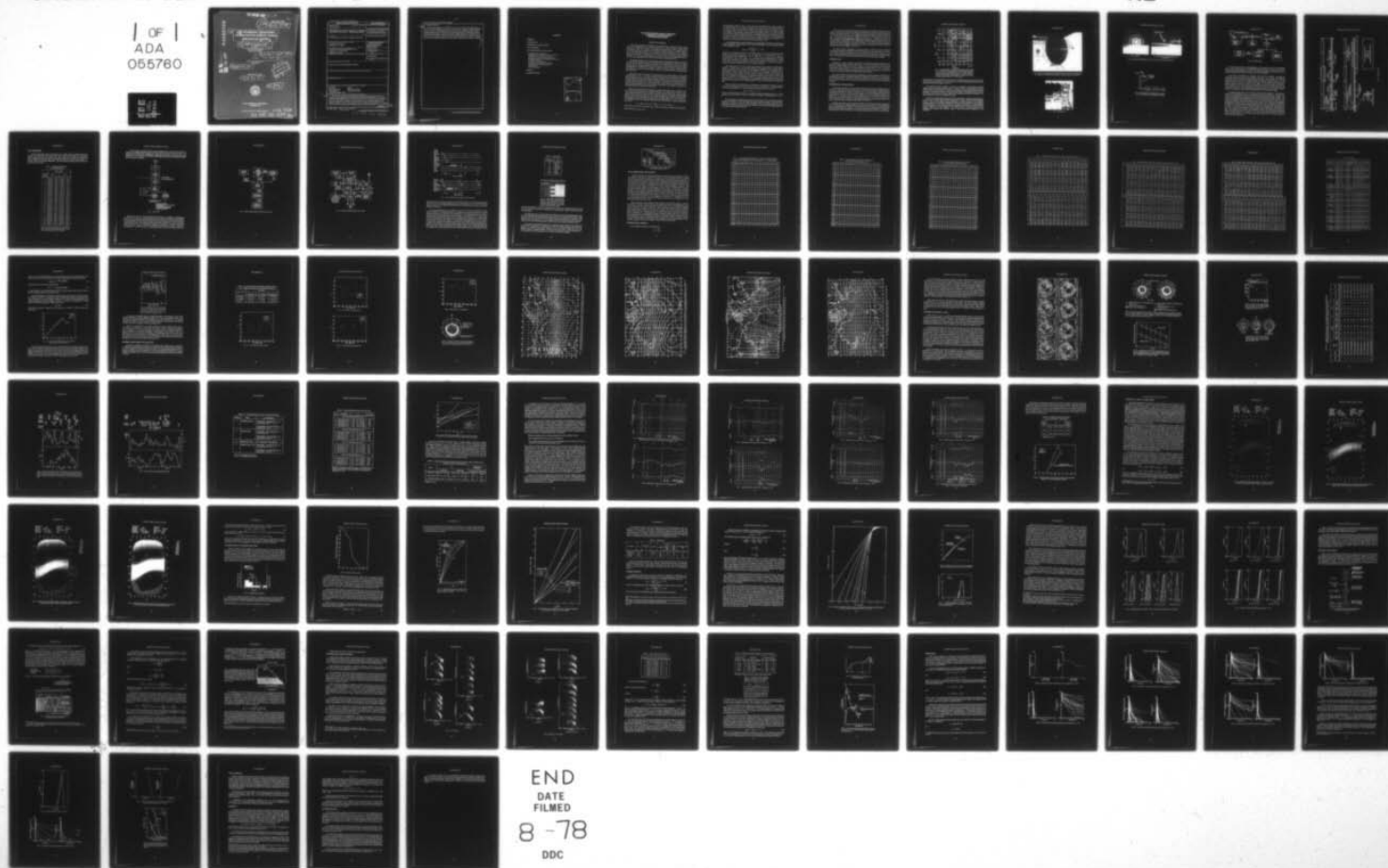
UNCLASSIFIED

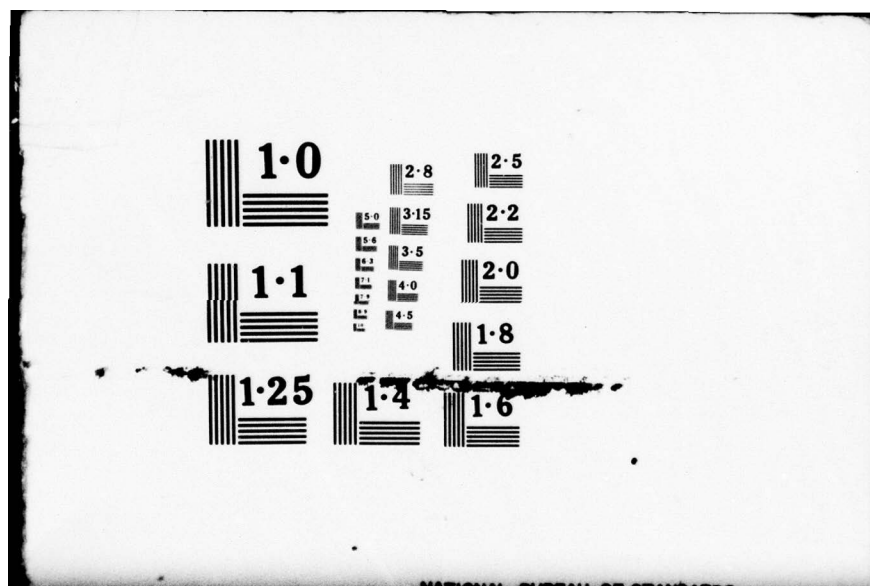
NRL-8160

NL

OF
ADA
055760

11
11





FOR FURTHER TRAN

NRL Report 8160

AD A 055760

AD No. _____
DDC FILE COPY

**UHF Scintillation Characteristics
as Observed From Keflavik, Iceland.
PRELIMINARY REPORT**

10 J. M. GOODMAN, P. L. WATKINS,
C. S. MYERS R. Hogg

Space Environment Branch
Space Systems Division

and
R. Hogg

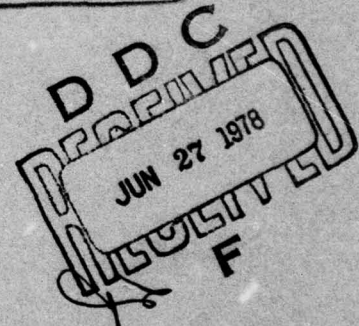
Naval Air Development Center
Warminster, Pa.

9 Interim rept. Oct 76-
Jul 77

16 5071605

February 28, 1978

11 28 Feb 78



12 87p.



NAVAL RESEARCH LABORATORY
Washington, D.C.

Approved for public release; distribution unlimited.

251 950

78 06 26 023 Gen

SECURITY CLASSIFICATION OF THIS PAGE (When Data Entered)

REPORT DOCUMENTATION PAGE		READ INSTRUCTIONS BEFORE COMPLETING FORM
1. REPORT NUMBER NRL Report 8160	2. GOVT ACCESSION NO.	3. RECIPIENT'S CATALOG NUMBER
4. TITLE (and Subtitle) UHF SCINTILLATION CHARACTERISTICS AS OBSERVED FROM KEFLAVIK, ICELAND - PRELIMINARY REPORT		5. TYPE OF REPORT & PERIOD COVERED Interim report (Oct. 1976-July 1977) on a continuing NRL Problem
7. AUTHOR(s) J. M. Goodman, C. G. Myers, P. L. Watkins, and R. Hogg		6. PERFORMING ORG. REPORT NUMBER
9. PERFORMING ORGANIZATION NAME AND ADDRESS Naval Research Laboratory Washington, D. C. 20375		8. CONTRACT OR GRANT NUMBER(s)
11. CONTROLLING OFFICE NAME AND ADDRESS Naval Electronic System Command, PME 106.4 National Center 1, Crystal City, Arlington, Va. 20376		10. PROGRAM ELEMENT, PROJECT, TASK AREA & WORK UNIT NUMBERS NRL Problem A01-59 Program Element 63763N Project S-0716-05
14. MONITORING AGENCY NAME & ADDRESS (if different from Controlling Office)		12. REPORT DATE February 28, 1978
		13. NUMBER OF PAGES 86
		15. SECURITY CLASS. (of this report) UNCLASSIFIED
		15a. DECLASSIFICATION/DOWNGRADING SCHEDULE
16. DISTRIBUTION STATEMENT (of this Report) Approved for public release; distribution unlimited		
17. DISTRIBUTION STATEMENT (of the abstract entered in Block 20, if different from Report)		
18. SUPPLEMENTARY NOTES		
19. KEY WORDS (Continue on reverse side if necessary and identify by block number) Scintillation Spectra High-latitude effects Distribution functions UHF propagation Communication effects Geostationary satellite ATS-6		
20. ABSTRACT (Continue on reverse side if necessary and identify by block number) <i>This is</i> → A study of characteristics of low-elevation and high-latitude scintillation, was initiated in a cooperative program between NRL and NADC during calendar 1976, and under the sponsorship of NAVELEX PME 106.4. Transmissions at 360 MHz from ATS-6 were received at Keflavik, Iceland, during June, September, and October and were analyzed to extract information related to the amplitude scintillation introduced by ionospheric and/or tropospheric inhomogeneities. This report describes the data acquisition and processing procedures and some interim results. → next page (Continued)		

DD FORM 1 JAN 73 1473

EDITION OF 1 NOV 65 IS OBSOLETE
S/N 0102-LF-014-6601

i SECURITY CLASSIFICATION OF THIS PAGE (When Data Entered)

78 06 26 023

20. Abstract (Continued)

The overall average scintillation index S_4 was found to be 0.15, and the 1-99% fading range was about 3.5 dB. The scintillation was found to be more strongly controlled by magnetic than solar activity, as expected. The amplitude statistics were found to be non-Rayleigh, and the smaller scintillation levels observed in this study were roughly approximated by the Nakagami-m model. The power spectra exhibited a power-law rolloff from a ~~corner~~ frequency of 0.067 Hz with an index of -2 on the average. Generally 50% of the scintillation power was provided by frequencies less than 0.03 Hz, and the fade-duration and fade-interval distributions were typically exponential.

CONTENTS

SUMMARY	1
INTRODUCTION	3
EXPERIMENTAL CONFIGURATION	3
DATA PROCESSING	9
DATA COMPUTATION AND ANALYSIS	15
Scintillation-Index Calculations	15
Scintillation and the Position of the Auroral Oval	24
Scintillation and the Indices K_p and R_z	32
Comparison of S_4 Indices with Other Models	48
Percentage Occurrence of Scintillation Index Values	53
Amplitude Distribution	57
Brief Theory of Power Spectra	64
Scintillation Spectra Obtained at Keflavik	68
Scintillation Spectra and the S_4 Index	72
Fading Statistics	74
Other Considerations	81
SUMMARY	81
RECOMMENDATIONS	82

ACCESSION for	
NTIS	Write Section <input checked="" type="checkbox"/>
DDC	Buff Section <input type="checkbox"/>
UNANNOUNCED	<input type="checkbox"/>
JUS TICATION	
BY	
DISTRIBUTION/AVAILABILITY CODES	
P	SPECIAL
A	

UHF SCINTILLATION CHARACTERISTICS AS OBSERVED FROM ICELAND PRELIMINARY REPORT

EXECUTIVE SUMMARY

Under the sponsorship of NAVELEX, the Naval Research Laboratory (NRL), and the Naval Air Development Center (NADC) cooperated in a research program on high-latitude scintillation at UHF. Even though a considerable scintillation data set in the high-latitude region has been obtained by workers at the Air Force Geophysics Laboratory (AFGL), principally at VHF, there was deemed to be an insufficient retrievable data base for the frequency domain near 400 MHz. Additionally the Navy studies were to emphasize design quantities derivable from the intrinsic signal statistics and spectra rather than phenomenological parameters such as the scintillation index, which are principally of geophysical interest.

Accordingly NADC set up a data-gathering system at the Keflavik, Iceland, Naval Station for recording the 360-MHz beacon of the Advanced Technology Satellite ATS-6. The testing intervals were during June and September-October 1976. During the summer interval, ATS-6 was geostationary, being positioned over Lake Victoria (Africa), yielding an elevation angle of approximately 5° to the Keflavik installation. During the autumn interval the satellite was being repositioned to the west and the elevation angles were somewhat higher, ranging between about 14° to 16°.

The antenna system employed for the measurements was characterized by a beamwidth of approximately 13.5°. As a result the studies were potentially contaminated by multipath effects during the summer tests because of ground reflections. This was realized at the outset and was recognized to be an observational constraint to be analyzed for the case of small disadvantaged users at high latitudes. Another constraint to the success of the measurement program was the aircraft traffic at the naval-station airfield, which produced unwanted receiver oscillations before adjustments were made to obviate the problem. Nevertheless a useful data set was obtained for processing by NRL personnel.

During the overall observation periods the average scintillation index S_4 , defined as the ratio of the standard deviation of the signal fluctuations to the average power, was 0.15. Also, the so-called SI scintillation index, employed by AFGL scientists and related to the full fading range, was about twice the value of the S_4 scintillation index on the average. Other average statistics were an rms signal fluctuation of 0.75 dB, a 1%-99% fading range of 3.5 dB, and a 1% fading depth of 1.8 dB. In addition the peak observed fading range was 7.5 dB. On the basis of a correlation analysis the following relationship was found between S_4 and the parameters Σk_p and R_z :

$$S_4 = 0.05 + 4.8 \times 10^{-3} (\Sigma k_p)_f + 5.7 \times 10^{-4} (R_z)_p,$$

where $(\Sigma k_p)_f$ is the sum of the eight 3-hour values of the planetary magnetic index *following*

the observation period and $(R_z)_p$ is the value of the smoothed Zurich sunspot number for the immediate day (24 hr) preceding the observations. This relation is approximate because of the limited number of data groups correlated but nevertheless indicates that magnetic activity is a stronger control than solar activity at these high latitudes, perhaps by an order of magnitude. Magnetic activity being a stronger control was anticipated, since the nocturnal scintillation which was emphasized during this study is undoubtedly related to the nighttime location of the auroral oval which blankets Iceland and is a visible manifestation of magnetospheric influences. Indeed other workers have noted that magnetic activity is more important than solar activity in controlling the high-latitude scintillation depth at VHF.

The amplitude statistics were observed to be non-Rayleigh at 360 MHz; however for the smaller scintillation levels observed in this study the distributions were closely approximated by the Nakagami- m model

$$P(p) = \frac{m^m (p/p_0)^{m-1}}{\Gamma(m)} e^{-mp/p_0},$$

where $\Gamma(m)$ is the gamma function, m is an index, and p and p_0 are the instantaneous and average received powers respectively. It can be shown that $m = 1/S_4^2$, and since $\langle S_4 \rangle \approx 0.15$ during the present observations, $\langle m \rangle$ is about 44. An m value of unity constitutes Rayleigh fading. The extreme values of S_4 were 0.05 and 0.34, suggesting that m ranged between 400 (virtually zero scintillation) and 8.65 during the periods of observation. For the lower values of scintillation observed in the current investigation, a log-normal distribution would be an equally valid approximation to the observed situation.

The power spectra in the current study were generally characterized by a high-frequency rolloff of f^{-2} rather than f^{-3} as was anticipated from our equatorial studies and some work of others at equatorial and midlatitudes. The low-frequency cutoff was not well defined, but its approximation called the corner frequency was 0.067 Hz on the average. Using the Fresnel zone distance as the canonical scale above which scintillation effects become filtered, we deduce the average drift velocity of the inhomogeneity field across the beam to be about 200 m/s. The correlation was insignificant between the rolloff exponent and either R_z or K_p . However for $K_p \geq 2$ the drift velocity of the ionosphere as determined from the spectral corner frequency appears to increase approximately 25 m/s per unity increase in the daily sum ΣK_p .

From an analysis of the distribution of scintillation versus fluctuation frequency, we find that most of the scintillation power resides below the corner frequency ν_c , or for periodicities in excess of approximately 15 s. The S_4 index was found to obey a law of the form

$$S_4(\nu) = S_4(1 - e^{-\lambda\nu}),$$

where ν is the fluctuation frequency, S_4 is the observed total scintillation index, $S_4(\nu)$ is the scintillation index from DC to ν , and λ is a parameter. Typically λ is approximately ν_c^{-1} , or 15 s.

The fade-duration and fade-interval statistics were also shown to be exponential, although the slopes were different in the high-frequency and low-frequency domains. The fade-interval distributions indicate that there is a finite probability that severely disadvantaged users will benefit from scintillation, because constructive interference may increase the signal strength to a level which enhances signal detection.

In terms of the analyses performed by various workers in the field, the high-latitude scintillation environment at UHF may be modeled (synthesized) by hypothesis of jointly Gaussian statistics, provided care is taken. The suggested average low-frequency cutoff should be taken to be approximately 0.07 Hz, and the in-phase and quadrature channels should be filtered in such a way that the high-frequency rolloff is of the order of ν^{-2} . However, to match the data, a cascade of filters (appropriately weighted) will probably be necessary to account for the distinctly different distributions for the long-duration and short-duration domains. Since only amplitude data were obtained, the preliminary analysis in this study provides little guidance in deriving the correlation coefficient between the in-phase and quadrature channels. Nevertheless for weak scatter we suggest a value of 0.1.

The current study is incomplete, and further analysis is required to increase validity of the conclusions reached. Furthermore the data described herein were obtained over a relatively short time during minimum solar activity. Also the low elevation angles during the experiment would be expected to produce some spurious interference effects due to multipath propagation arising because the beam illuminated the earth's surface along with the satellite.

INTRODUCTION

Because of a need to assess the personality of amplitude-scintillation statistics at low elevation angles and high latitudes at UHF (in the vicinity of 350 to 450- MHz), the Naval Research Laboratory (NRL) was tasked to process a set of data obtained by the Naval Air Development Center (NADC) from a site near Keflavik, Iceland (64° N, 23° W). Of principal interest were scintillation indices, scintillation rates, power spectra, probability density and distribution functions, and fade-duration and fade-interval distributions.

This report outlines the experimental configurations, the data acquisition procedures, the tape-digitization and data-processing techniques, the applications software, and the recommended future measurements. Examples of the data are provided in this report, and some conclusions are drawn; however these conclusions are preliminary until more data are obtained and examined.

EXPERIMENTAL CONFIGURATION

The need for data from a low-elevation geostationary source dictated a high-latitude station for the study to be discussed in this report. The synchronous satellite ATS-6 transmits at a frequency of 360 MHz and could be viewed from the U.S. Naval Station at Keflavik, Iceland. The dashed curves in Fig. 1 show the elevation angles for a nominal subsatellite position of 0° latitude, 35° E (over Lake Victoria in Africa, dashed curves). The ATS-6 was scheduled to be maneuvered to a position close to 134° W, requiring 120 days at a rate of 1.4° per day. Also shown (solid curves) are the elevation angles for the fall equinox period during the maneuver, when the elevation angle at Keflavik to the satellite was about 15°.

Available real estate for locating ground terminals was provided to NADC personnel by the U.S. Naval Station, Keflavik, Iceland. From this site the elevation of the geostationary source of transmissions was roughly 5° and the azimuth was 120° (clockwise from due north). During the ATS-6 phasing maneuver, the antenna elevation would maximize to roughly 17° during September 1976, and thereafter the satellite would disappear from view toward the west.

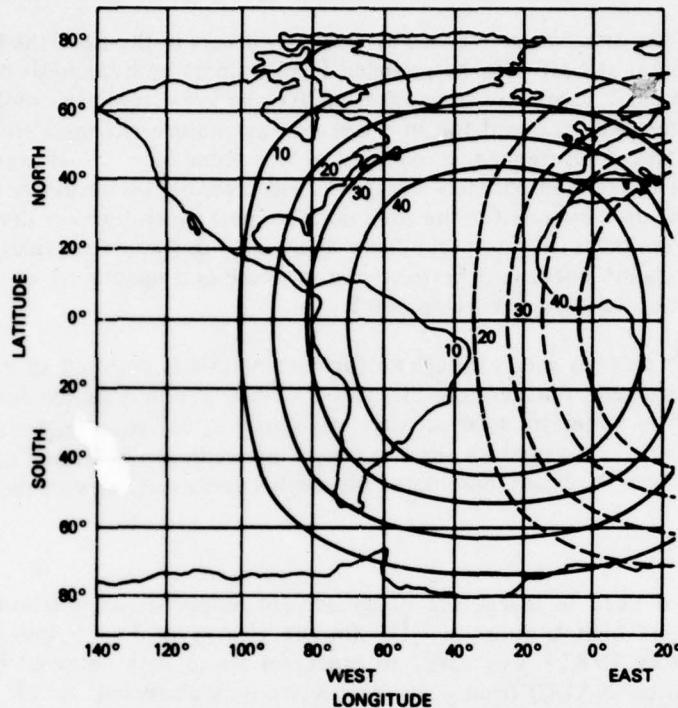


Fig. 1 - Coverage (visibility) curves (labeled with elevation angles in degrees) for the ATS-6 for June 1976 (dashed curves) and September and October 1976. The ATS-6 was approximately over Lake Victoria during June, providing an elevation angle of approximately 5° as viewed from Keflavik. During the equinox period, when the satellite was moving west, the elevation angle was approximately 15 to 17° (solid curves).

The preliminary results discussed in this report were obtained during a short interval in June, when the antenna was fixed at 5° elevation, and for an interval during September and early October when the elevation angle was 14 to 17° .

The ground terminal consisted of a fixed 3.7-m-diameter (12-ft-diameter) parabolic reflector (Fig. 2) and receiving system (Fig. 3). Figure 4 shows the antenna directed toward ATS-6 with an elevation angle of 5° . Figure 4 more clearly shows the relationship between the boresight of the antenna (crossmark) and local aircraft traffic. This geometry was an unavoidable situation and no doubt can lead to some rather troublesome interference problems. As a result the data have had to be interpreted with care.

Figure 5 is a block diagram of the antenna and feed system. Original plans called for reception of both 140-MHz and 360-MHz transmissions. Primary interest was in the 360-MHz channel, however, and insufficient funding eliminated the VHF experiment. The paraboloid furnished a gain of 17 to 19 dB at 360 MHz, and the loss through the 90° hybrid and diplexer were approximately 0.2 dB. Right-hand-circular polarization was employed to obviate Faraday rotation. Figure 6 is a block diagram of the receiver system. As noted, both chart and magnetic-tape recordings were obtained. Figure 3 shows the physical arrangement of the equipment.

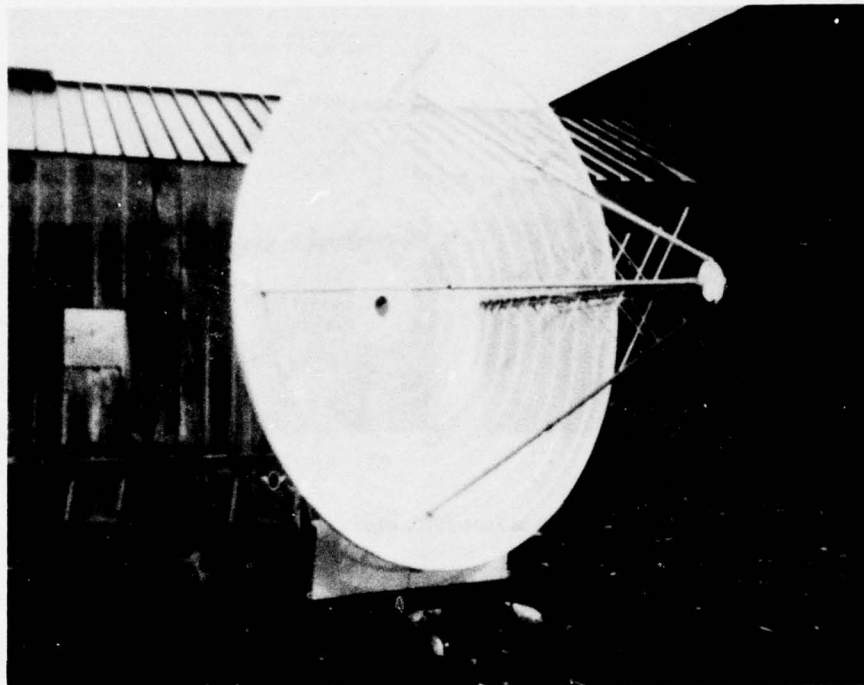


Fig. 2 - The 3.7-m (12-ft) parabolic antenna employed during the observations. The beamwidth was roughly 13.5° , resulting in possible multipath problems during the June measurements.



Fig. 3 - Receiver system

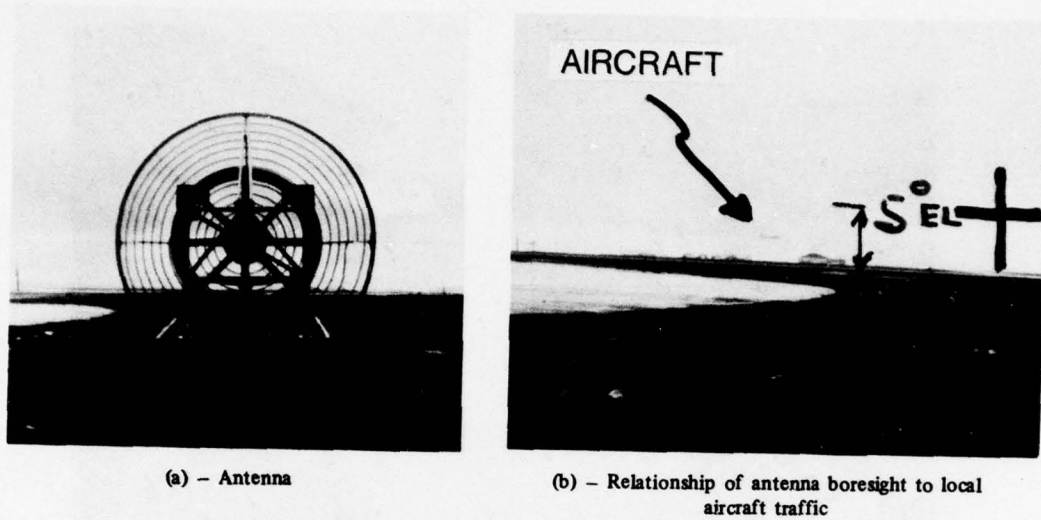


Fig. 4 - Antenna and its boresight in June 1976, when the ATS-6 was at an elevation of 5°

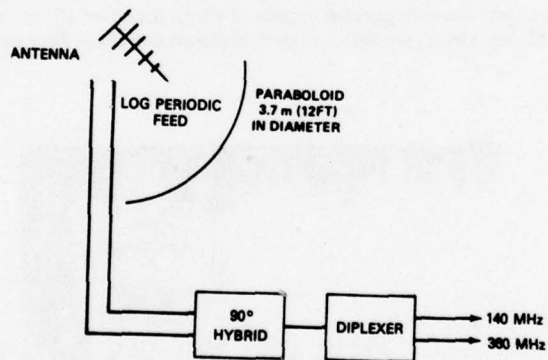


Fig. 5 - Antenna assembly. The antenna gain at 360 MHz is 17 to 19 dB. Right-hand circular polarization was received.

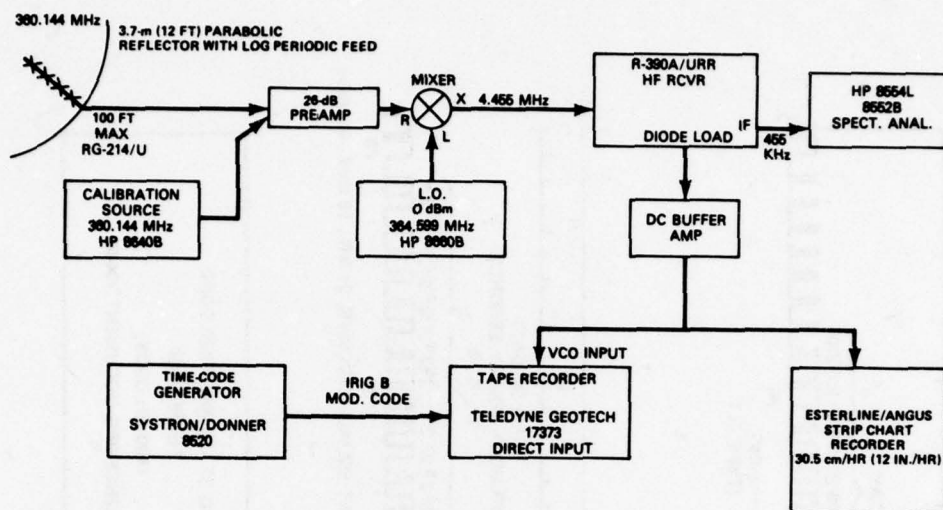


Fig. 6 - Receiving terminal

The ATS-6 transmissions at 360.144000 MHz were heterodyned down to 4.453500 MHz using a local-oscillator frequency of 364.597500 MHz and fed into an HF receiver. The receiver output was amplified and recorded. A low-noise preamplifier providing approximately 25 dB gain at 360 MHz was used prior to mixing with the local oscillator.

The IF filter bandwidths were selectable: either 100 Hz or 1000 Hz. Although the narrow-band filter was preferred for realizing the greatest system margin, noise impulses periodically received caused the 100-Hz predetection IF filter to oscillate for 30 to 45 s and mask the receiver data. Hence the 1000-Hz filter was employed during the latter part of the summer interval to minimize oscillations. This effect was corrected during the September-October observation interval, and the narrow-band filter was once more used. NADC personnel determined that the noise impulses are correlated with ground vehicles and aircraft observed on the taxiways. They concluded that the moving vehicles near the antenna boresight acted as a moving ground plane which caused interference with the received signal.

An Esterline/Angus strip chart recorder provided quick-look graphics. It was helpful in calibration and preprocessing but not in assessing the fine-scale scintillation. Indeed it was found to be misleading as a screening aid for scintillation processing in some instances. For detailed processing, analog recording was done with a Teledyne-Geotech tape recorder. The recorder was operated in the FM mode with a DC-to-34-Hz range and with a 0.9-to-5-V rms sensitivity, providing a 40-dB signal-to-noise ratio on an rms basis. Within the environmental specifications the linearity was $\pm 1\%$ of full deviation (40% of a center frequency of 168.8 Hz), the drift was $\pm 7\%$, the absolute timing accuracy was $\pm 1\%$, and the relative timing accuracy was 0.04 s. The recorder was run at 4.8 mm/s (3/16 in./s) during the tests. Tapes were 12.7 mm (1/2 in.) wide on 36-cm-diameter (14-in.-diameter) reels containing 2.2 km (7200 ft) of tape. Two channels were recorded: the FM data in channel 1 and time code from Systron-Donner time-code generator in channel 2. The time code recorded was IRIG B (100-pps code), as shown in Fig. 7. At the operating tape speed a maximum of 128 hours of data were recorded on each analog tape.

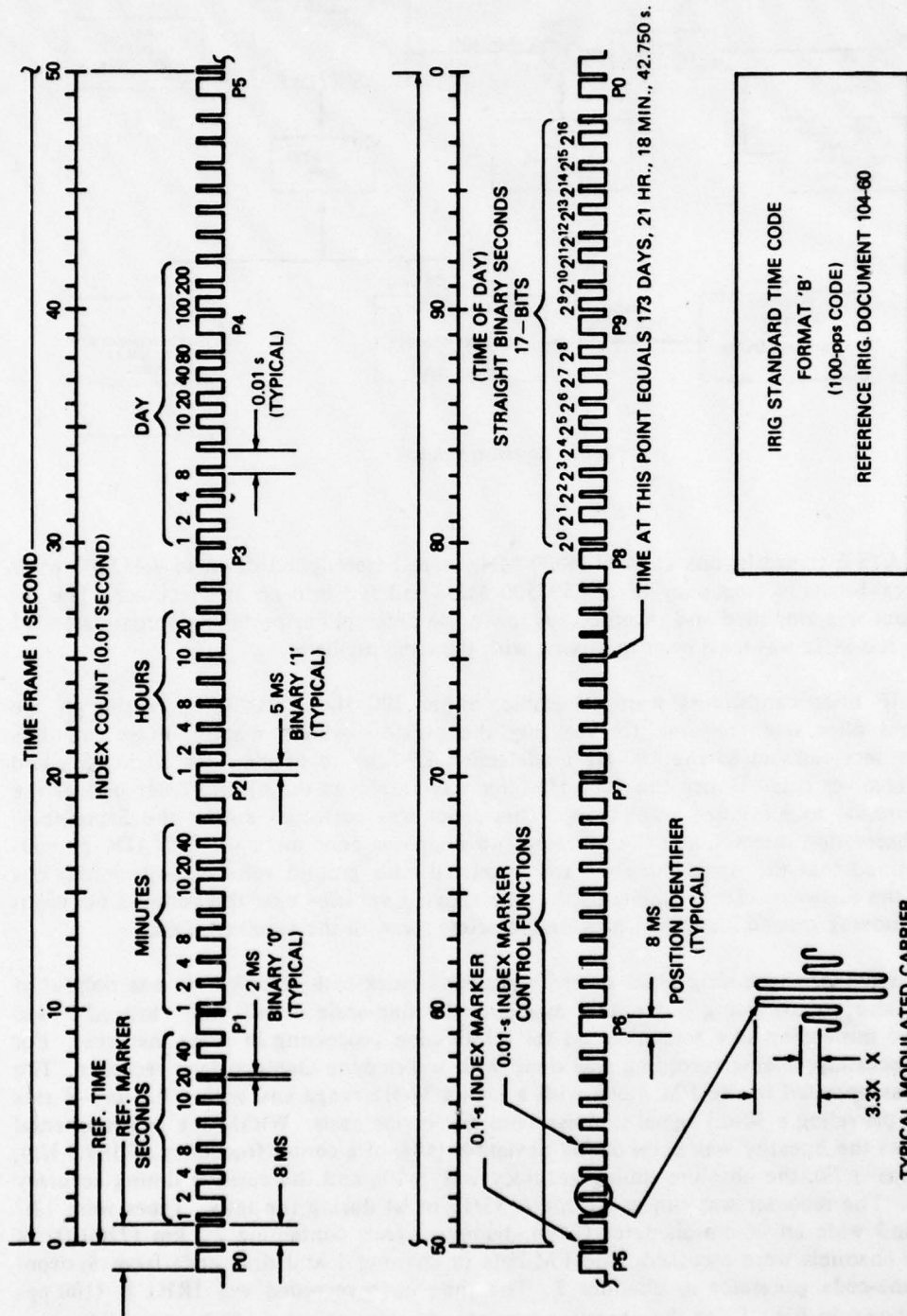


Fig. 7 - Time-code format

DATA PROCESSING

For the June period (June 14 through June 27, 1976), NADC recorded approximately 300 hours of ATS-6 UHF transmissions on 5.2 km (17,000 ft) of magnetic tape. During the autumn period (September and October 1976) approximately 350 hr of data were recorded on 8.8 km (29,000 ft) of magnetic tape. These tapes were delivered to NRL for scintillation processing. The first step involved digitization. As of this writing, 30 digital reels have been produced as shown in Table 1.

Table 1 — Digitized Reels Produced
From Data Recordings

Digital Reel*	Data Interval	
	Start	End
1	6/23/76 — 1428	6/23/76 — 2220
2	6/24/76 — 1543	6/25/76 — 0302
3	6/26/76 — 1543	6/26/76 — 2231
4/5	9/29/76 — 2003	9/30/76 — 1911
6	10/1/76 — 2037	10/2/76 — 1111
7	9/29/76 — 2003	9/29/76 — 1241
8	9/30/76 — 2105	10/1/76 — 0222
9	10/1/76 — 0340	10/1/76 — 1218
10	10/1/76 — 1500	10/1/76 — 1046
11	9/29/76 — 0015	9/29/76 — 1103
12	9/29/76 — 1200	9/29/76 — 2003
13	9/24/76 — 1819	9/25/76 — 0740
16	6/23/76 — 1430	6/23/76 — 2254
17	9/30/76 — 2038	10/1/76 — 0019
18	9/29/76 — 1940	9/29/76 — 2250
19	6/24/76 — 1543	6/25/76 — 0346
20	6/26/76 — 1543	6/26/76 — 2330
21	9/24/76 — 1816	9/25/76 — 0804
22	9/23/76 — 2144	9/24/76 — 1515
23	9/25/76 — 0745	9/25/76 — 2130
24	9/25/76 — 2117	9/26/76 — 1945
25	9/26/76 — 2010	9/27/76 — 2107
	9/27/76 — 2107	9/28/76 — 2258
26	9/29/76 — 0015	9/29/76 — 2026
27	9/29/76 — 2002	9/30/76 — 2119
28	9/30/76 — 2103	10/1/76 — 2055
29	10/1/76 — 2045	10/2/76 — 1442
30	10/1/76 — 2012	10/3/76 — 1838

*Reels 1 through 13 were generated from unfiltered data; reels 16 through 30 were generated using a 3-Hz low-pass filter on the analog data ahead of the digitizer.

The flow diagram associated with the data processing shown in Fig. 8, and the block diagram of the analog-to-digital magnetic-tape data-conversion system is shown in Fig. 9. The digitizer/formatter/controller is configured to sample data continuously at uniform intervals in groups of up to 10^6 samples using relatively small buffer memory and record lengths suitable for minicomputer processing.

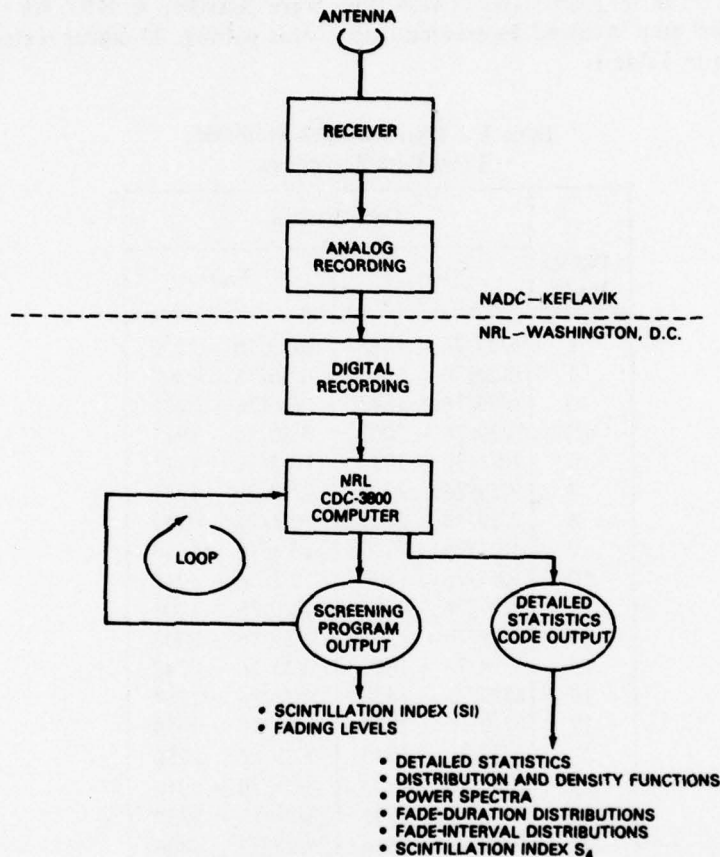


Fig. 8 - Data analysis

Basically the inputs to the digitizer/formatter/controller are threefold: a sampling-rate reference, a time code, and a signal channel. The time channel and signal channel originate from the analog recorder reproducer (Bell and Howell VR 3700B) with the time code having to be generated from the time channel through intermediate processing by a time-code reader (Systron-Donner 8154). The sampling-rate reference is provided by a frequency synthesizer (Lorch-Adret 202). Figure 10 shows the digital/formatter/controller, and Fig. 11 shows the timing sequence. As shown in Fig. 11, the sampling interval of 160 ms is maintained between

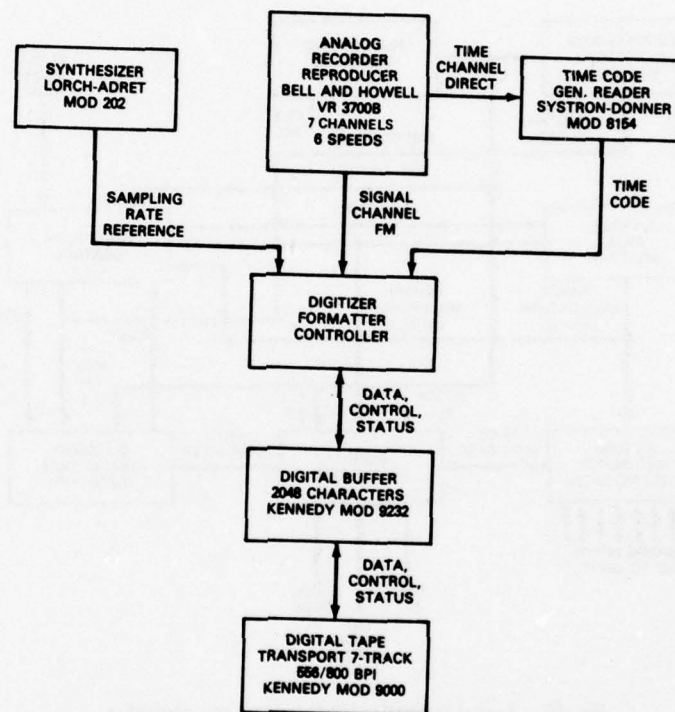


Fig. 9 - Analog-to-digital magnetic-tape data-conversion system

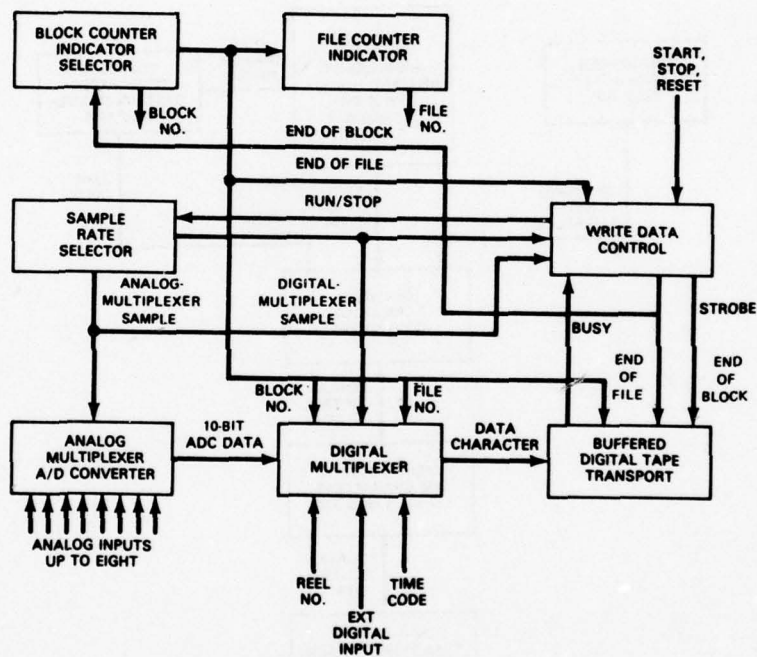


Fig. 10 - Digital magnetic-tape formatter and controller

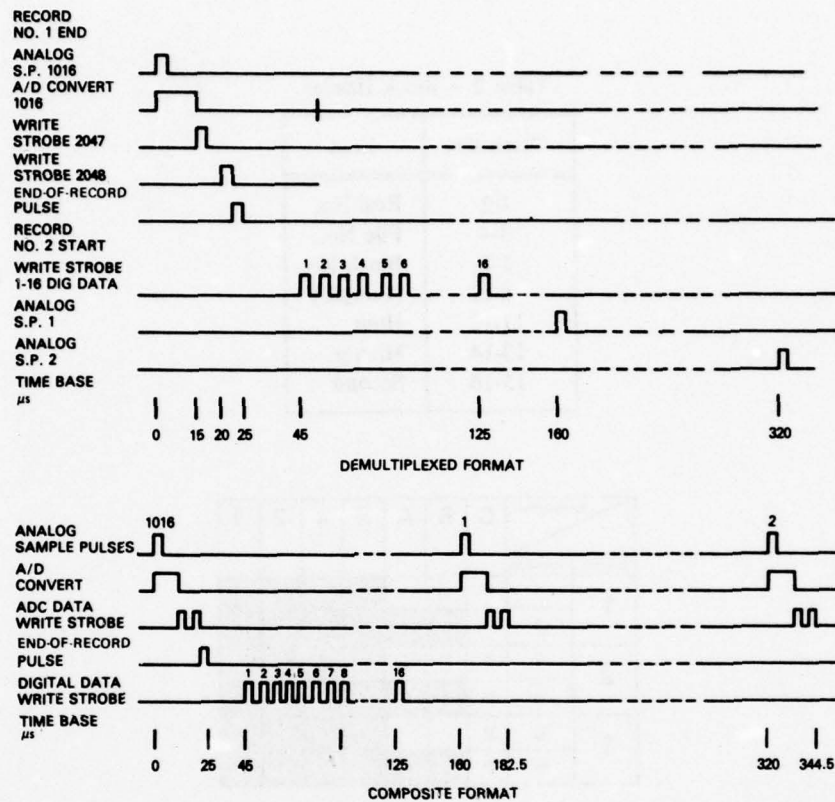


Fig. 11 - Record-cycle timing of the digitizer formatter/controller

sample 1016 of one block and sample 1 of the following block. Very closely spaced sample pulses are used to insert digital identification data at the start of each record without interrupting the continuity of the analog data sampling, which is approximately 5 times the maximum frequency in the data.

The standard digitization rate employed is 156.3 Hz. The format is defined by a block length of between 512 and 2048 characters. The digital tape is seven-track tape with a packing density of either 219 or 315 bits/cm (556 or 800 bits/in.). Both packing densities were used in processing the Keflavik analog tapes. The file length is up to 1024 blocks. As many as eight analog channels are selected, converted, and multiplexed sequentially with a synchronization bit on the last channel in the sequence. For the Keflavik data recordings only one data channel was used. The block has a header of 16 characters for identification, as shown in Table 2. In addition the remainder of the block contains either 496 or 2032 characters of digitized analog data at ten bits per two character samples. Figure 12 depicts two channels of analog data. Only one channel of data was required in the Keflavik analysis, since the 140-MHz data were not recorded. For a 496-character block there are 248 samples, and for a 2032-character block

Table 2 - Block Header

Characters	Item
1-2	Real No.
3-4	File No.
5-7	Block No.
8-10	(Unused)
11-12	Hour
13-14	Minute
15-16	Second

BIT POSITION		C	B	A	8	4	2	1
CHANNEL	CHARACTER							
1	1	P	-	-	9	8	7	6
	2	P	5	4	3	2	1	0
2	3	P	F	-	9	8	7	6
	4	P	5	4	3	2	1	0
1	5	P	-	-	9	8	7	6
	6	P	5	4	3	2	1	0

Fig. 12 - Data format for digitized analog data. The shaded region represents data bit positions. *P* is a parity mark. *F* is a frame mark which appears in the *B* track of the first character of the last channel of each frame. Here two channels constitute a frame.

there are 1016 samples. In the tape formatting four-bit decimal or hexadecimal coding is used for each character of header data, whereas six-bit straight binary coding is used for the digitized analog data.

The sampling rate for the analog data was uniform and continuous during each file. Files are unique data groupings separated by tape discontinuities. If the maximum file length (1024 blocks) is used with the maximum block length (1016 analog samples), the continuity of the sampling rate would extend for over 10^6 samples before the required file-to-file interruption. Figure 13 shows the relationship between the file, block, frame, channel, character, and bit.

To increase the processing speed, there is typically a speedup factor in the analog tape playback prior to digitization. For example, to recover 30 Hz with a speedup factor of 10:1 on playback, we sample at approximately 1500 Hz. That is, we sample 5 times the rate of the highest frequency component desired. No filtering was employed on the FM analog signal prior to digitizing, so the full bandwidth of 0 to 34 Hz in real time was available.

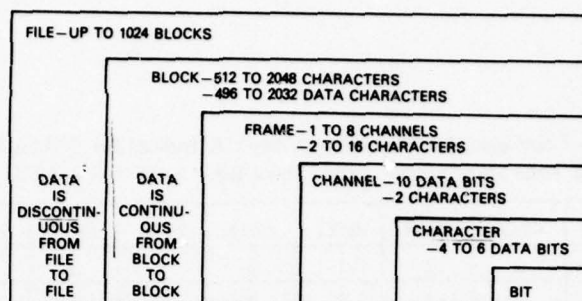


Fig. 13 - Relationships between the file, block, frame, channel, character, and bit

DATA COMPUTATION AND ANALYSIS

After the UHF data were recorded and digitized, a major task was to process the information, taking into account the needs of the users as well as the scientific community. Initially the data were screened by examining the original chart records obtained at the field site to ascertain periods of scintillation and their relative magnitudes. This screening by examining the chart records was ultimately discarded, because high-frequency-fluctuation components were severely filtered, resulting in a misleading picture of the index of scintillation. We next opted to screen the data through consideration of external phenomenological parameters. The canonical parameters selected were the magnetic Q and K indices. This allowed us to separate the data into priority groups, each being assigned an a-priori estimate of perceived scintillation probability. The perceived scintillation probability was reckoned from the "local" K indices from the Leirvogur Magnetic Observatory of the University of Iceland and the Q indices from the Sodankyla Geophysical Observatory. Tables 3, 4, and 5 are the "local" K indices and Tables 6, 7, and 8 are the Q indices for June, September, and October 1977. Subsequently the deduced relationships between K and other parameters such as solar activity (based on R_z) were reckoned from daily planetary values.

Table 9 indicates the SI scintillation index (related to the full fading range), S_4 scintillation index (ratio of the standard deviation of the signal fluctuations to the average power), and "local" Q and K indices, as well as pertinent data such as day, time, reel number, file number, azimuth, elevation, and signal-to-noise ratio. The undisturbed signal-to-noise ratios (SNRs) were typically higher during the low-elevation summer runs and were lower during the September-October runs of higher elevation. For convenience each data group was placed in either a premidnight or a postmidnight category. During the summer there were two premidnight groups and one postmidnight group; during the September-October interval, there were three premidnight and four postmidnight groups. Each group consisted of between one and six files of 30-min duration. Totally there were five groups in both the premidnight and postmidnight categories. Thirty files or roughly 15 hours of data were processed.

Scintillation-Index Calculations

The scintillation index S_4 was computed from

$$S_4 = \frac{\sigma_p}{\bar{p}}, \quad (1)$$

GOODMAN, MYERS, WATKINS, AND HOGG

Table 3 - Leirvogur Magnetic Observatory's K Indices for 3-Hour Intervals in Universal Time During June 1976 (lower limit for $K = 9$ is 1500 gammas)

Day	00-03	03-06	06-09	09-12	12-15	15-18	18-21	21-24	Sum
1	2	2	2	1	3	3	5	5	23
2	5	4	3	2	2	3	2	4	25
3	5	4	2	2	3	3	5	4	28
4	7	7	4	3	3	3	2	4	33
5	6	6	5	3	3	4	4	5	36
6	5	2	3	2	3	4	3	5	27
7	6	5	4	3	3	3	2	6	32
8	4	5	3	3	2	3	2	3	25
9	3	3	2	2	1	2	2	1	16
10	2	2	2	1	2	2	2	5	18
11	7	6	6	5	5	4	5	4	42
12	3	3	3	3	2	4	3	1	22
13	1	2	2	2	2	2	1	3	15
14	2	3	1	1	2	2	1	2	14
15	1	0	2	1	2	2	3	4	15
16	4	4	2	2	2	2	2	3	21
17	3	4	3	4	3	4	3	4	28
18	6	6	5	4	4	3	3	5	36
19	2	2	2	2	2	3	3	2	18
20	4	1	2	2	2	2	2	1	16
21	0	0	0	1	2	2	2	1	8
22	2	0	1	1	2	2	1	1	10
23	3	2	2	1	2	1	1	3	15
24	2	3	2	1	1	5	5	6	25
25	5	5	6	2	3	4	5	4	34
26	4	1	1	2	2	2	5	5	22
27	5	4	3	1	3	2	2	4	24
28	5	3	3	2	1	2	3	3	22
29	3	3	2	2	1	2	3	2	18
30	3	3	5	5	4	5	5	4	34
31									

NRL REPORT 8160

Table 4 - Leirvogur Magnetic Observatory's *K* Indices for
3-Hour Intervals During September 1976

Day	00-03	03-06	06-09	09-12	12-15	15-18	18-21	21-24	Sum
1	4	4	2	2	3	3	4	5	27
2	6	7	7	4	4	3	3	5	39
3	4	6	3	2	2	3	4	6	30
4	5	5	3	3	3	4	3	6	32
5	8	5	2	2	2	3	3	5	30
6	6	5	3	2	2	3	2	3	26
7	6	5	1	2	2	2	2	6	26
8	7	3	1	1	2	3	4	3	24
9	4	3	1	2	2	2	2	1	17
10	4	1	1	1	2	3	4	2	18
11	0	2	2	1	2	2	2	5	16
12	5	5	3	2	2	4	3	3	27
13	4	3	1	1	1	2	2	3	17
14	3	3	3	2	3	4	2	2	22
15	1	6	5	2	3	1	3	5	26
16	5	2	2	1	3	3	2	2	20
17	5	5	2	1	2	2	6	5	28
18	5	7	5	6	4	3	2	2	34
19	1	2	2	4	3	5	6	6	29
20	8	7	7	5	5	5	7	7	51
21	5	6	3	4	5	4	6	6	39
22	6	4	5	3	3	4	5	5	35
23	5	2	3	3	4	4	3	3	27
24	6	2	1	2	2	2	1	3	19
25	6	5	3	3	5	5	6	7	40
26	7	4	3	2	3	3	3	2	27
27	6	4	3	4	3	3	1	5	29
28	5	3	2	2	1	2	3	4	22
29	2	3	2	2	3	3	3	4	22
30	3	4	1	2	2	3	4	6	25
31									

Table 5 — Leirvogur Magnetic Observatory's *K* Indices
for 3-Hour Intervals During October 1976

Day	00-03	03-06	06-09	09-12	12-15	15-18	18-21	21-24	Sum
1	4	2	4	4	3	2	2	6	27
2	6	6	6	3	4	4	2	4	35
3	5	4	3	3	2	3	0	4	24
4	3	2	1	1	2	2	2	3	16
5	6	6	2	2	2	3	3	3	27
6	4	5	4	3	2	2	3	6	29
7	5	1	1	1	2	3	4	2	19
8	0	1	1	2	2	2	3	3	14
9	4	4	1	1	1	3	4	3	21
10	3	3	1	2	1	3	3	6	22
11	6	3	1	2	1	2	3	5	23
12	4	4	1	1	2	2	5	7	26
13	3	4	3	3	2	2	2	3	22
14	1	0	1	2	1	1	3	5	14
15	5	5	5	4	5	5	7	7	43
16	7	7	6	5	3	3	5	6	42
17	5	6	6	4	4	4	5	6	40
18	7	6	4	3	3	4	4	2	33
19	1	0	1	2	3	3	3	4	17
20	6	2	2	2	2	2	1	4	21
21	3	4	4	2	2	2	2	4	23
22	5	2	1	2	2	2	1	2	17
23	3	3	1	2	2	2	3	5	21
24	2	0	0	1	2	2	3	3	13
25	5	0	1	1	1	1	0	2	11
26	3	1	1	1	1	1	1	4	13
27	2	2	1	2	2	2	3	5	19
28	5	0	1	1	2	2	2	3	16
29	2	3	1	1	0	0	1	1	9
30	0	0	1	2	3	3	7	7	23
31	5	6	7	5	4	5	6	6	44

NRL REPORT 8160

Table 6 - Sodankyla Geophysical Observatory's Geomagnetic Q Indices During June 1976

	1	2	3	4	5	6	7	8	9	10	11	12	13	14	15
0 ^h	1100	3321	0122	0120	4433	4331	3223	3211	0000	0000	5555	1000	0001	0001	0000
	0000	0111	2222	1111	3344	1011	1122	1111	0000	0000	6777	0111	0000	1111	0000
	0000	1111	0011	2245	4433	1122	3332	1211	0000	0000	7776	1112	0000	1111	0000
	0000	1200	0000	5544	3201	1110	2111	1111	0001	0000	6665	1011	0110	0001	0000
	0010	0001	1000	3323	2233	0021	1111	1112	0000	0000	5443	0000	0000	1000	0000
	0000	0010	1000	3222	2331	1011	1111	2211	0000	0000	3333	0000	0011	0000	0001
6 ^h	0000	1210	0000	3211	3322	2211	1121	1010	0010	0000	3444	0011	1000	0000	0000
	0001	1000	0000	1123	2112	1121	1122	0011	0110	0000	3333	1100	0111	0010	0000
	0010	0011	0000	1222	2111	2111	1001	1112	0110	0000	3223	1112	1110	0000	0000
	0010	2111	0000	2221	1232	1002	0000	2221	0100	0000	2123	2210	0010	0000	0000
	1010	0010	0001	2211	2023	1310	1333	2100	0000	0001	3455	1213	1111	0000	0000
	0000	0000	0010	2222	3323	1012	2221	1133	0000	1212	6655	3110	0011	0110	0000
12 ^h	0010	0000	0001	3213	3444	1321	2322	2210	0000	2110	5545	0110	1111	0000	0000
	0011	0010	0101	4554	2122	1112	3232	2210	0000	0221	5556	1221	1111	0000	0000
	1211	1000	0011	3222	1122	2212	1211	0111	0000	2211	7765	1111	1110	0000	0000
	1111	0011	1110	2101	3333	2221	1230	1111	0000	0000	5455	1122	0000	0000	0000
	1221	0111	1111	1120	2223	3332	1110	0111	0000	0011	4444	3332	0000	0000	0000
	1110	1112	1113	1110	2222	3111	1100	1110	0000	0000	4443	3322	0000	0000	0000
18 ^h	1011	1121	3212	0000	2121	1001	1001	0001	0000	0000	3322	1110	0000	0000	0000
	1211	1111	2223	0000	2222	0000	0001	0012	0000	0000	3344	0000	0000	0000	0001
	1244	1111	3456	1112	2333	0011	1001	2222	0000	0000	3445	0000	0000	0000	0012
	4443	1222	6654	3344	3333	0111	1023	2221	0000	0010	5455	1110	0000	0000	3333
	3333	1111	4443	3222	3356	2333	5656	0000	0000	0112	4432	0000	1111	0000	1110
	2333	1110	3210	2344	6665	3223	5444	0000	0000	3555	1100	0000	1100	0000	0001
	16	17	18	19	20	21	22	23	24	25	26	27	28	29	30
0 ^h	0000	1111	2333	1011	0222	0000	0000	0000	0000	6665	1111	0000	3333	0000	0000
	0000	0000	4545	1111	2110	0000	0011	0001	1111	5554	1111	0121	3221	0010	0000
	0111	0000	5543	1111	1011	0000	1111	1000	1111	3221	1011	0011	0000	0000	0002
	1111	1100	3222	1100	0111	0000	0000	0001	0000	3332	0011	1001	0000	1111	0000
	1011	1110	3221	0000	1101	0000	0000	0000	0111	2212	1000	1011	0000	1000	1011
	0001	0000	2213	0000	1100	0000	0000	0000	0000	2212	1111	1000	0000	1001	0111
6 ^h	0100	0012	2222	1000	0000	0000	0000	0000	0111	2322	1111	0111	0000	0000	0001
	0001	1221	1223	0000	0000	0000	1000	1001	1100	2121	0010	1111	0001	0000	1123
	0100	2212	3323	0000	0000	0000	0000	0000	0000	1011	0100	2110	0100	0001	3344
	0011	1233	3321	0101	1111	0000	0001	0000	0000	0000	0010	0000	0010	0010	3223
	2210	3333	2333	1010	1100	1001	0000	0010	1111	0012	0110	0111	0111	0000	4445
	1000	3223	3244	1122	1101	1001	0000	0002	1211	3322	0110	2202	0100	0000	5433
12 ^h	0000	3322	4442	1111	0010	0111	0000	1110	0000	1232	1011	2100	0000	0000	3233
	0000	2334	3333	1011	0011	1110	0011	0000	0000	1222	0000	1100	0100	0000	1112
	0000	3334	3333	0011	2200	0000	2110	1100	0000	2222	1001	1221	0000	0000	2122
	0000	4443	2223	1111	0101	0000	0000	0011	1221	2334	0001	0001	0000	0000	2332
	0000	2222	3222	0011	1010	1110	0000	1000	1143	4243	0000	1011	0000	0121	3333
	0000	2122	2233	1111	0000	0001	0000	0000	3333	3211	0000	1100	0001	0011	3443
18 ^h	0000	2111	1100	1100	0000	0010	0000	0000	3554	2211	0012	0000	0012	0000	2333
	0000	1111	0022	0000	0000	0111	0000	0000	4211	1135	2133	1110	2122	0002	3333
	0000	2111	2334	0000	1100	1001	0000	0101	2331	4443	2345	1011	1133	2110	4333
	1221	0333	4443	0000	1111	0000	1100	1100	2211	3444	5544	1112	2222	0000	4444
	1100	2121	3444	0000	1011	0000	0000	0000	2334	4443	4333	2222	1000	0000	4333
	0000	0000	0000	0000	0000	0000	0000	0000	0000	0000	0000	0000	0000	0000	0000

GOODMAN, MYERS, WATKINS, AND HOGG

Table 7 - Sodankyla Geophysical Observatory's Geomagnetic Q Indices During September 1976

	1	2	3	4	5	6	7	8	9	10	11	12	13	14	15
0 ^h	4443	5444	3200	1111	6776	3221	0123	4444	1222	0000	0000	3222	0100	0000	0000
	2221	3211	1221	2122	5321	1223	3443	3332	1100	0011	0000	2111	0000	0000	0000
	1110	1122	0021	2211	1112	3333	3333	1111	0110	0000	0000	1111	0000	1011	0001
	1111	2111	1111	2223	1211	3222	2101	1111	0000	0000	0100	1100	0000	1111	0011
	0000	1222	1112	2221	1001	2212	1111	1111	0000	0000	0011	1000	0000	1000	2333
	0000	1124	2221	0110	0210	0111	1110	0000	0000	0000	0011	0001	0000	0000	3322
6 ^h	0000	4433	1111	1111	0000	1111	0010	0000	0000	0000	0100	0011	0000	0110	2212
	1221	3333	1111	0110	0111	2211	0000	0000	0000	0000	0000	1100	0000	1110	2221
	1101	3333	0100	0001	2100	0000	0000	0000	0000	0000	0000	1010	0000	0000	1112
	1011	2332	0111	1101	1111	0000	0013	0000	0000	0000	0000	0022	0000	1111	2111
	0100	3333	0111	1012	0011	0000	1000	0002	0121	1100	0000	1111	0100	1211	1100
	0001	3222	1222	2111	2221	0011	1100	2312	0011	0000	0001	0000	0000	2221	1111
12 ^h	2211	2333	2221	1001	3211	1101	1111	0000	2223	0000	0110	1110	0000	2222	1122
	1112	3344	0000	1112	1001	1122	1100	0000	3222	0001	0100	1211	0000	2121	1111
	3333	3444	0011	3334	1111	1121	0010	0000	1800	0000	0001	0011	0000	1112	1000
	3343	4331	1111	4332	1100	1112	0100	0000	0001	0000	1100	0110	0000	1121	0000
	2110	1111	2211	1111	1111	1100	1111	0111	1000	0010	0000	1221	0000	1120	0000
	1112	0111	0001	0000	0110	0121	1100	1111	0000	1110	0000	2333	1100	0000	0000
18 ^h	2233	1122	0023	1000	0110	1100	0000	1121	0000	0022	0001	1110	0000	0001	0000
	3333	2234	3333	0000	0001	0000	0000	2554	1000	2210	0100	0000	0000	1111	0111
	3211	3333	1123	0002	1111	0000	0001	1100	0000	0011	0000	0023	0000	1122	1211
	0000	3344	5666	3333	0000	0000	0103	0000	0000	0222	1000	3222	2111	2222	2322
	0012	4555	4443	3333	0112	0000	4333	0000	0000	2200	0000	2211	1111	2111	2332
	3455	4433	1010	2204	2333	1111	3223	0111	0000	0000	1233	0000	1100	1000	1110
	16	17	18	19	20	21	22	23	24	25	26	27	28	29	30
0 ^h	0000	0000	5432	0000	6787	7544	5433	3321	0000	1346	7654	0133	3321	0000	1111
	0111	0001	2211	0000	7653	3333	2111	1000	0122	6555	3322	3333	1110	0000	1000
	1110	1111	1122	0000	3344	2223	1211	0000	2211	5433	1112	3311	0000	0000	0000
	0000	1111	2334	0010	3356	3442	1112	0011	1111	3321	1122	2221	0000	0000	0011
	0000	1100	4433	0001	6654	2332	3232	1110	0000	1111	1011	1011	0000	0110	1111
	0000	0001	4554	0001	3343	3332	2233	0101	0110	1110	0000	1112	0000	0100	0000
6 ^h	0000	0001	4544	1000	4445	1111	3231	0011	0000	1110	1110	2110	0000	0000	0000
	0000	0000	4333	1110	4524	1222	2223	1222	0100	0000	0012	0010	0000	0010	0000
	0000	1200	4554	1211	3233	2222	2222	2212	0010	0001	1011	1100	0100	1011	0000
	0000	1000	4444	1111	3333	2223	2122	2122	0111	1222	0100	0011	0000	1202	0000
	1000	0000	3344	2222	3334	2233	2221	3333	1122	1111	0122	2210	0001	1221	0010
	0111	0001	4345	3223	5445	2112	1233	3233	1211	1112	2222	0122	0011	0010	0011
12 ^h	1000	1101	5554	3322	5577	3333	3222	2223	1110	2233	2211	1132	0000	1123	0221
	0012	0110	3455	3332	7644	1434	3332	3332	0000	4345	1000	1211	0000	2101	1101
	2111	1100	5533	3212	5546	4332	2332	2122	0000	5666	0000	1322	0100	0121	2221
	1110	0000	3222	3333	6432	3234	2212	1100	1100	5666	0111	1121	0000	0000	0111
	1110	0001	2111	4555	2333	5554	3433	0111	1000	4555	1111	0012	0100	1000	1101
	0000	0111	1111	4443	5342	3321	3222	2110	1122	5444	1122	2332	0000	1001	2000
18 ^h	0111	0001	0011	3335	4666	2222	1110	0001	2110	4557	4433	1111	0010	1111	0000
	1113	1123	2011	5654	5555	2345	1366	1112	0000	5556	1110	1100	0000	1111	0013
	3111	3667	1001	4456	6677	5544	5543	3233	0000	6665	0000	0021	0122	1332	4455
	1000	7766	1221	6543	7777	4432	4444	2232	0000	4532	0100	1122	3333	2332	5665
	0000	5555	0000	5667	6555	2222	4443	3322	0000	4455	1121	3333	1110	1222	5444
	0000	5565	0010	7654	6687	3345	3333	1000	0001	5578	1000	3443	0000	2111	3322

NRL REPORT 8160

Table 8 - Sodankyla Geophysical Observatory's Geomagnetic Q Indices During October 1976

	1	2	3	4	5	6	7	8	9	10	11	12	13	14	15	
0 ^h	2210 0011 1111 1112 1111 1010	2112 2345 5444 3233 3344 4333	2222 2112 2112 0011 1111 0102	0000 0000 0000 0000 0000 0000	1001 2344 5543 3222 1111 1111	0000 0000 0001 1111 1110 1222	3322 1111 0010 0000 0000 0000	0000 1111 0000 0000 0000 0101	0111 0000 0000 1111 0010 0021	0111 1100 1000 0000 0000 0000	3333 3333 3220 1111 0001 1002	1222 1111 0010 0010 1200 0100	1111 0010 0010 0111 1210 0001	0000 0000 0000 0000 0000 0000	5431 1000 1011 2121 2221 1222	
6 ^h	0000 0010 0122 2221 2333 3211	2333 2312 2222 1112 3323 3333	1111 1111 1210 1000 1111 0110	0000 0000 0110 2110 2110 1000	1211 0010 1110 0111 1211 1100	2110 1101 0112 2333 2110 0011	0010 0000 0000 0000 0000 0000	0000 0000 0000 0000 1000 0000	1110 0000 0000 0000 0000 0010	0000 0000 0000 0000 0000 0000	1000 0000 0000 0000 0000 0000	0010 0000 0000 0000 0000 0000	0111 1210 0121 1011 1111 1100	0001 0000 0000 0000 0000 1000	2222 2212 2122 2331 1223 4443	
12 ^h	1111 1122 1221 0111 1000 0000	3333 3222 2211 3444 4321 0100	0010 1111 1113 3211 1012 1001	1121 1211 1100 0011 1100 0100	0100 0000 0004 1121 0000 0011	1000 0000 0000 0011 0000 0000	0110 0000 0000 0001 1111 2333	0010 0000 1000 0010 0000 0011	0110 1111 2210 0000 0000 0002	0000 0000 0011 1010 1113 3220	0000 0000 1111 0013 3122 1101	1100 0112 2011 0000 0000 0101	1011 0101 1111 1111 0000 0000	0000 0000 0000 1111 0000 0001	3467 7555 3556 5444 6744 4455	
18 ^h	0000 1111 0012 2356 7643 3221	0110 0001 2122 2221 0011 0112	1100 0000 0000 0000 0000 0110	0000 0000 0013 3322 1001 2100	1112 2222 1110 0001 1011 0100	0001 1111 1344 1001 4320 2232	2244 4322 1001 0110 0112 0000	1101 1122 1123 3320 0000 0000	3322 1210 0111 0011 1101 1100	2111 1112 2112 2222 2345 5554	1211 1222 2334 4445 4432 2212	1123 3554 4466 6677 7652 2233	0000 0010 1111 1100 0000 0000	1011 1220 1233 3445 5555 6766	5454 5346 7877 6666 8877 7788	
	16	17	18	19	20	21	22	23	24	25	26	27	28	29	30	31
0 ^h	7777 6354 5544 4554 4543 4433	5444 3222 2211 1122 2322 3343	4443 4344 6665 4444 3321 1211	0000 0000 0000 0000 0001 0000	2223 4443 2100 0000 0000 0000	1011 1011 1111 1100 0110 1001	1222 2222 1100 0000 1000 0000	0000 0000 0011 1000 0010 1010	1000 0000 0000 0000 0000 0000	0012 2222 1011 1011 0001 0000	0000 0000 0000 0010 0000 0001	0000 0000 0000 0010 0000 0000	2222 0010 0000 0000 0000 0000	0000 0000 0000 0000 0000 0000	0000 0000 0000 0000 0000 0000	6932 2222 2222 2221 2122 2122
6 ^h	2223 3223 3443 4333 4413 3312	3222 3344 3333 3433 3443 3344	1100 1112 1222 2212 2223 3333	0000 1000 0000 0000 0000 1112	0000 0000 0000 0000 0011 0000	1111 0000 1001 0112 0122 2112	0000 0000 0001 0000 0000 0000	0100 1100 0000 0010 0000 0001	0000 0000 0000 0000 0000 0000	0000 0000 0011 0000 0000 0000	0000 0010 0000 0000 0000 0000	0000 0000 0000 0001 0000 0000	0000 0000 0000 0000 0000 0000	0000 0000 0000 0000 0000 0000	0000 0100 1001 1010 0001 1111	3334 3433 4443 3333 3333 2321
12 ^h	3333 3332 1222 2111 1111 2222	4445 6544 3222 2221 1100 1233	4332 1010 0010 0000 1124 3232	2111 1111 0113 3444 3331 2212	0000 0000 0000 0000 0001 1111	1111 0000 1101 0000 0122 2112	0000 1110 0000 0000 0000 0000	1111 0000 0000 0112 1110 2210	0000 1110 0000 0111 1212 1000	0000 0000 0000 0000 0000 0000	0000 0000 0000 0000 0000 0000	0000 1000 0010 0001 0012 2100	0000 0000 1100 1110 1111 2100	0000 0000 0000 0000 0000 0000	1112 2344 3211 0010 1335 5334	1133 4455 5555 5666 6654 4314
18 ^h	1124 4346 6666 5544 5676 5655	3445 5554 4343 2333 4445 5664	1000 0143 6653 2110 0000 0000	3333 2211 2112 2222 2111 1112	2211 1000 0001 1233 3322 3321	0011 0000 1110 1100 0000 0111	0000 0000 0000 0000 0000 0111	1112 2222 2333 2222 3322 2211	0000 0003 4443 2200 0000 0000	0000 0000 0000 0000 0000 0000	0000 0000 0100 0000 0000 3210	1111 1212 2333 4555 1211 3221	0000 0001 1111 1111 1211 1110	0001 0001 0000 0000 0000 0000	4333 3332 3333 4567 7778 8877	3344 4444 3334 5555 4555 5555

GOODMAN, MYERS, WATKINS, AND HOGG

Table 9 - Data Summary

Group	Date	T ₀	Reel	File	Az (deg)	El (deg)	SNR (dB)	SI	S ₄	Q	K
Low Elevation											
1	6/23/76	2118	16	3	120	5	12.6	0.26	0.10	1	3
		2149	16	4	120	5	12.6	0.42	0.22	0	3
		2221	16	5	120	5	12.6	0.21	0.05	0	3
Daily av		2150	—	—	120	5	12.6	0.30	0.12	0.3	3
2	6/25/76	0140	19	1	120	5	13.9	0.41	0.14	3	5
		0211	19	2	120	5	13.9	0.47	0.34	2	5
		0243	19	3	120	5	13.9	0.44	0.19	3	5
		0314	19	4	120	5	13.9	0.42	0.13	3	5
Daily av		0227	—	—	120	5	13.9	0.44	0.20	2.8	5
3	6/26/76	2020	20	1	120	5	14.6	0.12	0.09	5	5
		2051	20	2	120	5	14.6	0.25	0.07	5	5
		2123	20	3	120	5	14.6	0.20	0.05	4	5
		2155	20	4	120	5	14.6	0.27	0.07	3	5
		2227	20	5	120	5	14.6	0.19	0.12	3	5
		2258	20	6	120	5	14.6	0.15	0.06	1	5
Daily av		2139	—	—	120	5	14.6	0.20	0.08	3.5	5
Av daily av		2259	—	—	120	5	13.7	0.31	0.13	2.2	4.3
Higher Elevations											
4	9/25/76	0039	21	12	195	16	9.9	0.43	0.26	5	6
		0111	21	13	195	16	9.9	0.38	0.13	5	6
Daily av		0055	—	—	195	16	9.9	0.40	0.20	5	6
5	9/25-26/76	2355	24	5	195	16	8.9	0.38	0.14	7	7
	9/26/76	0027	24	6	195	16	8.9	0.27	0.13	4	7
	9/26/76	0059	24	7	195	16	8.9	0.28	0.13	3	7
Daily av		0027	—	—	195	16	8.9	0.31	0.13	4.7	7
6	9/29/76	2105	27	2	207	15	10	0.38	0.24	3	4
		2137	27	3	207	15	10	0.29	0.15	2	4
Daily av		2121	—	—	207	15	10	0.34	0.20	2.5	4
7	9/30/76	2206	28	2	210	14	11	0.37	0.17	3	6
		2238	28	3	210	14	11	0.36	0.18	2	6
		2309	28	4	210	14	11	0.43	0.20	2	6
Daily av		2238	—	—	210	14	11	0.39	0.18	2.3	6
8	9/30/76	2116	29	1	210	14	12.3	0.35	0.15	5	6
		2148	29	2	210	14	12.3	0.43	0.16	7	6
		2220	29	3	210	14	12.3	0.33*	0.15	4	6
Daily av		2148	—	—	210	14	12.3	0.37	0.15	5.3	6
9	10/2/76	0036	29	8	210	14	12.3	0.34*	0.16	1	6
Daily av		0036	—	—	210	14	12.3	0.34	0.16	1	6
10	10/2/76	0243	29	12	210	14	12.3	0.33	0.14	3	6
		0315	29	13	210	14	12.3	0.27	0.24	3	6
		0346	29	14	210	14	12.3	0.27	0.15	3	6
Daily av		0315	—	—	210	14	12.3	0.29	0.18	3	6
Av daily av		2258	—	—	205	15	11.0	0.35	0.17	3.4	5.9

*In arriving at the value, extraneous block estimations of SI owing to interference were rejected.

where σ_p is the standard deviation of the power fluctuations and \bar{p} is the average power over a 30-min file. But the average scintillation index SI was estimated for each 30-min file from

$$\text{average SI} = \frac{SI_{\max} + SI_{\min}}{2}, \quad (2)$$

where each block value of SI was obtained from

$$SI = 1 - \text{antilog} \frac{1}{10} \text{FR (dB)}, \quad (3)$$

in which FR(dB) is the third peak down from the maximum signal minus the third null up from the minimum signal over a data block (30 s).

The preceding recipe for obtaining SI was devised by personnel of the Air Force Geophysics Laboratory (AFGL) as a convenient scheme of obtaining scintillation characteristics from chart records and is not as meaningful a parameter as S_4 , since it somewhat depends on the amplitude distribution function, whereas S_4 does not. Generally SI corresponds to a fading range in the 98-99% neighborhood. Figure 14 shows that

$$SI \approx 2S_4. \quad (4)$$

This relation is generally in agreement with findings by H. Whitney of AFGL (private communication).

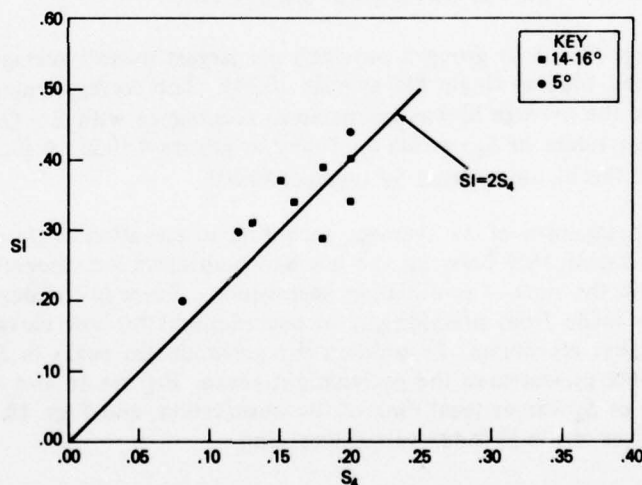


Fig. 14 - Relation between the average values of the S_4 index and the average values of the SI index

The SI indices each reckoned over a data block exhibited a considerable variation over a file of 30 min. Figure 15 shows the variation of SI for a particular interval of interest. The range of values is between 0.2 and 0.57 in this special case, with the average being about 0.4. Equation (2) implies $SI = 0.38$, and the exact index $S_4 = 0.20$. Hence the relation $SI \approx 2S_4$ is satisfied on the average. The system designer must note however that the short-term full-range fading statistics are more severe than would be suggested by an SI of 0.4.

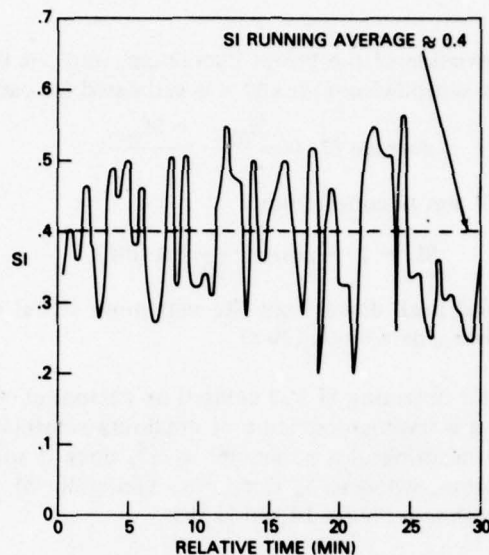


Fig. 15 - Computed values of SI for reel 27, file 2 (2105-2136, 9/29/76). The 32-s blocks exhibited SI values ranging between 0.2 and 0.57, whereas the running mean is about 0.4. The S_4 index for this file is 0.20; thus $S_4 \approx SI/2$.

At low elevation (Table 9) group 2 provided the largest overall average S_4 index (0.20) and also contained the highest single file average (0.34). The corresponding SI indices were 0.44 and 0.47 (where the average SI was estimated in accordance with Eq. (2)). At the higher elevations the highest values of S_4 per file are found in groups 4 (0.26) 6 (0.24), and 10 (0.24). Groups 4 and 6 have the highest overall S_4 averages (0.20).

Table 10 is a breakdown of S_4 averages according to elevation angle and time of day. Most striking is the dissimilarity between the low and high elevation categories with regard to the S_4 dependence on the time of scintillation observation. There is a strong enhancement in S_4 as a transition is made from premidnight to postmidnight for low elevation; there is no difference for the higher elevations. In addition the postmidnight peaks in S_4 (the maximum file average of S_4) were greater than the premidnight peaks. Figures 16 and 17 show the average and peak values of S_4 versus local time of the observation, and Figs. 18 and 19 show the average and peak values of the SI index versus local time.

Scintillation and the Position of the Auroral Oval

Inasmuch as scintillation is closely tied to the position of the auroral oval, it is instructive to examine the approximate location of the oval (Fig. 20) under average conditions. Figure 21 is a map of magnetic-dip contours. (Figure 22 is map of the magnetic-dipole latitudes, with the magnetic-dip equator shown as a dashed line. As further geomagnetic coordinates, the invariant latitudes are mapped in Fig. 23 and the centered-dipole-field geomagnetic latitudes are mapped in Fig. 24.)

Table 10 - S_4 Values Partitioned by Elevation Angle and Time of Day. (Values in parentheses are the maximum file values.)

Time of Day	S_4 Values		
	5° Elevation	14-17° Elevation	All Elevations
Premidnight	0.10 (0.22)	0.18 (0.24)	0.15 (0.24)
Postmidnight	0.20 (0.34)	0.17 (0.26)	0.18 (0.34)
All times	0.13 (0.34)	0.17 (0.26)	0.16 (0.34)

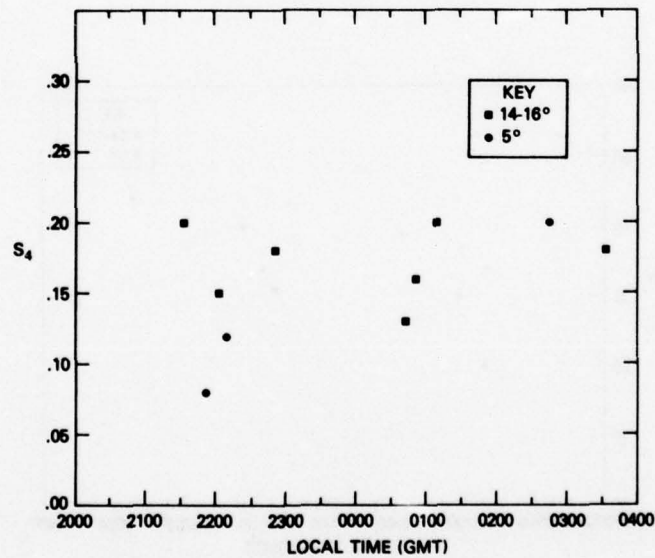


Fig. 16 - Average values of S_4 versus local time

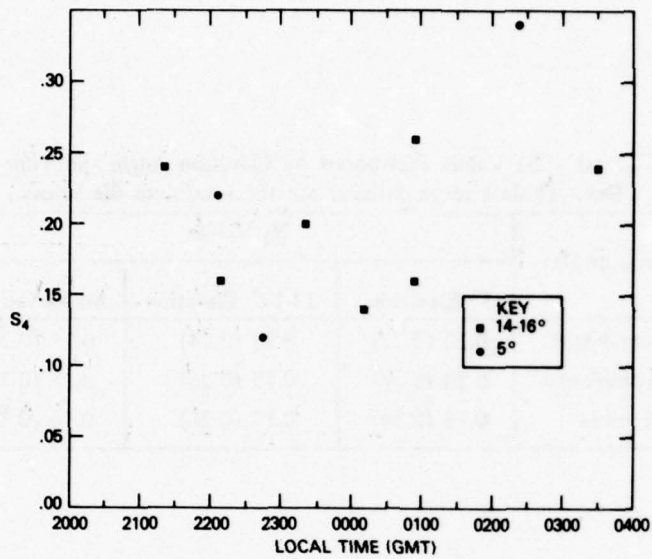


Fig. 17 - Peak values of S_4 versus local time

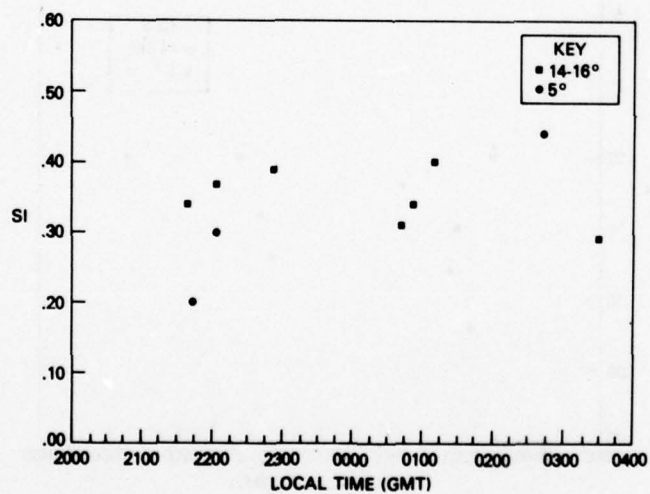


Fig. 18 - Average values of S_1 versus local time

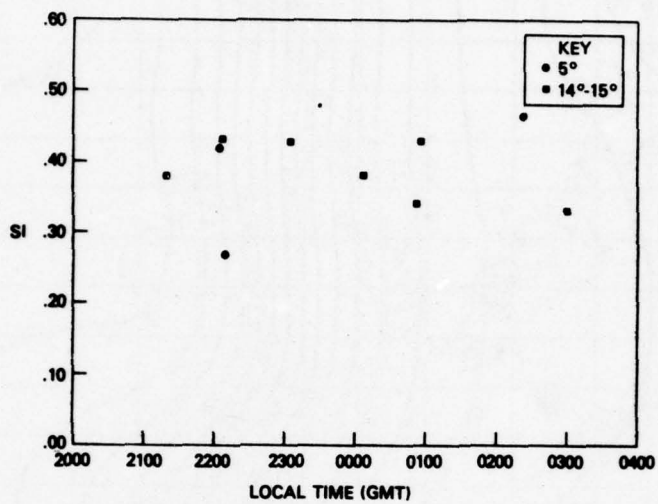


Fig. 19 - Peak values of S/I versus local time

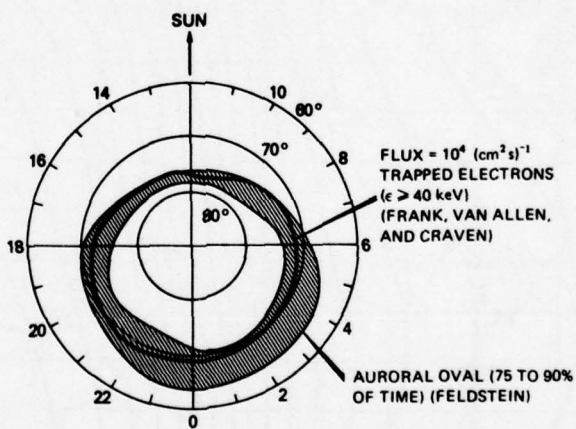


Fig. 20 - The auroral-oval position in magnetic-dipole-latitude and time coordinates. [From S. Akasofu, *Polar and Magnetospheric Substorms*, Springer-Verlag, New York, 1968, p. 7.]

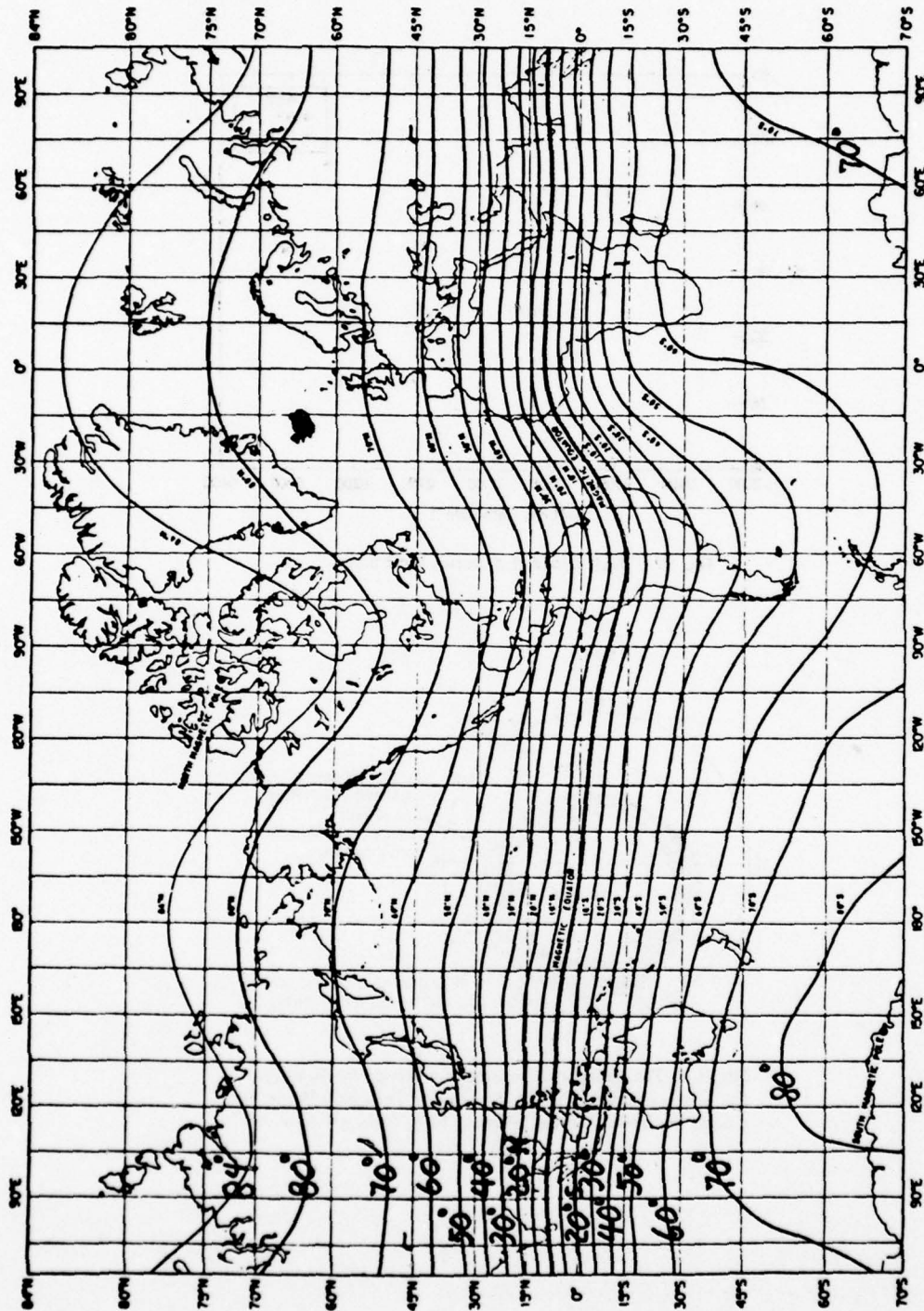


Fig. 21 - World map of the magnetic dip at the earth's surface (epoch 1955) (Navy Oceanographic Office, chart 1700). The dip is roughly 75° at the U.S. Naval Station, Keflavik, Iceland. [From E.K. Smith, Dept. of Commerce technical report 74-186, Nov. 1974, p. 76.]

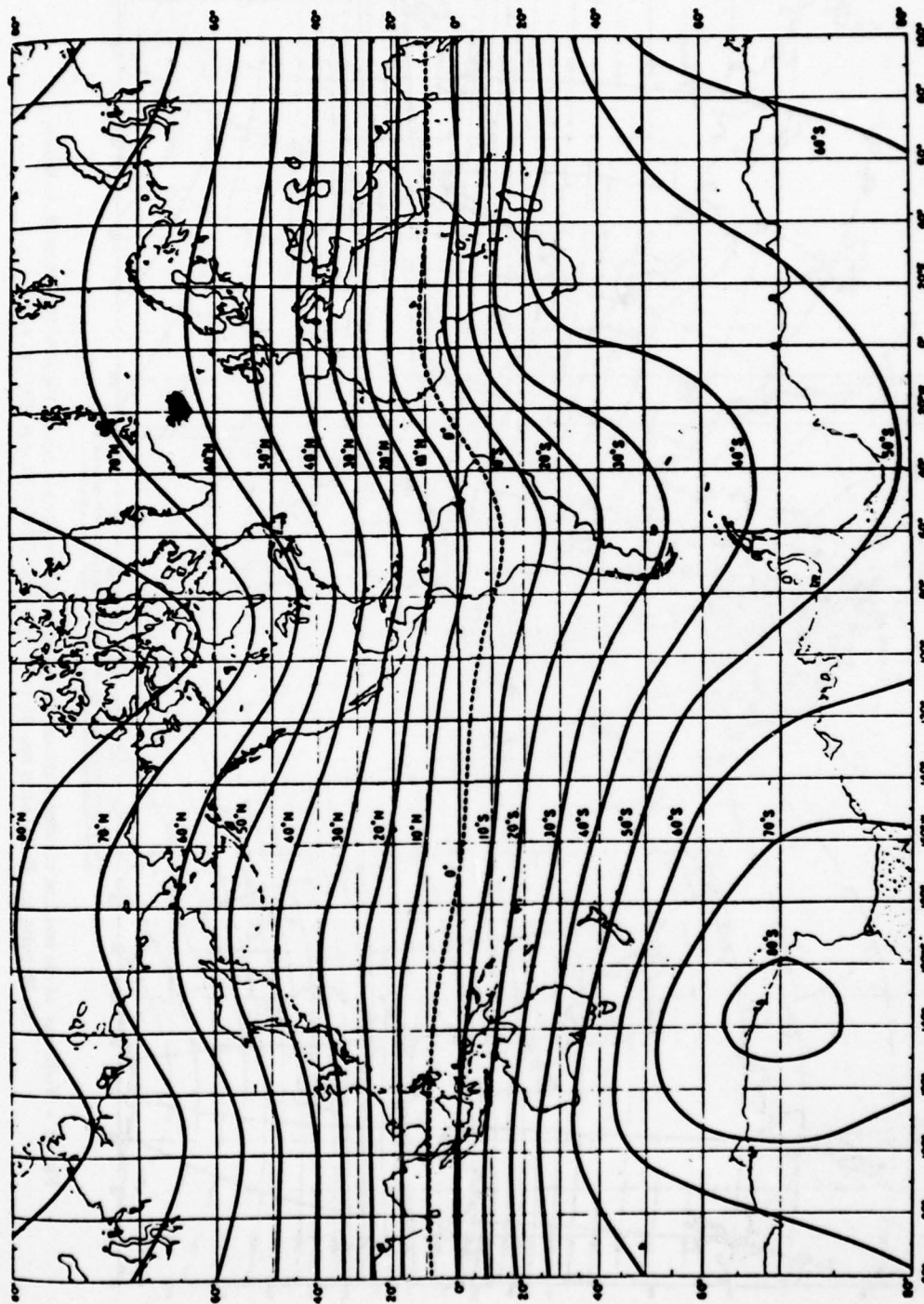


Fig. 22 - Magnetic-dipole latitude (θ) derived from Fig. 21 using the relation $\tan \theta = (1/2) \tan I$, where I is the magnetic dip. The dashed line is the dip equator. Iceland is in solid black. [From E.K. Smith, Dept. of Commerce technical report 74-186, Nov. 1974, p. 77.]

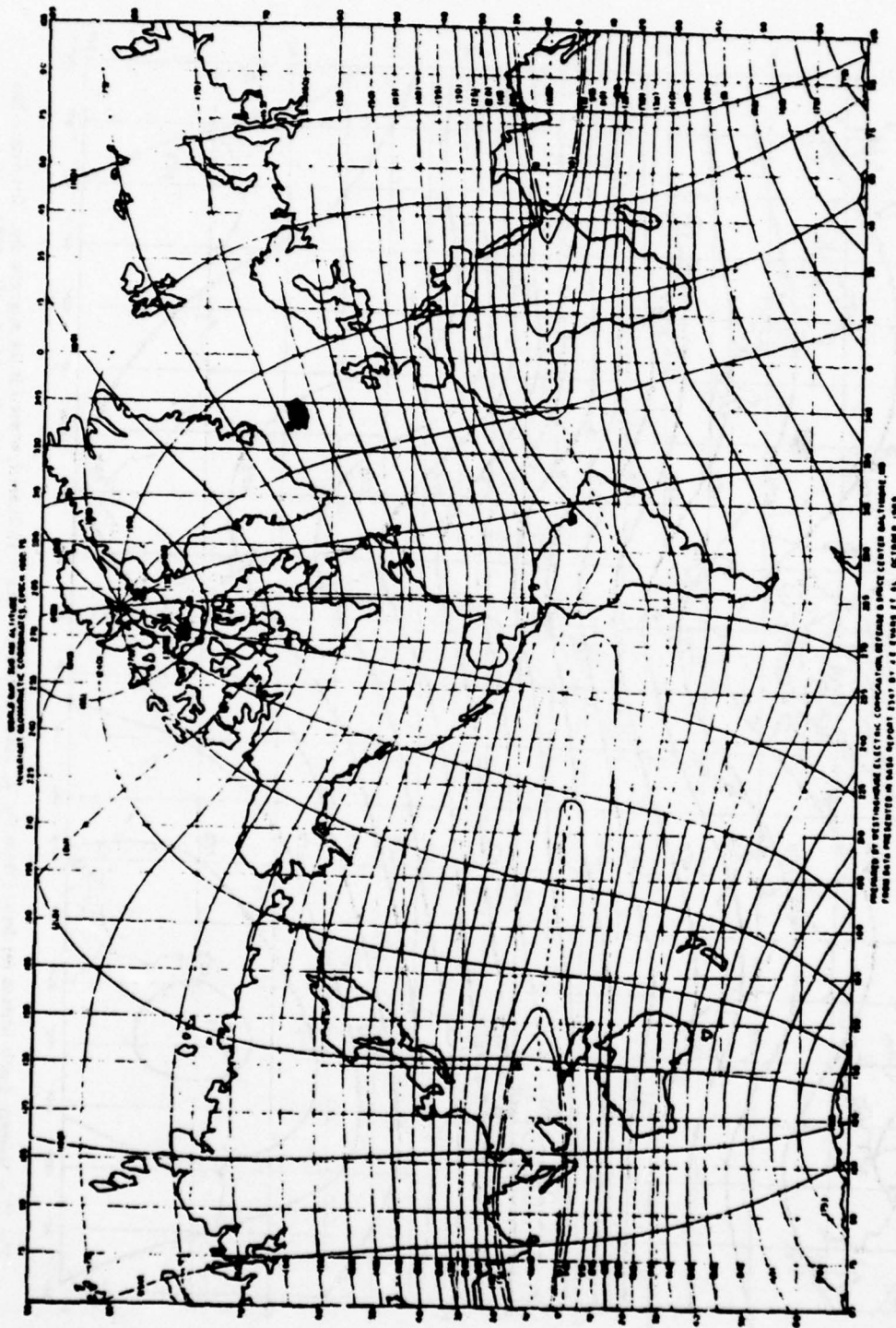


Fig. 23 - World map of the invariant coordinate system referenced to 300-km altitude (epoch 1969-1975). [From W. E. Brown, G. Haroules, and W. I. Thompson, III, DOT report TSC-OST-72-33, Apr. 1973, p. 43.]

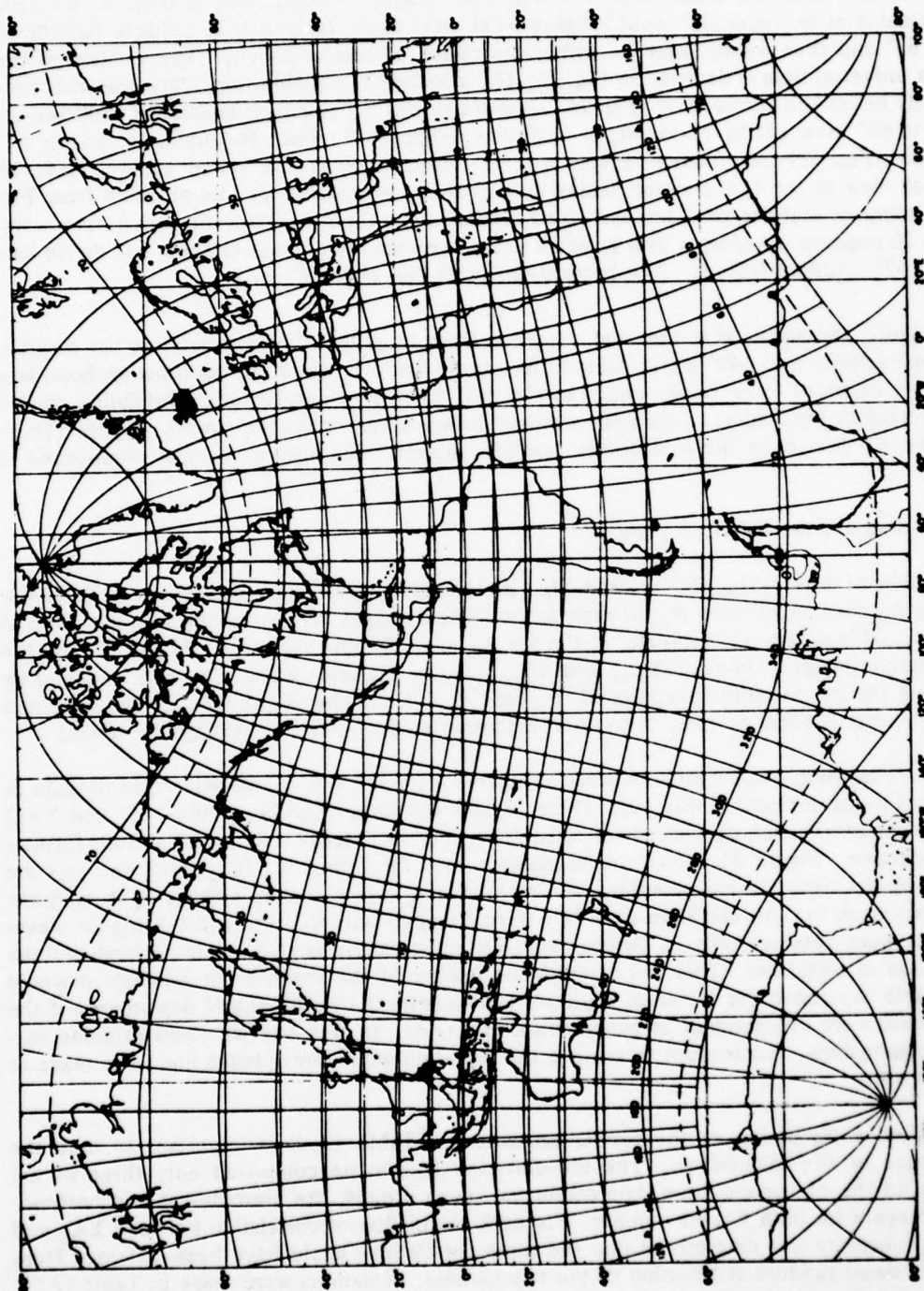


Fig. 24 - World map of the geomagnetic coordinate system (centered dipole field). [From W. E. Brown, G. Haroules, and W. I. Thompson, III, DOT report TSC-OST-72-33, Apr. 1973, p. 42.]

The oval (hatched area) extends to about 65° magnetic-dipole latitude (Fig. 22) by 2200 and remains at or below 65° until roughly 0400 local time. Iceland is at a dipole latitude of about 65° and thus would likely be within the region of auroral activity. The rotation of the oval in universal time is depicted in Fig. 25. The so-called scintillation boundary descends considerably below the auroral oval (Fig. 26). It is roughly at 57° invariant latitude at 2200 and ascends to 60° invariant by midnight; at 0300 it is roughly 62° . Since Iceland is, at roughly 67° invariant (Fig. 23), scintillation effects will be encountered at the Naval station, Keflavik. Another view of the oval position (using auroral forms as tracers) may be obtained from Fig. 27. It suggests that the oval descends for fixed universal times as magnetic activity increases. Figure 20 suggests a midnight oval position (under average conditions) of about 63° dipole latitude or 67° invariant latitude. This is consistent with Fig. 27 for $K_p \approx 3$.

Figure 28a shows that the oval descends from roughly 65° dipole latitude for negligible magnetic activity to $\approx 49^\circ$ dipole latitude for strong activity. Since the scintillation boundary would be expected to be driven ahead of the oval boundary, high-latitude scintillation should be expected at even some midlatitude stations during severe magnetic storms. Figure 28b illustrates the descent of the oval during magnetic storms. The descent is most pronounced at night.

Scintillation and the Indices K_p and R_z

Table 11 lists $S_4 - \max$, $S_4 - \text{av}$, and SI_{av} , the planetary magnetic index K_p , and the planetary Zurich sunspot number R_z for each group. The averages here are group averages (one to six files). \overline{SI} is already an "estimate" of the file average (30 min) using Eqs. (2) and (3) and the block determinations (30 s) of SI_{max} and SI_{min} . SI_{av} is therefore a group average obtained by averaging the estimated file averages \overline{SI} . Figures 29 and 30 show K_p and R_z for the June and the September-October periods. Also indicated are solar-flare effects and magnetic storms.

In developing relationships between the parameters K_p and R_z , we will crosscorrelate in four time-frame formats (Table 12). Table 13 lists the linear regression lines (S_4 and ΣK_p) and the crosscorrelation coefficients of S_4 and ΣK_p for each set of data under all four formats of comparison. Figure 31 shows the regression lines for format 2. In general the sets are defined by the elevation characteristics and whether the peak S_4 or the average S_4 is analyzed. However, since the low-elevation data (5°) were obtained only in June and the higher elevation data were obtained only in October and November, there is also a summer-and-equinox bifurcation of properties. This is a troublesome feature of the analysis. In principle it would be possible to remove the elevation-angle (or equivalently the zenith-angle) dependence if the scintillation were independent of geographical variations. In this way we could examine seasonal relationships. No attempt to remove the elevation-angle dependence has been made as of this writing.

Before a discussion of the results presented in Table 13, it is important to note the significance of the calculations. The low-elevation data alone comprised only three of ten groups, and the higher elevation data comprised seven groups; the premidnight and postmidnight groups were both five in number. For each calculation of correlation between ΣK_p and S_4 the probability was determined that the same correlations could have been obtained from an uncorrelated random distribution of the two variates. Notations were made in Table 13 for a probability $P = 0.1$ and 0.2 .

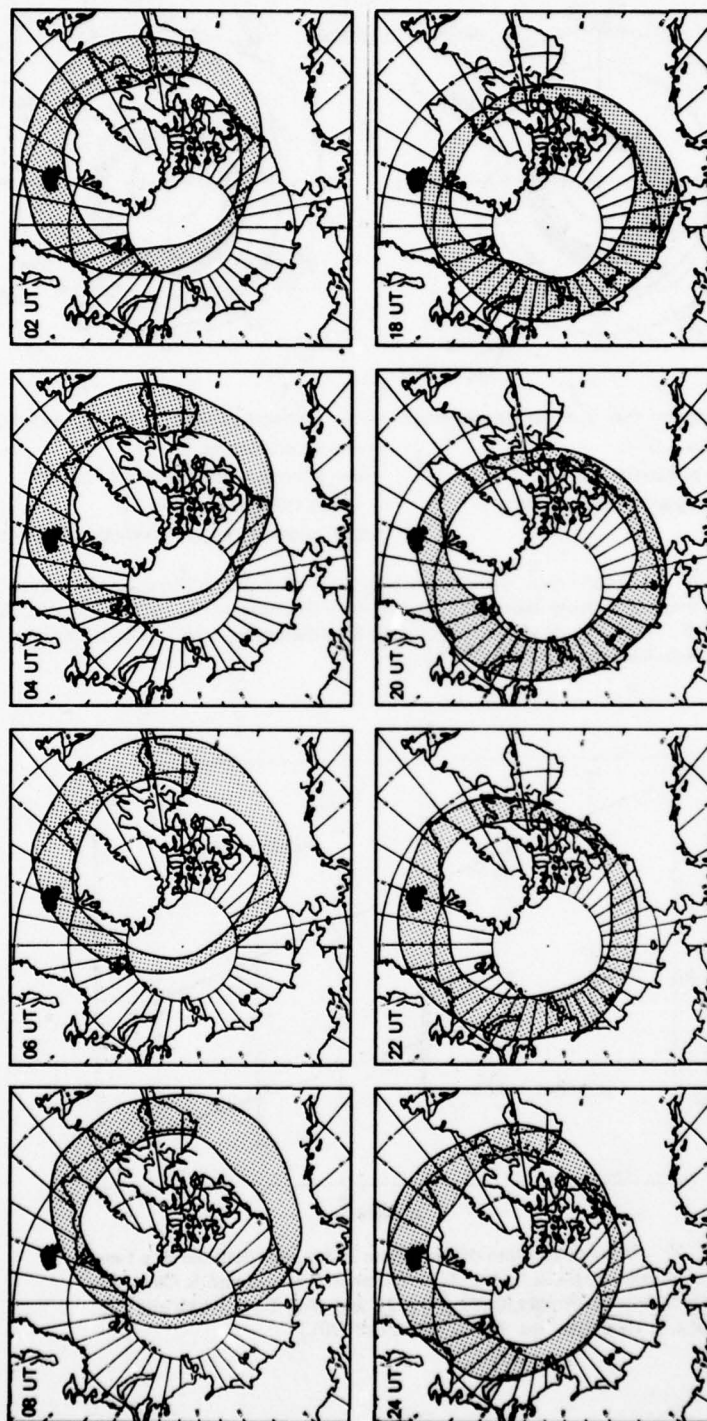


Fig. 25 - Location of the auroral oval (shaded) at fixed values of universal time. Iceland is in solid black. [From S. Akasofu, *Polar and Magnetospheric Substorms*, Springer-Verlag, New York, 1968, pp. 8-10.]

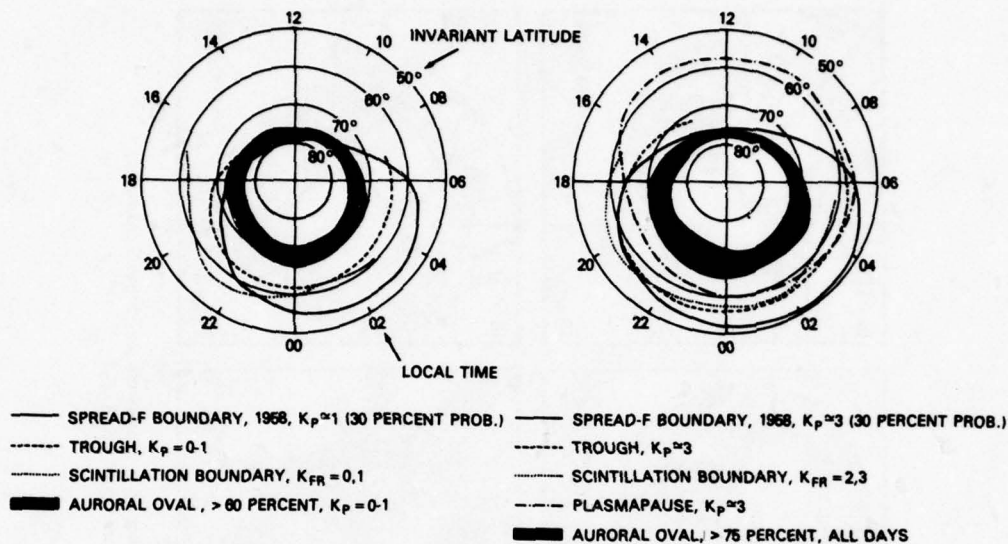


Fig. 26 - Location of the auroral oval, scintillation boundary, midlatitude through, and spread-F boundary. K_p is the planetary magnetic activity index, and K_{FR} is the index obtained at the Fredricksburg Magnetic Observatory. [From E.K. Smith, "A Study of Ionospheric Scintillation as it Affects Satellite Communications," Dept. of Commerce technical report 74-186, 1974.]

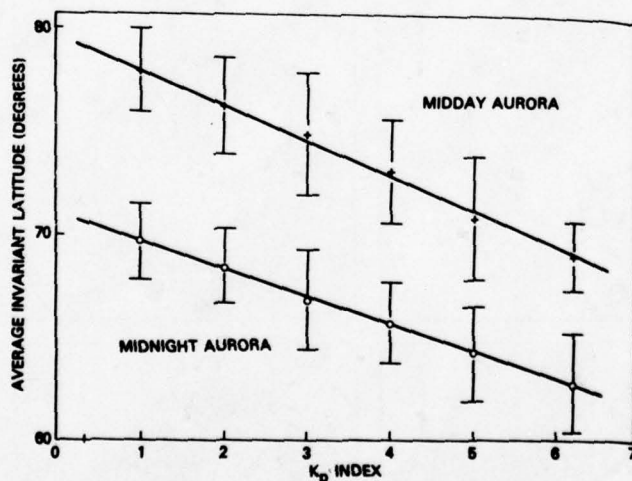


Fig. 27 - Average location of the aurora in invariant latitude as a function of the magnetic index K_p . [From S. Akasofu and S. Chapman, *Solar Terrestrial Physics*, Oxford, 1972), and after T.A. Chubb and G.T. Hicks, *J. Geophys. Res.* 75, 1290-1311 (1970).]

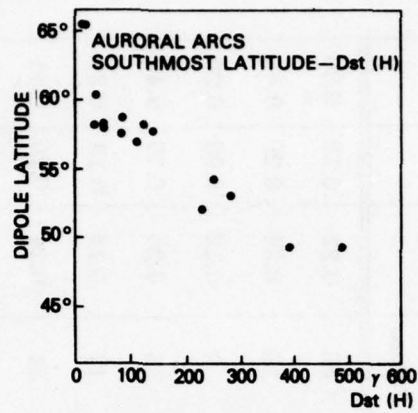


Fig. 28a - Position of the auroral arcs in dipole latitude with the D_{st} index as variable [From S. Akasofu and S. Chapman, *Solar Terrestrial Physics*, Oxford, 1972.]

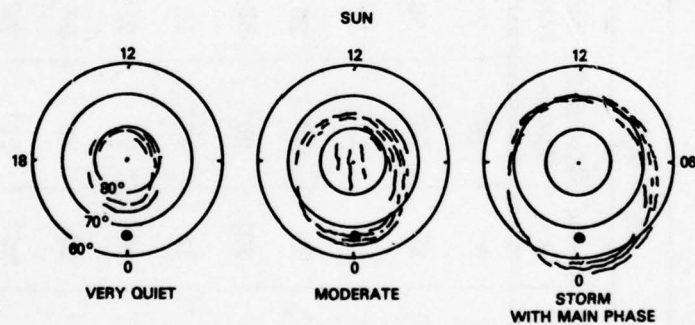


Fig. 28b - Descent of the auroral oval with increasing magnetic activity. [From S. Akasofu, *Polar and Magnetic Substorms*, Springer-Verlag, New York, 1968, p. 18.]

Table 11 — Indices for Each Group. The modified-past, same-day, modified-future and same-period time-frame formats are explained in Table 12.

Group	Date	Time of Day	ΣK_p				R_z			$S_{4-\max}$	$S_{4-\text{av}}$	SI_{av}
			Mod. Past	Same Day	Modified Future	Same Period	Mod. Past	Same Day	Mod. Future			
1	6/23	Premidnight	9 ⁻	9 ⁻	19 ⁺	7 ⁻	23	23	26	0.22	0.12	0.30
2	6/25	Postmidnight	19 ⁺	26 ⁻	26 ⁻	36	26	19	19	0.34	0.20	0.44
3	6/26	Premidnight	13 ⁻	13 ⁻	14 ⁻	19 ⁻	19	19	9	0.12	0.08	0.20
4	9/25	Postmidnight	13 ⁺	30	30	23 ⁻	7	16	16	0.26	0.20	0.40
5	9/26	Postmidnight	30	20 ⁺	20 ⁺	36	16	17	17	0.14	0.13	0.31
6	9/29	Premidnight	18	18	16 ⁺	12	25	25	31	0.24	0.20	0.34
7	9/30	Premidnight	16 ⁺	16 ⁺	21	23 ⁻	31	31	31	0.20	0.18	0.39
8	10/1	Premidnight	21	21	25 ⁺	26 ⁺	31	31	28	0.16	0.15	0.37
9	10/2	Postmidnight	21	25 ⁺	25 ⁺	26 ⁺	31	28	28	0.16	0.16	0.34
10	10/2	Postmidnight	21	25 ⁺	25 ⁺	26 ⁺	31	28	28	0.24	0.18	0.29

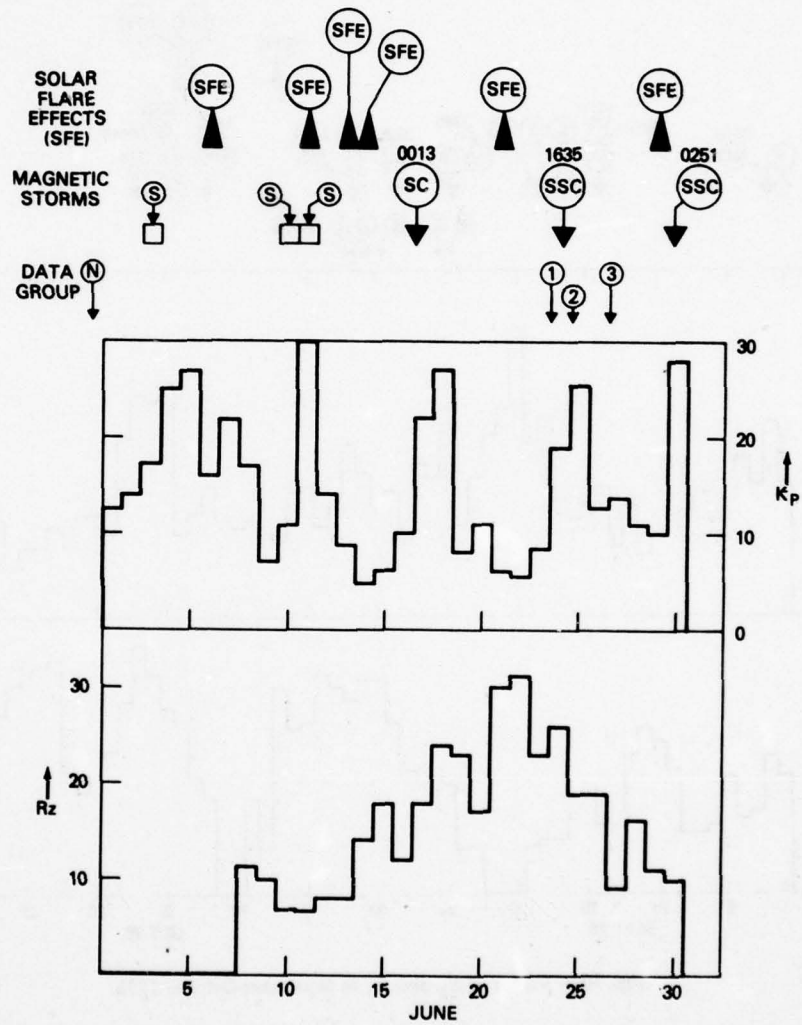


Fig. 29 - Values of the magnetic activity K_p and the solar activity R_z in June 1976. A sudden commencement is denoted by SC. A sudden storm commencement (SSC) is a sudden commencement followed by a magnetic storm or a period of storminess. The term S refers to a magnetic storm period for which there was no sudden storm commencement (SSC).

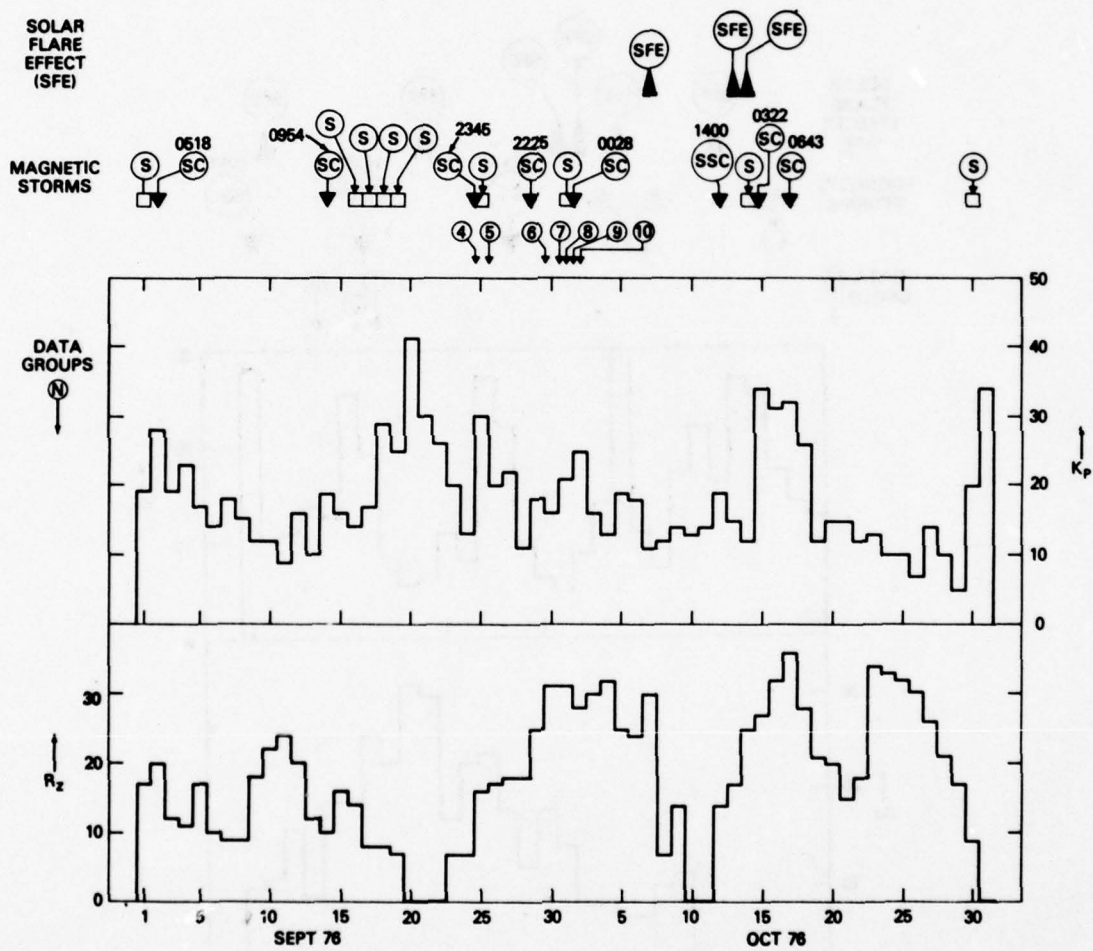


Fig. 30 - Values of K_p and R_z in September-October 1976.

Table 12 — Time-frame Formats Used in Crosscorrelating K_p

Format	Name	S_4 Associations
1	Modified-past ΣK_p	Premidnight: same-day $\sum_{i=1}^8 K_{p,i}$ as observations; day N^* Postmidnight: previous-day $\sum_{i=1}^8 K_{p,i}$ as observations; day N
2	Same-day ΣK_p	Premidnight: same-day $\sum_{i=1}^8 K_{p,i}$ as observations; day Postmidnight: same-day $\sum_{i=1}^8 K_{p,i}$ as observations; day $N+1$.
3	Same-period ΣK_p	All: $4[K_{p,8}(N) + K_{p,1}(N+1)]$.
4	Modified-future ΣK_p	Premidnight: next-day $\sum_{i=1}^8 K_{p,i}$ as observations; day $N+1$. Postmidnight: same-day $\sum_{i=1}^8 K_{p,i}$ as observations; day $N+1$.

*Day N = Premidnight Greenwich day;
 day $N+1$ = Postmidnight Greenwich day.

Table 13 - Relationships Between the S_4 Index and ΣK_p

Set	Characteristic	S_4	Correlation
S_4 Index and ΣK_p Relationships (Format 1)			
A ₁	Low elevation; max S_4	$0.04 + 13.9 \times 10^{-3} \Sigma K_p$	+0.64
B ₁	High elevation; max S_4	$0.33 - 6.6 \times 10^{-3} \Sigma K_p$	-0.75
C ₁	Low elevation; av S_4	$0.01 + 8.9 \times 10^{-3} \Sigma K_p$	+0.74
D ₁	High elevation; av S_4	$0.26 - 4.44 \times 10^{-3} \Sigma K_p$	-0.87*
E ₁	All elevations; max S_4	$0.25 - 2.56 \times 10^{-3} \Sigma K_p$	-0.23
F ₁	All elevations; av S_4	$0.15 + 7.49 \times 10^{-4} \Sigma K_p$	+0.11
S_4 Index and ΣK_p Relationships (Format 2)			
A ₂	Low elevation; max S_4	$0.09 + 9.2 \times 10^{-3} \Sigma K_p$	+0.72
B ₂	High elevation; max S_4	$0.12 + 3.46 \times 10^{-3} \Sigma K_p$	+0.35
C ₂	Low elevation; av S_4	$0.05 + 5.2 \times 10^{-3} \Sigma K_p$	+0.81
D ₂	High elevation; av S_4	$0.15 + 1.14 \times 10^{-3} \Sigma K_p$	+0.21
E ₂	All elevations; max S_4	$0.13 + 3.84 \times 10^{-3} \Sigma K_p$	+0.38
F ₂	All elevations; av S_4	$0.08 + 4.04 \times 10^{-3} \Sigma K_p$	+0.66
S_4 Index and ΣK_p Relationships (Format 3)			
A ₃	Low elevation; max S_4	$0.13 + 4.72 \times 10^{-3} \Sigma K_p$	+0.63
B ₃	High elevation; max S_4	$0.31 - 4.47 \times 10^{-3} \Sigma K_p$	-0.66
C ₃	Low elevation; av S_4	$0.07 + 3.04 \times 10^{-3} \Sigma K_p$	+0.73
D ₃	High elevation; av S_4	$0.25 - 3.08 \times 10^{-3} \Sigma K_p$	-0.84*
E ₃	All elevations; max S_4	$0.19 + 5.92 \times 10^{-4} \Sigma K_p$	+0.08
F ₃	All elevations; av S_4	$0.14 + 8.98 \times 10^{-4} \Sigma K_p$	+0.20
S_4 Index and ΣK_p Relationships (Format 4)			
A ₄	Low elevation; max S_4	$-0.13 + 1.83 \times 10^{-2} \Sigma K_p$	+1.00†
B ₄	High elevation; max S_4	$0.15 + 1.95 \times 10^{-3} \Sigma K_p$	+0.19
C ₄	Low elevation; av S_4	$-0.07 + 1.01 \times 10^{-2} \Sigma K_p$	+1.00†
D ₄	High elevation; av S_4	$0.16 + 4.77 \times 10^{-4} \Sigma K_p$	+0.08
E ₄	All elevations; max S_4	$0.07 + 6.2 \times 10^{-3} \Sigma K_p$	+0.47
F ₄	All elevations; av S_4	$0.05 + 4.84 \times 10^{-3} \Sigma K_p$	+0.60

*Significant at probability $p < 0.20$ (the probability is less than 20% that the observed correlation could have been obtained from a random population).

†Significant at $p < 0.10$.

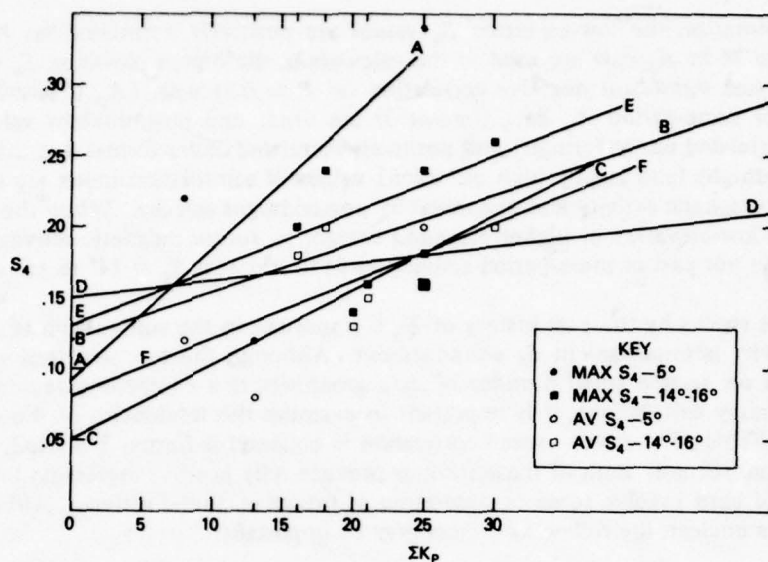


Fig. 31 — S_4 values versus ΣK_p . The associations are based on eight 3-hour values of K_p which occur on the universal day on which the scintillation data were obtained.

Only the low-elevation data using format 4 yielded significant (positive) correlation between ΣK_p and S_4 at the $P = 0.1$ level. However at the $P = 0.2$ level the higher elevation data suggested significant (negative) correlation between ΣK_p and S_4 (average) for formats 1 and 3. Table 14 shows the relationships between the average S_4 and ΣK_p and their crosscorrelation coefficients using premidnight and postmidnight as the partitioning function. The postmidnight data are negatively correlated with past (preceding) values of ΣK_p (format 1) but positively correlated with future (following) values of ΣK_p (format 4). Furthermore, these correlations are significant at $P = 0.1$; so there is at least 90% probability that they are real. The premidnight correlations are insignificant even at the 0.2 level. Also, four out of the five groups of postmidnight data were obtained at the higher elevation.

Table 14 — Relationship Between the Average S_4 and ΣK_p When the Data are Partitioned Into Premidnight Data and Postmidnight Data

Format	S_4		Crosscorrelation Coefficient r	
	Premidnight	Postmidnight	Premidnight	Postmidnight
1: past 24 hr	$0.05 + 6 \times 10^{-2} \Sigma K_p$	$0.27 - 4.4 \times 10^{-3} \Sigma K_p$	+0.58	-0.91*
3: same period	$0.14 + 4 \times 10^{-4} \Sigma K_p$	$0.22 - 1.7 \times 10^{-3} \Sigma K_p$	+0.07	-0.35
4: future 24 hr	$0.08 + 3.51 \times 10^{-3} \Sigma K_p$	$-7.01 + 7.4 \times 10^{-2} \Sigma K_p$	+0.32	+0.89*

*Significant at $P < 0.1$.

To summarize, the low-elevation S_4 values are positively correlated (at $P \approx 0.1$) with ΣK_p if future-24-hr K_p data are used in the calculation, the higher elevation S_4 values exhibit a somewhat less significant negative correlation (at $P \approx 0.2$) with ΣK_p if past-24-hr K_p data (format 1) or same-period K_p data (format 3) are used; and postmidnight values of S_4 are negatively correlated under format 1 and positively correlated under format 4 at the $P \approx 0.1$ level. Thus postmidnight (and largely high elevation) values of scintillation index are suppressed by premidnight magnetic activity and enhanced by postmidnight activity. When the S_4 values are grouped into low-elevation or higher elevation categories, future magnetic activity enhances S_4 at 5° elevation but past or same-period activity tends to suppress S_4 at 14° to 16° elevation.

It is not clear why the past history of K_p is important in the suppression of S_4 or why future K_p activity is important in S_4 enhancement. Although the low statistical significance of results based on such a small number of data groupings is a compelling reason to disregard these preliminary calculations, it is important to examine the tendencies of the data. For example, from Table 13 the best overall correlation is obtained if format 2 is used; however format 4 is a close second. Both of these formats produce only positive regression lines linking S_4 and ΣK_p , and both involve some consideration of future magnetic activity. Although the reason for this is unclear, the following factors may be important:

- Planetary magnetic activity is being compared with local scintillation indices;
- The averaging intervals for K_p may not be optimum;
- The intrinsic physics governing the onset of scintillation may be distinct from (but related with) that which produces magnetic activity.

With regard to the first factor, planetary activity may conceivably be more sluggish than local magnetic activity at the polar regions. This would lead to future values of ΣK_p being more closely tied to S_4 in the polar regions. Another factor is that the polar-cap-absorption (PCA) events generally precede the SSC events. Thus precipitation of highly energetic particles may be a factor in scintillation occurrences which precede magnetic storms and the concomitant substorm and auroral development. It has been suggested that precipitation is the mechanism for high-latitude scintillation. The less energetic plasma cloud, known as the disturbance corpuscular flux, compresses the magnetosphere on the dayside, causing an enhancement in the magnetic field, called the initial phase of the storm, which lasts for 1 to 3 hr in general. Subsequently the disturbance-ring magnetic field produces a reduction in the horizontal component of the earth's field, called the main phase of the storm. The disturbance-ring field arises from a new ring current produced by particles which enter the outer Van Allen belt from the magnetotail. During magnetic storms, rapid fluctuations in the vertical (Z) and horizontal (H) components of the field are observed, along with fluctuations in the field orientation (D). (Magnetic activity is an indication of current flow at very high altitudes; it is not necessarily related to ionospheric electron density fluctuations which are responsible for scintillation.)

Figures 32 through 39 are magnetometer data from the Leirvogur Magnetic Observatory of the University of Iceland, Reykjavik, Iceland, at $64^\circ 11'N$, $21^\circ 42'W$. Also indicated on the figures are the various observation groups discussed in this report. The correlation between magnetic-field fluctuations (in H or Z coordinates) and S_4 indices is not sharp. However more S_4 data are needed during less active periods.

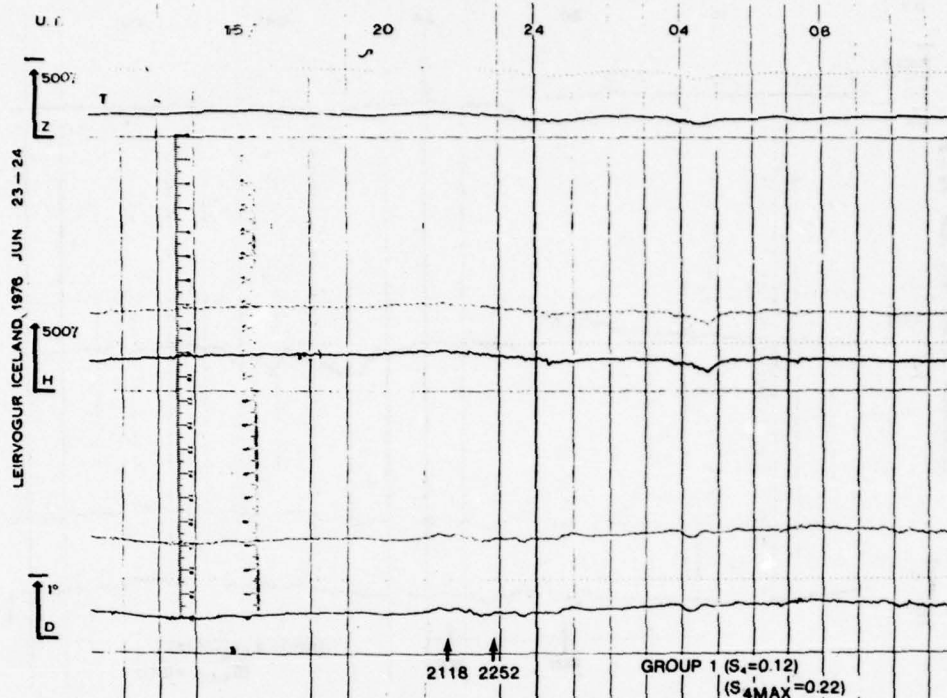


Fig. 32 - Magnetograph data from the Leirvogur Magnetic Observatory, Iceland, June 23 and 24, 1976. These data correspond to group 1, for which $S_4 = 0.12$ and $S_{4-max} = 0.22$.

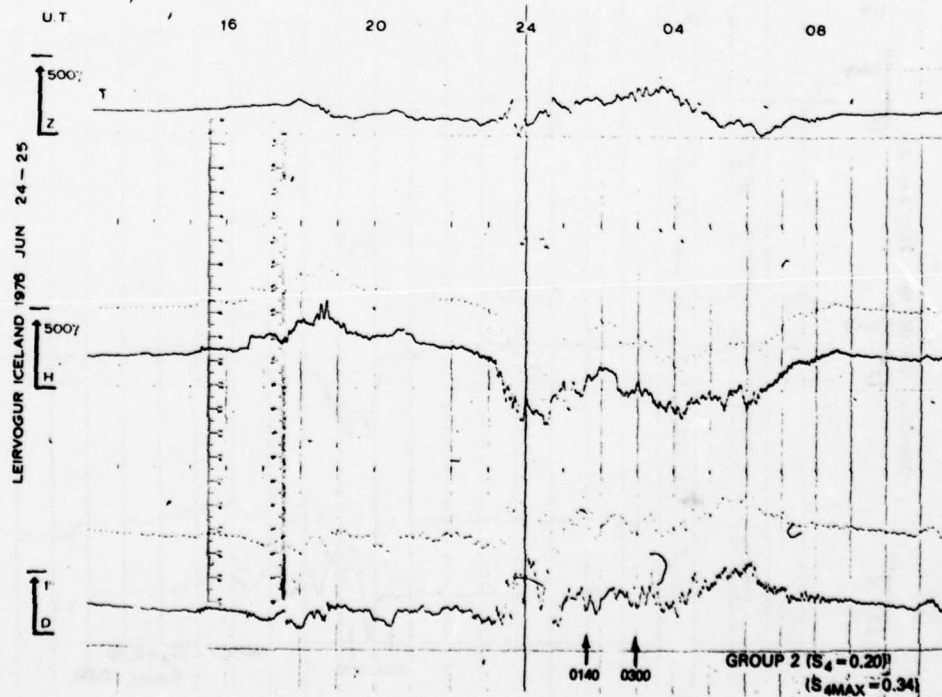


Fig. 33 - Magnetograph data for group 2 ($S_4 = 0.20$; $S_{4-max} = 0.34$)

GOODMAN, MYERS, WATKINS, AND HOGG

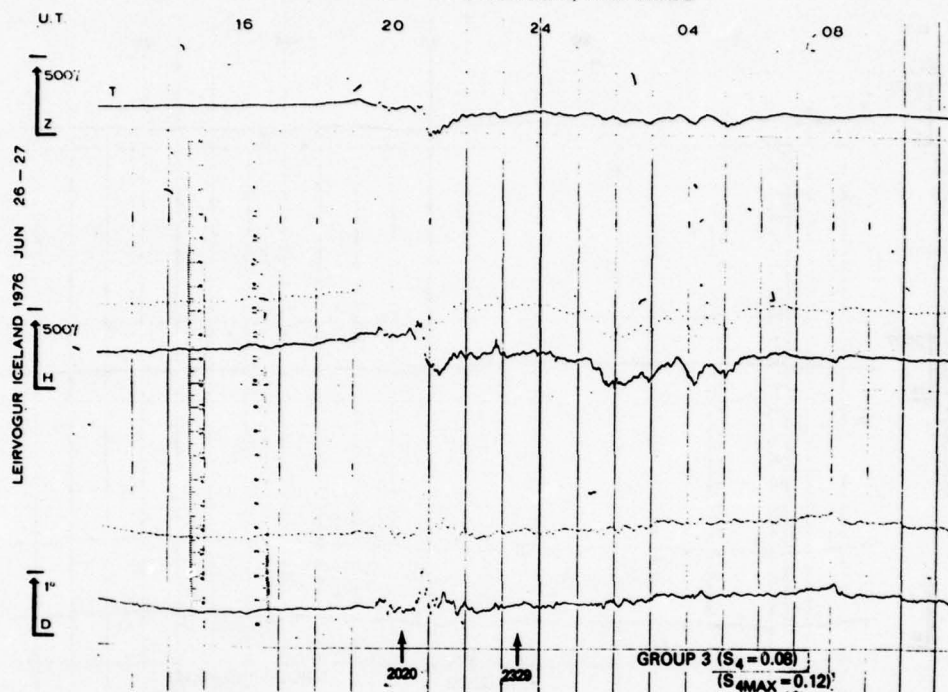


Fig. 34 - Magnetograph data for group 3 ($S_4 = 0.08$; $S_{4-max} = 0.12$)

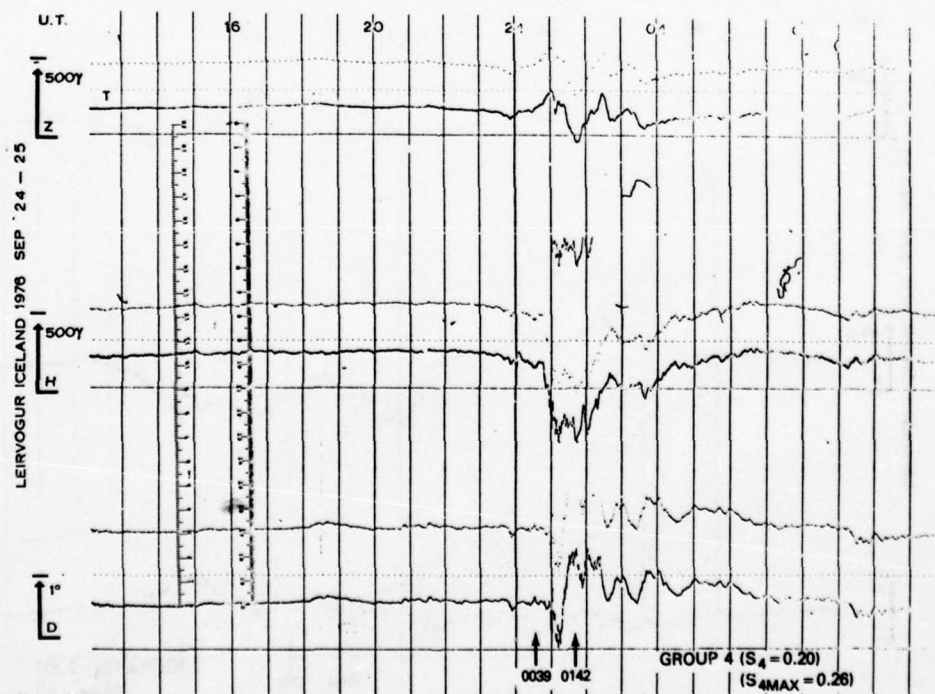


Fig. 35 - Magnetograph data for group 4 ($S_4 = 0.20$; $S_{4-max} = 0.26$)

NRL REPORT 8160

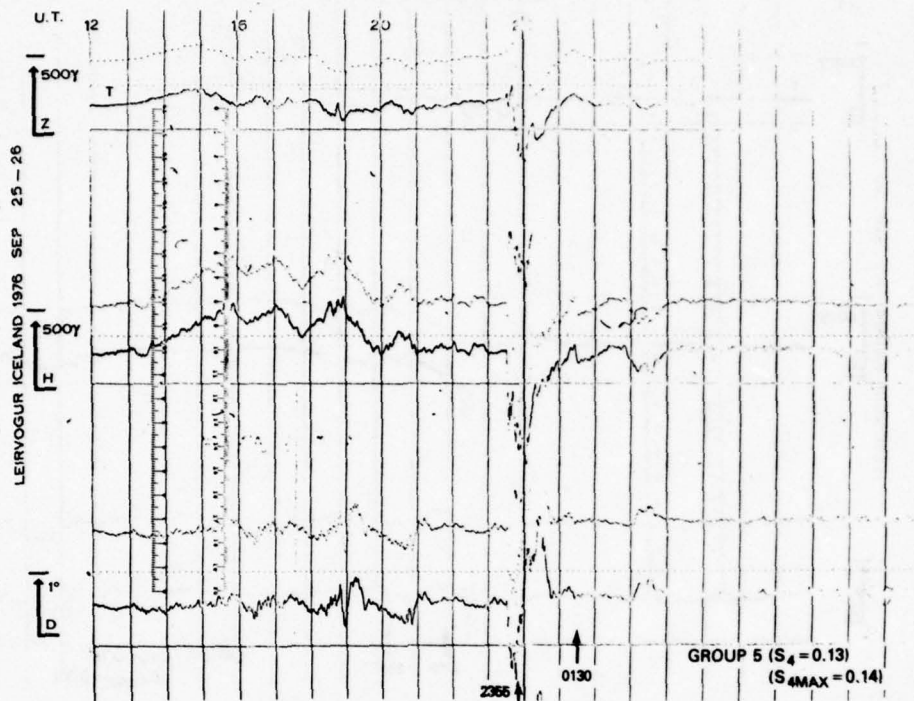


Fig. 36 - Magnetograph data for group 5 ($S_4 = 0.13$; $S_{4-max} = 0.14$)

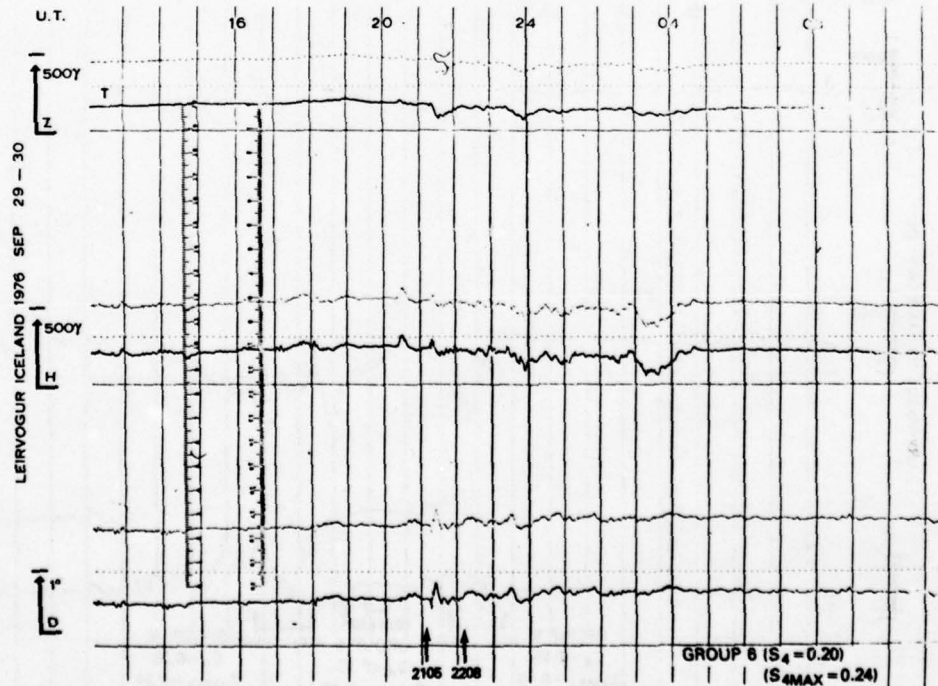


Fig. 37 - Magnetograph data for group 6 ($S_4 = 0.20$; $S_{4-max} = 0.24$)

GOODMAN, MYERS, WATKINS, AND HOGG

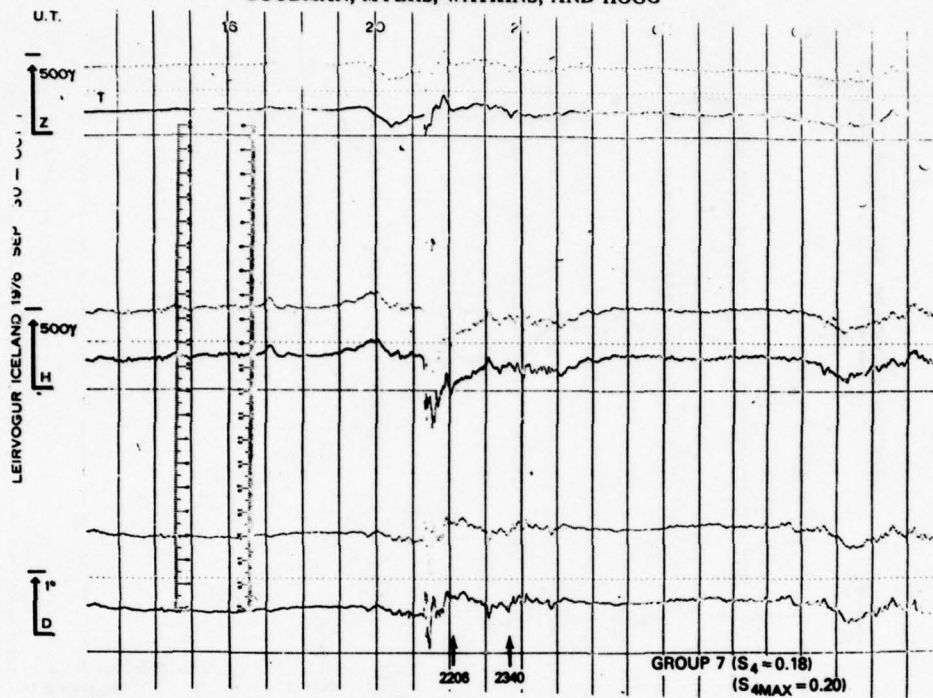


Fig. 38 - Magnetograph data for group 7 ($S_4 = 0.18$; $S_{4-max} = 0.20$)

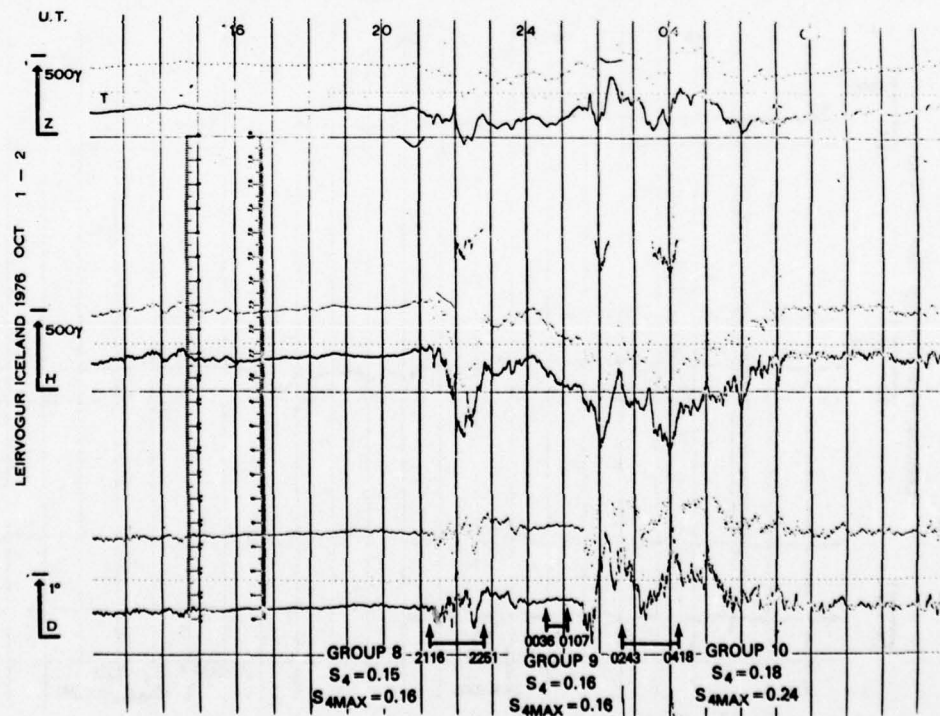


Fig. 39 - Magnetograph data for groups 8, 9, and 10 ($S_4 = 0.15, 0.16$, and 0.18 ;
 $S_{4-max} = 0.16, 0.16$ and 0.24 respectively)

With regard to the planetary Zurich sunspot number R_z , Table 15 indicates the deduced S_4 functions and the crosscorrelation between S_4 and R_z using format 1 (past data). Figure 40 exhibits the result also for format 1, but for low elevation (5°) only. Thus for low-elevation data previous values of K_p and R_z both significantly enhance S_4 . For higher elevation data there is no significant R_z correlation with S_4 , whereas the K_p correlations are mixed (Tables 13 and 14). (Again, "summer" can be substituted for "low elevation", and "fall equinox" can be substituted for "higher elevation".)

Table 15 — Relation Between the Average S_4 and R_z (Format 1: Past 24 Hr)

Elev (deg)	S_4	Correlation
5	$-0.25 + 1.68 \times 10^{-2} R_z$	+0.96*
14-16	$0.18 - 4.3 \times 10^{-4} R_z$	-0.16
All	$0.15 + 5.69 \times 10^{-4} R_z$	+0.11

*Significant at $P \leq 0.1$.

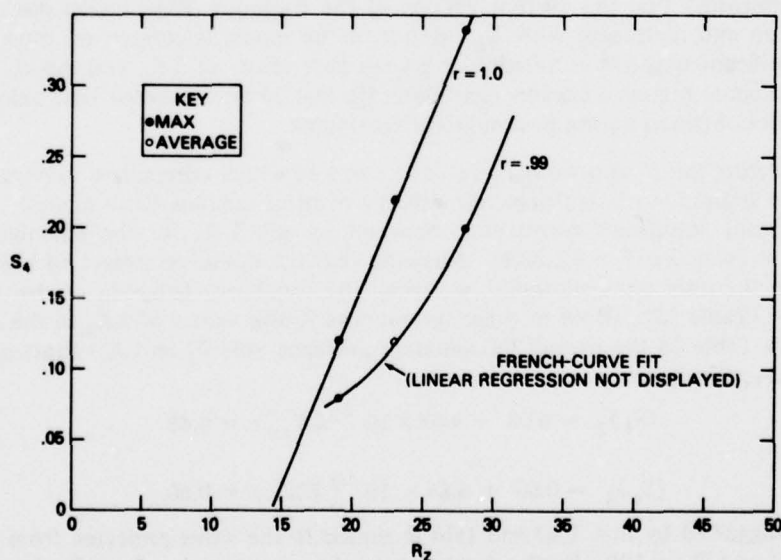


Fig. 40 — Average and maximum S_4 versus R_z for groups in which the elevation angle was 5° (r is the correlation coefficient)

Comparison of S_4 Indices With Other Models

No detailed comparison of the derived S_4 (or SI) indices have been made as of this writing. Figures 41 through 44 are plots of the S_4 index for 140 MHz at local midnight under the assumption that the source satellite is located at 0° latitude on the Greenwich Meridian. Within the circle in the figures are the model projections of the S_4 indices to be obtained at Keflavik at 140 MHz for sunspot numbers (R_z) of 0 (Fig. 41 and 42) and 100 (Figs. 43 and 44). Other assumptions are indicated in the figures. The model is due to Fremouw and Rino and is described in a report by Goodman and Myers*. The displayed projections take no account of K_p variations, although such modifications have been incorporated into the code discussed in the report cited by the footnote. No readings of S_4 are available from the charts for $R_z = 0$ (S_4 being below 0.06); hence we will use the $R_z = 100$ curves for projection (Figs. 43 and 44). For $R_z = 100$ and at 65°N , 23°W , S_4 ranges between 0.21 and 0.35, the latter value being estimated for the low-elevation case. There is little difference between the summer or equinox conditions near the region of interest.

But the frequency for the current observation was 360 MHz rather than 140 MHz. Using $S_4 \propto f^{-1.5}$ (as predicted by a three-dimensional inhomogeneity wavenumber spectrum $P(k)$ having a power-law behavior of k^{-4}), we find from the model in which R_z is taken to be 100 that the 360-MHz range of S_4 indices should be approximately 0.05 to 0.08. The actual observed average range of S_4 (for higher and low elevations respectively) was approximately 0.13 to 0.17. Thus the observed indices were about twice those predicted by the model, even though the liberal value of 100 for R_z which was employed in the estimation was not realized. R_z ranged between 16 and 31 during the period of observation, the average being about 25 for the equinoctial higher elevation data groups and 20 for summer low-elevation data groups.) Clearly the model requires that the S_4 range be less than 0.05 and 0.08. The burden is shifted to K_p to compensate for the difference between the model projections and the actual observations. It is noteworthy that the current version of the Fremouw-Rino model discards R_z for the S_4 prediction and replaces it with K_p . Hence, if the model is correct, we must reject the statistically significant negative correlations between past values of ΣK_p and the S_4 values obtained for equinoctial higher elevation conditions (format 1) and between past values of ΣK_p and the S_4 values obtained during postmidnight conditions.

Thus, rejecting the S_4 functions in Tables 13 and 14 which correspond to negative values of r (an ad-hoc assumption based upon the efficacy of the Fremouw-Rino model), we are left with no statistically significant correlations between S_4 and ΣK_p for the equinoctial higher elevation data at even the $P = 0.2$ level. Allowing that the model is correct and that positive correlations are the only ones allowable, we recall the consistent behavior of the r values in formats 2 and 4 (Table 13). (Both of these formats use future values of ΣK_p in the correlation analysis.) From Table 13 the overall (all-situation averages, sets F_2 and F_4) functions for formats 2 and 4 respectively are

$$(S_4)_2 = 0.08 + 4.04 \times 10^{-3} \Sigma K_p; r = 0.66 \quad (5a)$$

and

$$(S_4)_4 = 0.05 + 4.84 \times 10^{-3} \Sigma K_p; r = 0.60. \quad (5b)$$

The S_4 range suggested by Eqs. (5a) and (5b) is similar to the value projected from the model taking $\Sigma K_p = 0$ and $R_z = 100$. Furthermore, taking the average value for ΣK_p during the observations (modified future or format 4) to be 24 (Table 11), and using Eq. (5b), we have

$$S_4 = 0.17.$$

*J.M. Goodman and C. Myers, "Computer Codes for Use in Display of Predicted Scintillation Characteristics and Total Electron Content," NRL Memorandum Report 3397, 1976.

NRL REPORT 8160

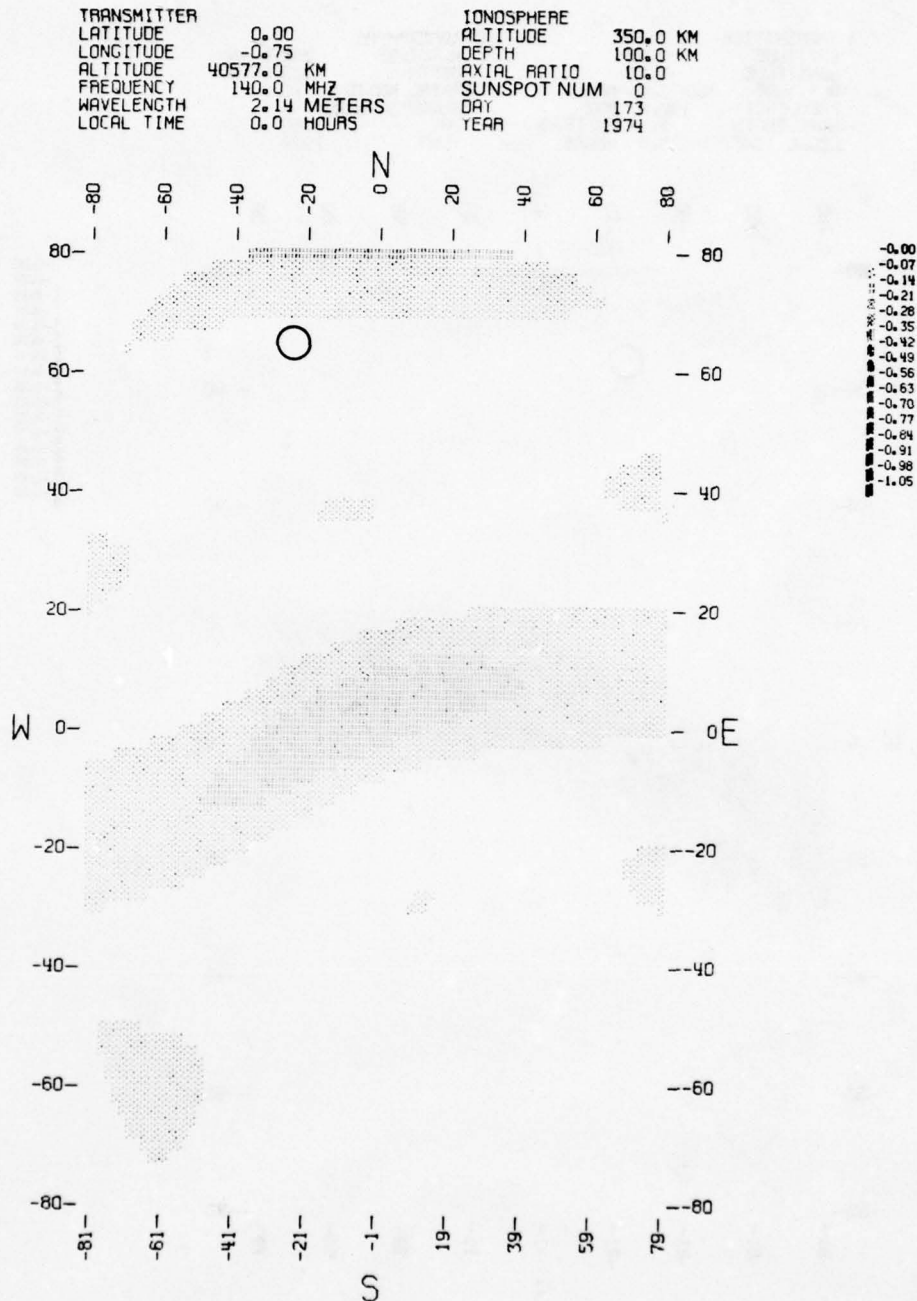


Fig. 41 - Scintillation index map (sunspot number = 0; summer). The center of the circle is the approximate location of Keflavik, Iceland (23°W, 65°N).

GOODMAN, MYERS, WATKINS, AND HOGG

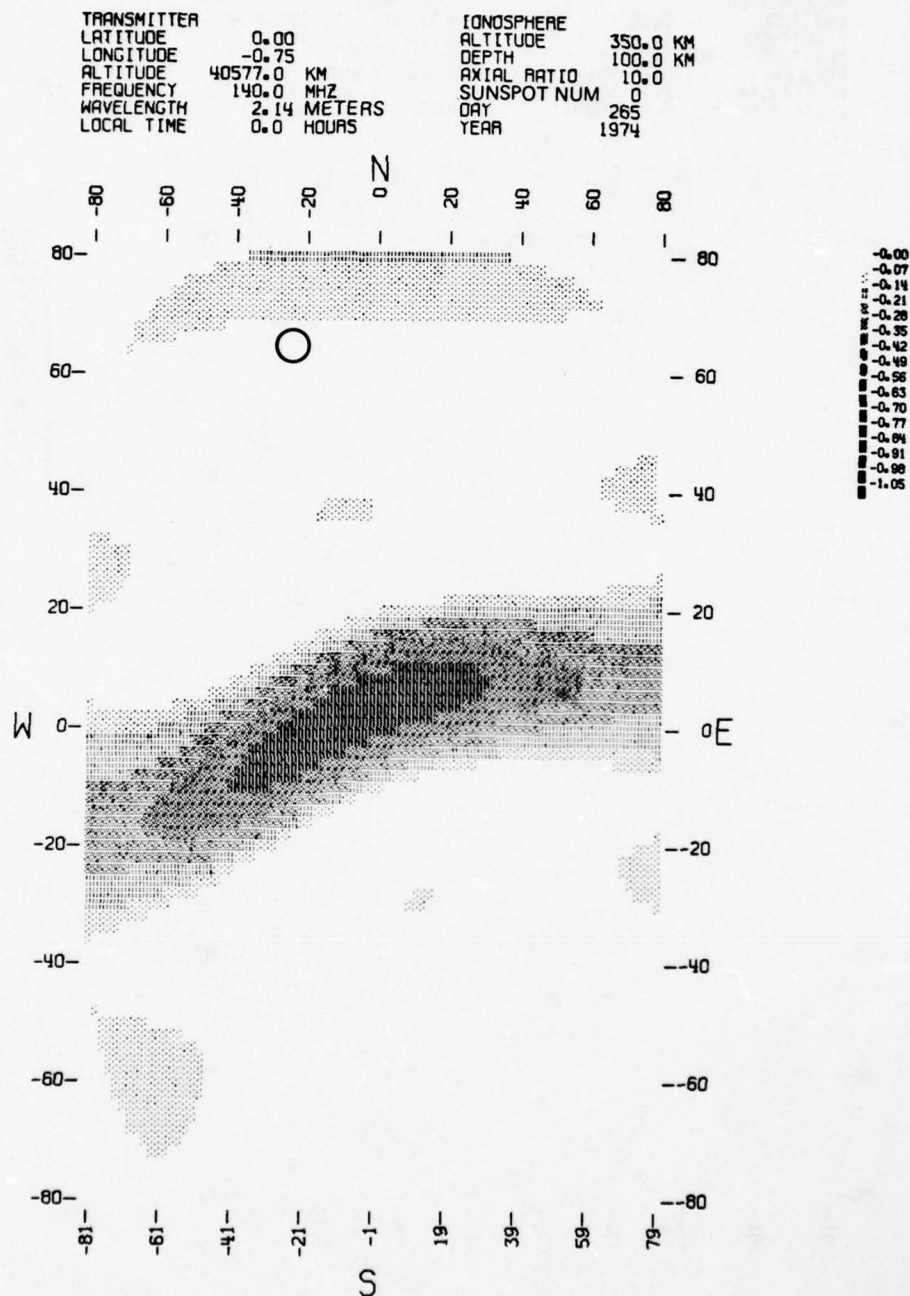


Fig. 42 - Scintillation index map. (sunspot number = 0; autumnal equinox). The center of the circle is the approximate location of Keflavik, Iceland (23°W, 65°N).

NRL REPORT 8160

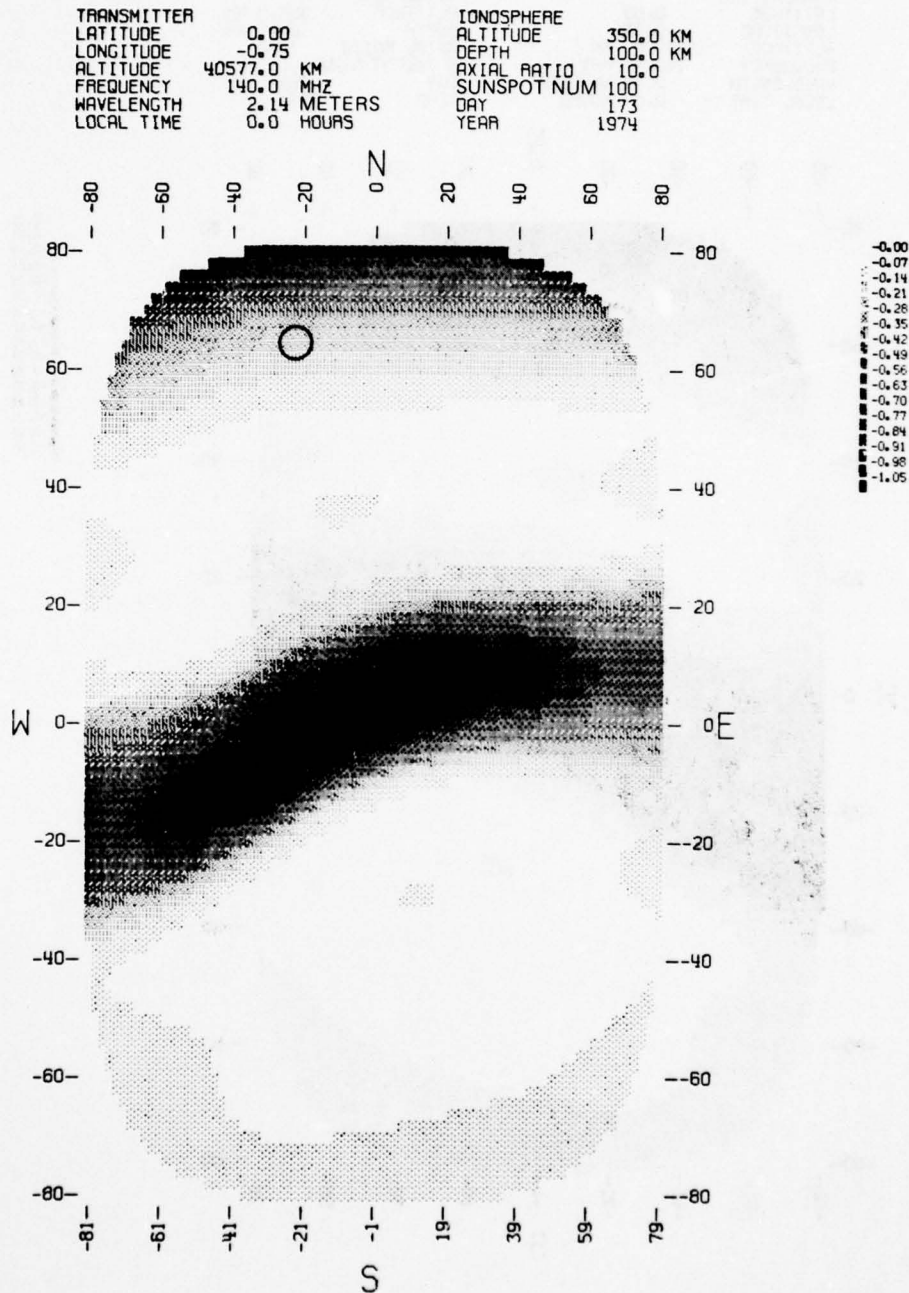


Fig. 43 - Scintillation index map (sunspot number = 100; summer). The center of the circle is the approximate location of Keflavik, Iceland (23°W, 65°N).

GOODMAN, MYERS, WATKINS, AND HOGG

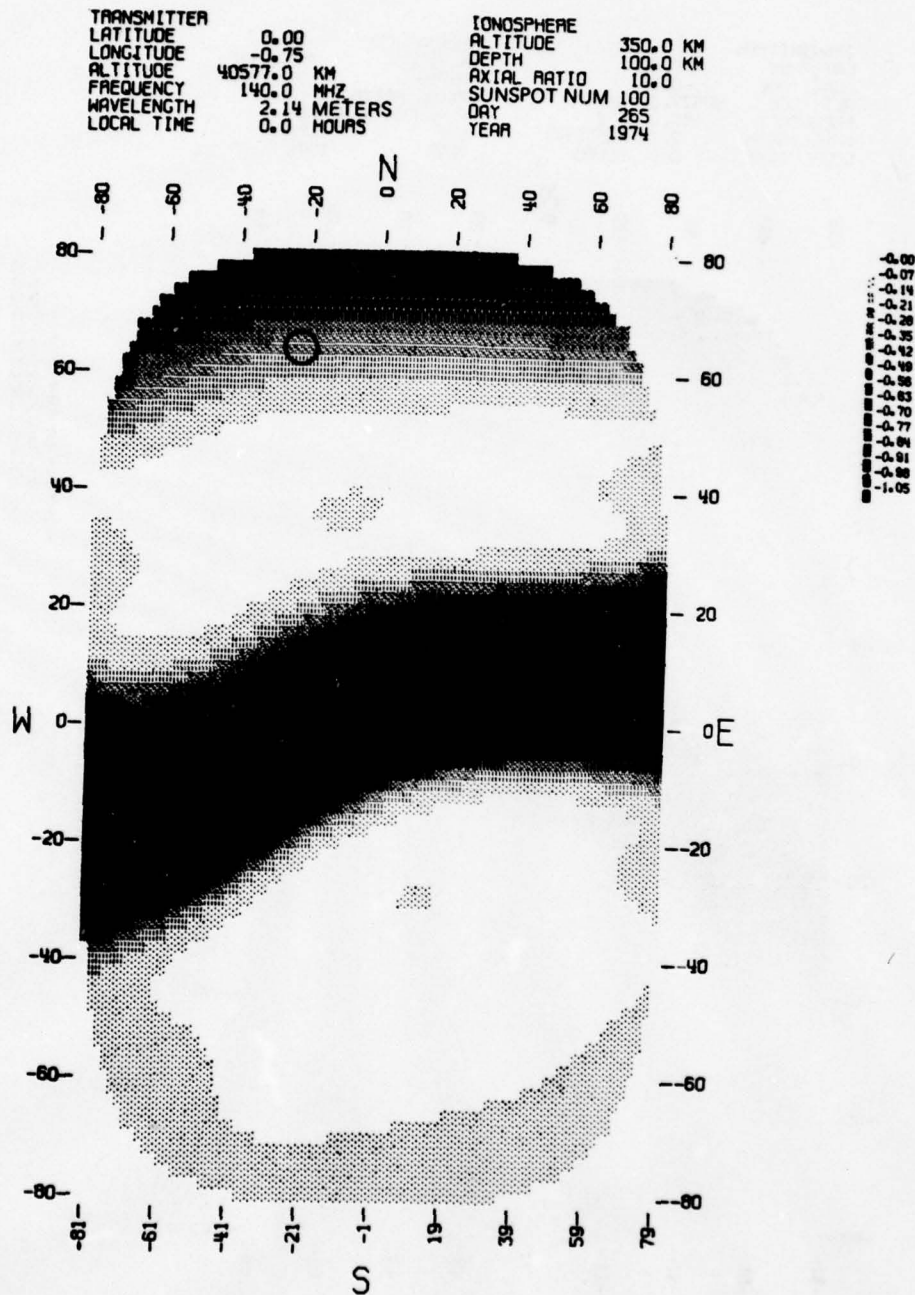


Fig. 44 - Scintillation index map (sunspot number = 100; autumnal Equinox). The center of the circle is the approximate location of Keflavik, Iceland (23°W, 65°N).

We recall that the range of observed S_4 values was 0.13 to 0.17. Using the S_4 function (for all data groups averaged and for past values of R_z) found in Table 15; that is

$$S_4 = 0.15 + 5.69 \times 10^{-4} R_z, \quad (6)$$

and noting that R_z is approximately 23, we have $S_4 \approx 0.16$. Thus Eqs. (5b) and (6) are consistent. Therefore we take

$$S_4 = 0.05 + 4.8 \times 10^{-3} (\Sigma K_p)_F + 5.7 \times 10^{-4} (R_z)_p, \quad (7)$$

where the F stands for the format 4 case (future, or following) and p stands for the format 1 case (past, or preceding). If R_z and ΣK_p are zero, then S_4 is approximately 0.05 as a baseline according to Eq. (7). This corresponds to a fading depth of 0.2 dB on an rms basis.

Percentage Occurrence of Scintillation Index Values

Figure 45 indicates the percentage of time specific ranges of S_4 occurred during the analysis included in this report. Thirty files of data (each lasting 30 min) were analyzed. Breaking the S_4 values into groupings of 0-0.04, 0.05-0.09, 0.10-0.14, 0.15-0.19, 0.20-0.24, 0.25-0.29, 0.30-0.34, etc., we find that the modal value is about 0.15, occurring within 0.10-0.19. If however we examine the low-elevation (summer) and higher elevation (equinoctial) percentages separately, we find the former mode to be within the grouping 0.05-0.09 and the latter mode to be within 0.15-0.19. On the other hand the range of values for the summer data is greater (0.05-0.34) than the equinoctial data (0.10-0.29).

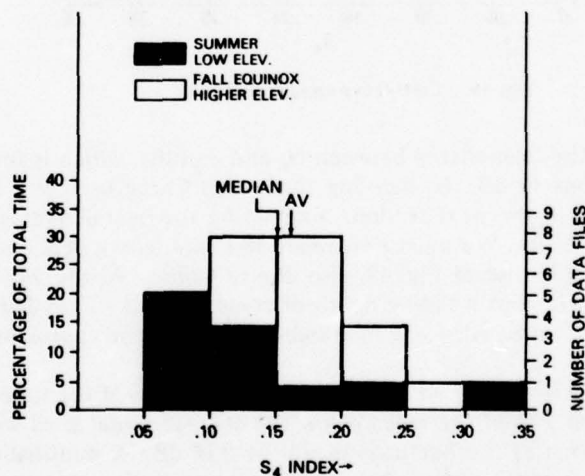


Fig. 45 - Scintillation-index distribution

Figure 46 is a cumulative version of Fig. 45. To interpret Fig. 46 in terms of link availability, one must know the fading level below which corrupted data become intolerable to the mission of the system. To assist in doing this, we shall refer to curves presented by Crane*.

*R.K. Crane, "Ionospheric Scintillation" (invited paper), Proc. IEEE, Feb. 1977, pp. 180-199.

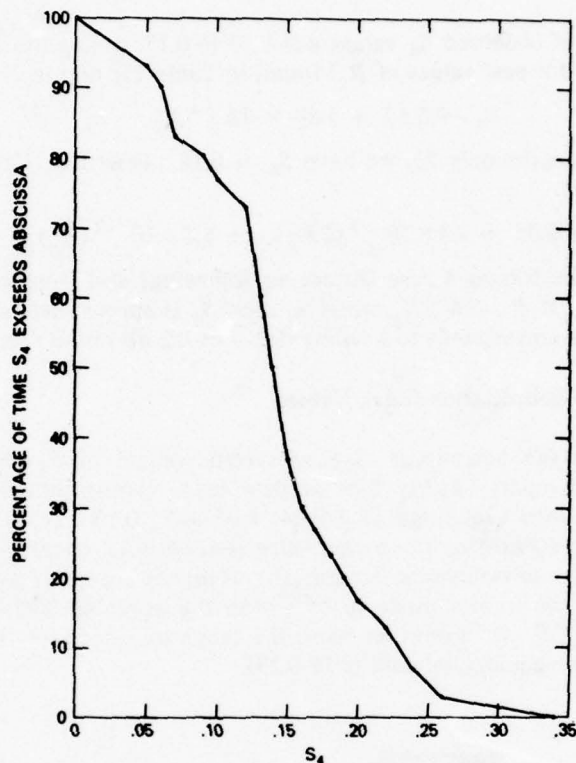


Fig. 46 - Cumulative version of Fig. 45

Figure 47 shows the relationship between S_4 and σ_x (dB), which is the standard deviation of the power fluctuations in dB. In deriving this curve Crane used the Nakagami-m model, which will be discussed in the next section. Examining the overall average S_4 of 0.15 dB, we note that σ_x (dB) \approx 0.75 dB. We must now relate this to a fading depth with a specific probability. This is facilitated by use of Fig. 48, also due to Crane. At the 99% level an S_4 of 0.15 dB or a σ_x (dB) of 0.75 implies a fading depth of roughly 2 dB. Thus fades of 1.8 dB will be exceeded only 1% of the time. Also, the total fading range will be approximately 3.5 dB.

In the present data inventory an S_4 of 0.15 will occur 37% of the time, and (from Figs. 47 and 48) during this time 99% of the fades below the average signal level will be less than 2 dB and the standard deviation of the fluctuations will be 0.75 dB. A scintillation index $S_4 \approx 0.25$ occurs 7% of the time in the current data inventory, and during this time 99% of the fades below the average signal level will be less than approximately 3 dB and the standard deviation of the fluctuations will be roughly 1.2 dB. However the fading range will be somewhat in excess of 6 dB.

Table 16 lists the S_4 index, σ_x (which is the standard deviation in log received power (dB)), the SI index, the 1%-99% fading range (dB), the 1% fading depth, (dB), and the estimated fading depth (dB) derived from

$$SI \text{ (dB)} \approx 10 \log (1 - SI) \quad (8)$$

for the lowest, average, and the peak values of S_4 observed in the current analysis. Evidently the result of Eq. (8) refers to the fading depth near the 1% level. It does not apparently refer to the fading range, even though the prescription for deducing SI is based on an examination of maximum and minimum values.

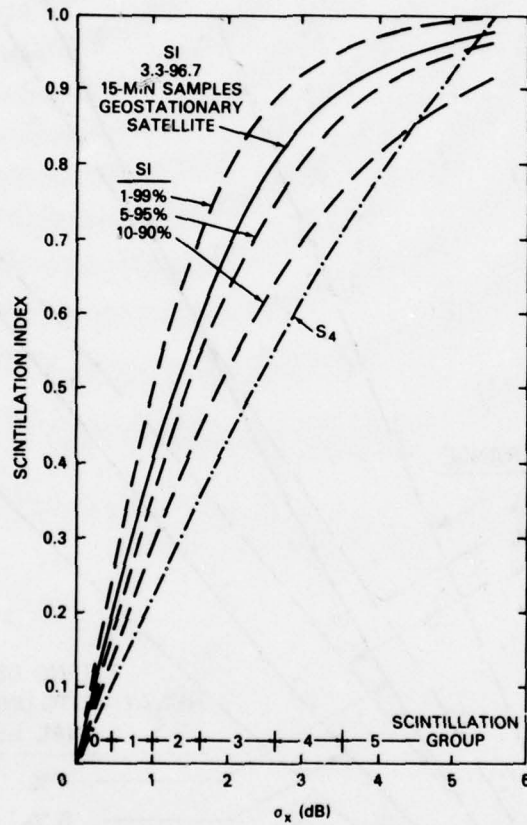


Fig. 47 - Scintillation index versus σ_x (dB) [From R.K. Crane, "Ionospheric Scintillation" (invited paper), Proc. IEEE, Feb. 1977, pp. 180-199.]

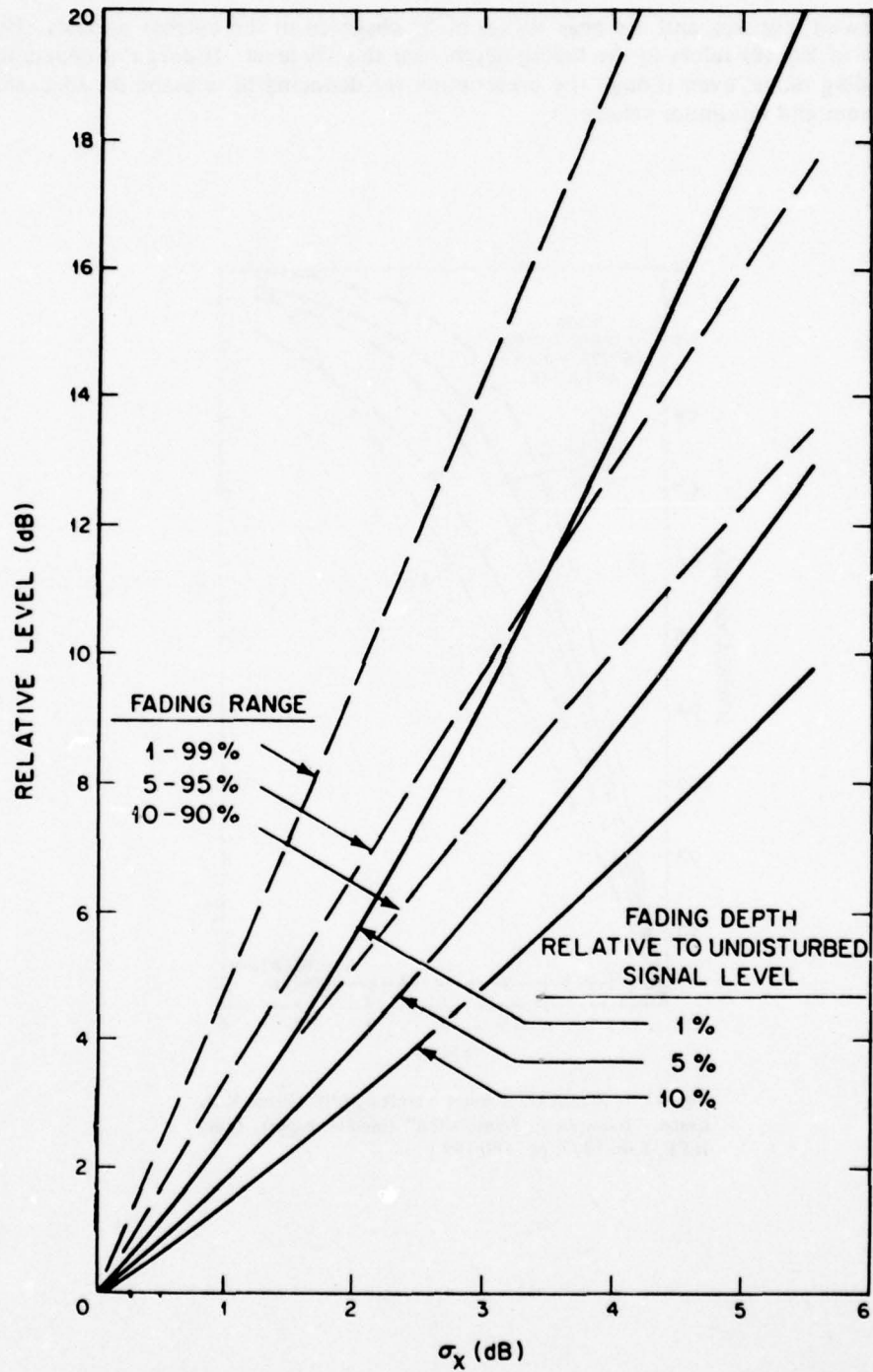


Fig. 48 - Fading level (dB) versus σ_x (dB) [From R.K. Crane, "Ionospheric Scintillation" (invited paper), Proc. IEEE, Feb. 1977, pp. 180-199.]

From Table 16 the peak S_4 of 0.34 corresponds to an SI of 0.68. (Clearly $SI \approx 2S_4$, as indicated in an earlier section.) This yields a fading range (at the 1-99% level) of 4.1 dB. The estimation of σ_x and SI, etc., were based on a model to be discussed in the next section and are accurate only in that context. Also, the values of fading depth in the last column from Eq. (8) are in good (but not excellent) agreement with the fading-depth values in the second-last column. The difference may result from human error in reading Crane's charts.

Table 16 - Observations

Condition	S_4	Occurrence (%)	σ_x (dB)	SI (1-99%)	1-99% Fading Range (dB)	1% Fading Depth (dB)	10 log (1 - SI) (dB)
Minimum S_4	0.05	3	0.25	0.14	1.0	0.6	0.7
Average S_4	0.15	37	0.75	0.35	3.5	1.8	1.9
Peak S_4	0.34	3	1.6	0.68	7.5	4.1	4.9

The worst observed condition ($S_4 = 0.34$) occurred approximately 3% of the total time, and during this time only 1% of the fades exceeded 4.1 dB (second-last column) or 4.9 dB (last column). If hypothetically a system default threshold were -4 dB, then corrupted behavior would occur at the rate of approximately 1/2 min/day using the value in the second-last column.

Amplitude Distribution

A number of workers have noted that although the Nakagami-m distribution is not theoretically justifiable for amplitude scintillation, it is a reasonably good fit to the experimental data.*† If r is the received signal voltage level, the Nakagami distribution is given by

$$P(r) = \frac{2m^m r^{2m-1}}{\Gamma(m) (r^2)^{-m}} e^{-mr^2/r^2}, \quad (9)$$

where m is a parameter and $\Gamma(m)$ is the gamma function. In terms of power p we have‡

$$P(p) = \frac{m^m (p/p_0)^{m-1}}{\Gamma(m)} e^{-mp/p_0}, \quad (10)$$

where p and p_0 are the instantaneous and average received powers respectively.

*R.K. Crane, "Morphology of Ionospheric Scintillation" MIT Lincoln Laboratory Technical Report 1974-29, 21 May 1974.

†H.E. Whitney, J. Aarons, R.S. Allen, and D.R. Seemann, "Estimation of the Cumulative Amplitude Probability Distribution Function of Ionospheric Scintillation," Radio Science 7, 1085-1104 (1972).

‡E.A. Bucher, "UHF Satellite Communication During Scintillation," MIT Lincoln Laboratory Technical Note 1975-10, 5 Aug. 1975.

Figure 49 shows the probability of fading depth for Nakagami- m fading. Rayleigh fading is given by the curve $m = 1$. In this case Eq. (10) reduces to

$$P(p) = e^{-p/p_0}. \quad (11)$$

The variance of p/p_0 for Rayleigh fading is clearly unity; in general it is

$$\text{var} \left(\frac{p}{p_0} \right) = \sigma^2 \left(\frac{p}{p_0} \right) = \left(\frac{\sigma_r}{p_0} \right)^2 = \frac{1}{m}. \quad (12)$$

Because

$$S_4 = \frac{\sigma_p}{p_0}, \quad (13)$$

then

$$m = \frac{1}{S_4^2}. \quad (14)$$

Since the Nakagami- m distribution depends only on m , it is a convenient relation to employ in estimating the effects on systems if only the value of S_4 is known, which often is the case. Figure 50 (similar to Fig. 47, both being due to Crane (1976 paper)) shows the relationship between S_4 and σ_x for log-normal and Nakagami- m models of scintillation. For weak scatter there is little difference. During the current study the data group averages (30 min to 3 hr long) ranged between 0.08 and 0.2; and the file averages (30-min segments) ranged between 0.05 and 0.34. Hence the range of m values for all 30-min segments was 400 to 8.65. Obviously the observed fading was not close to being Rayleigh-like at 360 MHz.

Figure 51 is a typical amplitude distribution obtained by Crane (1976 paper). Clearly the UHF scintillation is essentially log-normal for the data he has analyzed. In general the log-normal distribution is indistinguishable from the Nakagami- m distribution for small scintillation indices. From Fig. 50 the Rayleigh limit at $m = 1$ occurs at $\sigma_x \approx 5.6$ dB. For the present data in which the S_4 values ranged between 0.05 and 0.34, σ_x ranged between 0.25 and 1.6 dB, which is clearly non-Rayleigh.

The SI index is not readily derivable in general measured values of S_4 or σ_x , since the prescription for its determination leaves unanswered the question of the number of independent samples. But if this number is known, and if the Nakagami- m model is employed, one may relate S_4 with the index SI. However for geostationary satellite observations such as the ones described in this report, the number of independent samples is difficult to assess. Each file is 30 min long, and, assuming an irregularity drift velocity of 10^2 m/s and a Fresnel-zone radius (at 360 MHz and at a ray-path distance of 1000 km) of 10^3 m, we have an independent sample every 10 s, or 180 independent samples per file. Since the prescription for SI involves finding the third highest peak and the third lowest minimum, we observe a data range of 1.67 to 98.33%. The SI values alluded to in Table 16 were not deduced from the data directly; they were ascertained from Crane's curves under the assumption of Nakagami- m fading at approximately the 1%-99% assumed level. With the geophysical and geometrical conditions just imposed, such an assumption is justifiable.

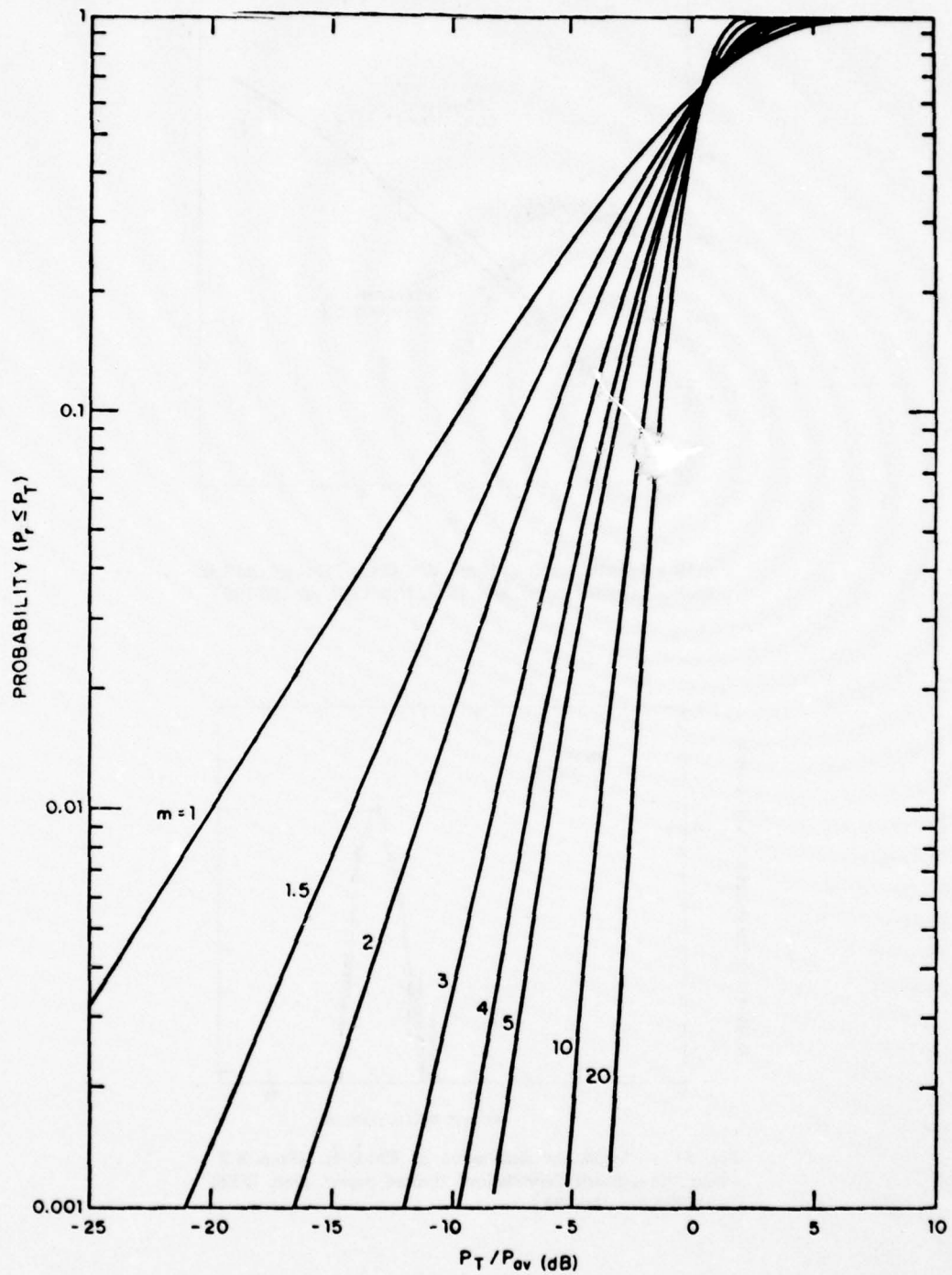


Fig. 49 - Nakagami-m distribution [From E.A. Bucher, "UHF Satellite Communication During Scintillation," MIT Lincoln Laboratory Technical Note 1975-10, 5 Aug. 1975.]

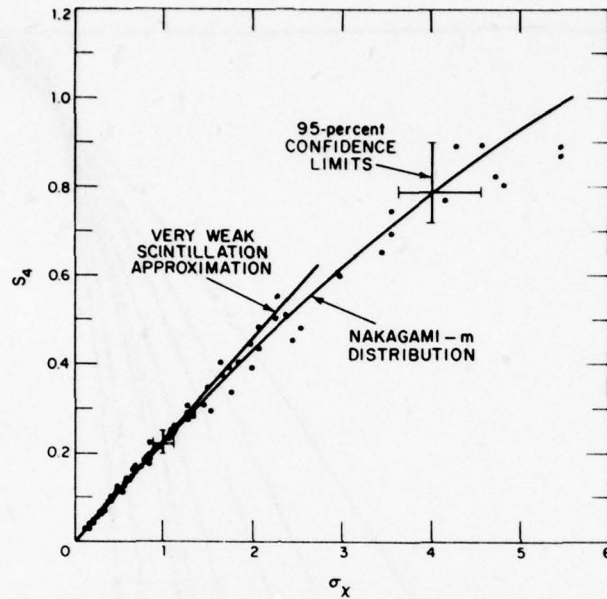


Fig. 50 - S_4 index versus σ_x [From R.K. Crane, "Ionospheric Scintillation" (invited paper), Proc. IEEE, Feb. 1977, pp. 100-199.]

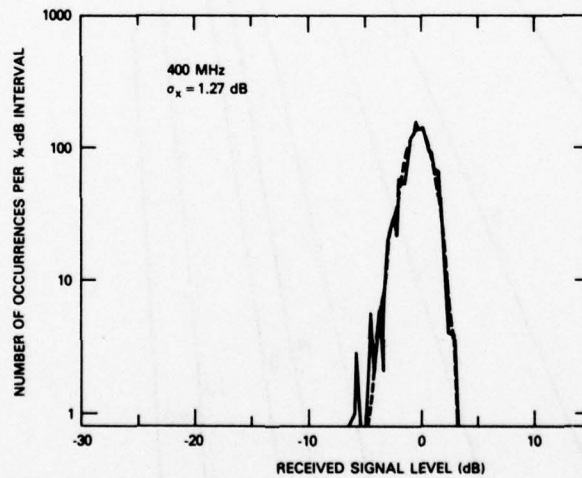


Fig. 51 - Amplitude distribution at 400 MHz. [From R.K. Crane, "Ionospheric Scintillation" (invited paper), Proc. IEEE, Feb. 1977, pp. 180-199.]

Shown in Fig. 52 are the amplitude probability-density functions for the S_4 groups: 0.30-0.34, 0.25-0.29, 0.20-0.24, 0.15-0.19, 0.10-0.14, and 0.05-0.09. Shown in Fig. 53 are the corresponding cumulative distribution functions. For convenience all curves are superimposed. Fixed probability levels (say 10^{-3}) intersect the distributions at values of P_i/P_{av} (dB) roughly in proportion to the S_4 group. The first two groups (0.30-0.34 and 0.25-0.29) contain only one file (30-min segment) each. Hence general conclusions cannot be reached. From inspection of the curves and review of Fig. 49, many of the distributions approximate a Nakagami-m behavior. Nevertheless there are some striking dissimilarities. For example there is an anomalous occurrence of deep fades in data group 2 (reel 20, file 2, for which $S_4 = 0.34$), data group 3 (reel 20, file 5, for which $S_4 = 0.12$), and data group 4 (reel 21, file 12, for which $S_4 = 0.26$). These fades occurred at a 10^{-3} level of probability and were between 12 and 15 dB deep. Hence they occurred for approximately 2s out of 30 min. Furthermore this statistic is valid on three files out of 30, or 10% of the total analysis time.

Rino and Fremouw* have shown for weak scatter that the first-order statistics for amplitude are non-Rician and are best described by a general Gaussian distribution but that the log-normal distribution provides an equally good fit to VHF amplitude data over the equator. They conclude that in general the Nakagami-m distribution of amplitudes is a poorer approximation. They remark that log-normal statistics would be expected near the scattering medium if the complex phase is Gaussian. However the amplitude statistics would be expected to be altered as a result of free-space propagation. They conclude that for *system applications* the log-normal distribution should be used rather than the Nakagami-m distribution. It is important to realize though that the *general* Gaussian hypothesis provides a better understanding of the underlying physics.

The viewpoint of Rino and Fremouw does not have universal acceptance and requires more intensive testing. Whitney et al.,* for example, showed good agreement between measured distribution of ionospheric scintillation and the Nakagami-m distribution. More recently excellent agreement during a 1974 test of equatorial 250-MHz scintillation amplitudes has been obtained.†

Crane‡ tested the use of the Nakagami-m distribution as an approximation to the empirical amplitude distribution obtained at 400 MHz as suggested by Bischoff and Chytil§. Neither the log-normal nor the Nakagami-m distribution were found to be good fits to the data during quiet conditions, although the Nakagami-m distribution provided the best fit when $S_4 \approx 1.0$ and also produced the best agreement with the observed relationship between σ_x (dB) and S_4 over the whole range of S_4 values. For S_4 less than 0.4, there is little difference between the two at either VHF or UHF. The test of the Nakagami-m distribution by Rino and Fremouw was conducted using equatorial data at VHF for which $S_4 \approx 0.5$.

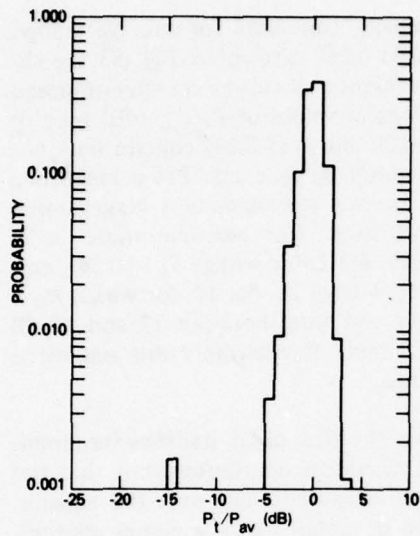
*C.L. Rino and E.J. Fremouw, "Statistics for Ionospherically Diffracted VHF/UHF Signals," *Radio Science* 8, 223-233 (Mar. 1973).

*H.E. Whitney, J. Aarons, R.S. Allen, and D.R. Seaman, "Estimation of the Cumulative Amplitude Probability Distribution Function of Ionospheric Scintillation," *Radio Science* 7, 1085-1104 (1972).

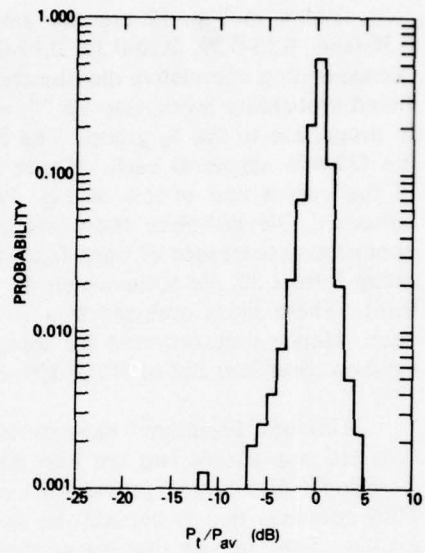
†H.E. Whitney and J. Aarons, "Amplitude Scintillation Observations and System Application," AGARDGRAPH 173, NATO AGARD mtg. on Radio Systems and the Ionosphere, 1976.

‡R.K. Crane, "Morphology of Ionospheric Scintillation," AIAA paper 74-52, Washington, D.C., Jan.-Feb. 1974.

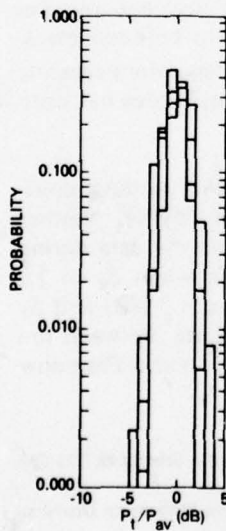
§K. Bischoff and B. Chytil, "A Note on Scintillation Indices," *Planet. Space Sci.* 17, 1059-1066 (1969).



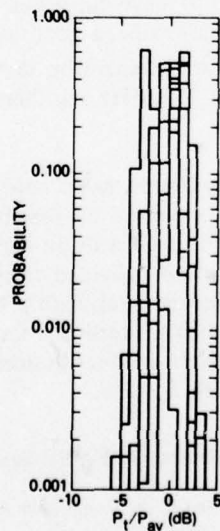
(a) $S_4 > 0.30$



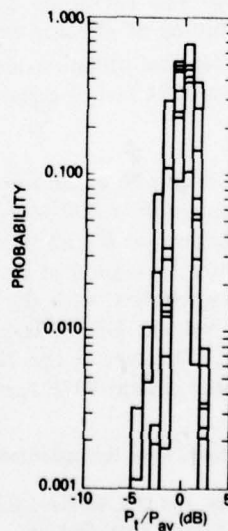
(b) $0.25 < S_4 < 0.29$



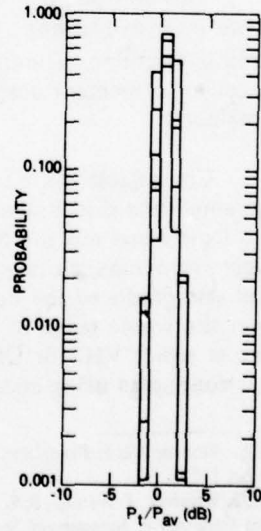
(c) $0.20 < S_4 < 0.24$



(d) $0.15 < S_4 < 0.19$



(e) $0.10 < S_4 < 0.14$



(f) $0.05 < S_4 < 0.09$

Fig. 52 - Probability density of fade levels. Curves for several files are superimposed in (e) through (f).

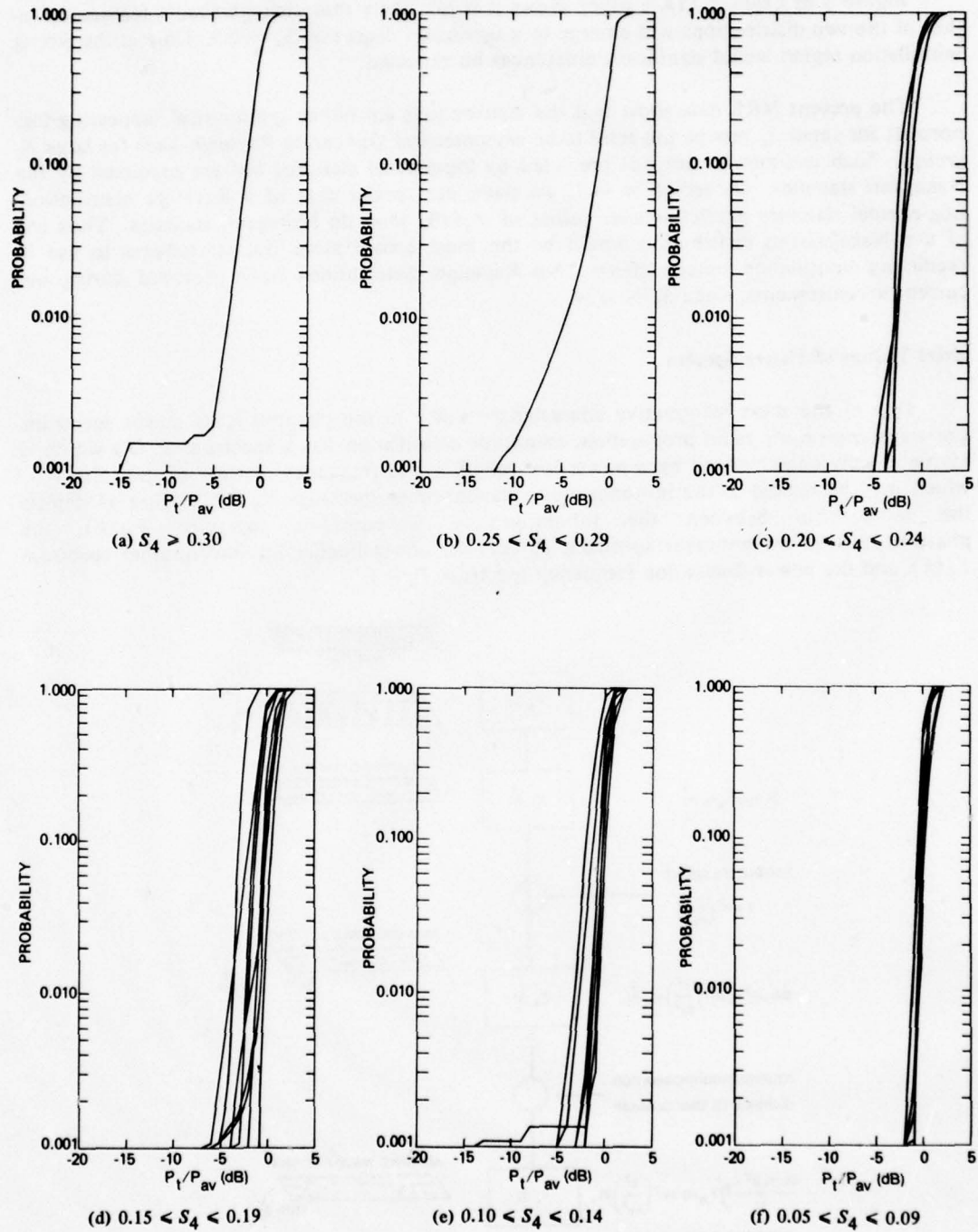


Fig. 53 - Cumulative amplitude distributions corresponding to Fig. 52

Figure 5 of Crane's ALAA paper shows it is not likely that distinguishable features of either of the two distributions will emerge to a significant degree at $S_4 \approx 0.5$. Only at the strong scintillation region would significant differences be expected.

The present NRL data show that the distributions are rather symmetrical (appearing log-normal) for small S_4 groups but tend to be asymmetrical (appearing Rayleigh-like) for large S_4 groups. Such asymmetries are not predicted by log-normal statistics but are predicted by the Nakagami statistics. Indeed if $m = 1$, we have the special case of a Rayleigh distribution. Log-normal statistics predict smaller values of σ_x (dB) than do Nakagami statistics. Thus use of the Nakagami-m distribution would be the most conservative (safest) scheme to use in predicting scintillation outage effects. No Rayleigh distributions were observed during our current measurements, since $S_4 \leq 0.34$.

Brief Theory of Power Spectra

One of the most informative characteristics of a fading channel is its power spectrum. For transionospheric radio propagation, amplitude scintillation has a spectrum $P_s(\nu)$ which is asymptotically characterized by a power-law rolloff in the frequency domain of the form ν^{-n} which may be related to the inhomogeneity wavenumber spectrum $P_N(k)$. Figure 54 depicts the relationship between the inhomogeneity wavenumber spectrum $P_N(k)$, the phase-fluctuation wavenumber spectrum $P_\phi(k)$, the power-fluctuation wavenumber spectrum $P_s(k)$, and the power-fluctuation frequency spectrum $P_s(\nu)$.

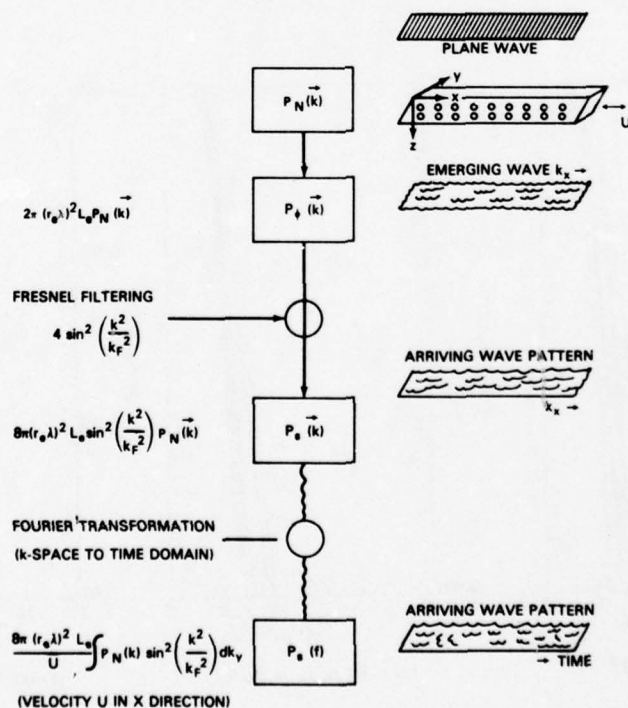


Fig. 54 - Relationship between the irregularity wavenumber spectrum and the resultant power spectrum

The power spectrum for phase fluctuations using the thin-screen approximation is*

$$P_{\phi}(k_x, k_y) = 2\pi (r_e \lambda)^2 L_e P_N(k_x, k_y, k_z = 0), \quad (15)$$

where r_e is the classical electron radius, λ is the radio wavelength, L_e is the irregularity layer thickness, k_x and k_y are the wavenumber coordinates perpendicular to the ray path, and k_z is the wavenumber coordinates along the ray path. Thus $P_{\phi}(k_x, k_y)$ is determined with respect to the center of the irregularity slab in this approximation ($z = 0$). As would be expected, $P_{\phi} \approx P_N \lambda^2$ at the screen. It is convenient to consider the scintillation spectrum $P_s(k)$ as the resultant of an interference pattern produced as the emerging wave traverses the distance from the thin phase screen to the observing screen. Near the screen the interference pattern is not fully developed; far from the screen the reverse is true. Figure 55 depicts in a simplistic way the near-zone and far-zone effects. For a characteristic (outer) scale Λ_o located at distance z from the observer, the zones may be defined as*

$$\begin{aligned} \text{Near Field:} & \quad 0 < (\Lambda_F/\Lambda_o) < 10^{-1}, \\ \text{Transition Field:} & \quad 10^{-1} < (\Lambda_F/\Lambda_o) < 10^1, \\ \text{Far field:} & \quad 10^1 < (\Lambda_F/\Lambda_o) < \infty, \end{aligned}$$

where $\Lambda_F = \sqrt{\pi \lambda z}$ is the Fresnel radius of a radiowave with wavelength λ .

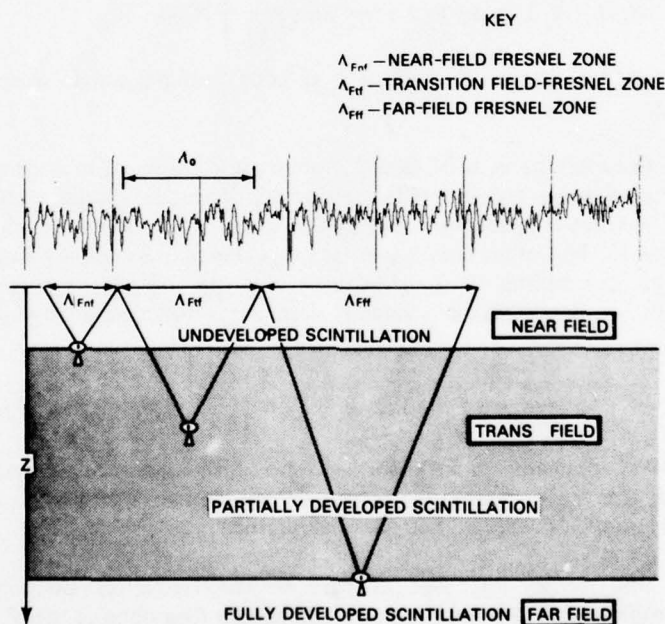


Fig. 55 — Relationship between a characteristic scale Λ_o and the near-field and far-field effects

*C.L. Rufenach, "Ionospheric Scintillation by a Random Phase Screen," Radio Science **10**, 155-165 (Feb. 1975).

*C.L. Rufenach, "Wavelength Dependence of Radio Scintillation: Ionosphere and Interplanetary Irregularities," J. Geophys. Res. **79** (10), 1562 (Apr. 1974).

As the distance to the thin screen diminishes, the Fresnel zone contracts as \sqrt{z} . The interference due to nonrectilinear propagation (diffraction) will be small if $\Lambda_F \ll \Lambda_0$; the interference will be complete if $\Lambda_F \gg \Lambda_0$.

The compensation for the discrepancy in the phase-scintillation and amplitude-scintillation spectra is obtained by including a Fresnel filtering factor

$$F = 4 \sin^2 \left(\frac{k^2}{k_F^2} \right),$$

where

$$k^2 = k_x^2 + k_y^2$$

and

$$k_F^2 = \left(\frac{2\pi}{\Lambda_F} \right)^2 = \frac{4\pi}{\lambda z}.$$

Thus the scintillation spectrum is written

$$P_s(k_x, k_y) = 8\pi (r_e \lambda)^2 L_e \sin^2 \left(\frac{k^2}{k_F^2} \right) P_N(k_x, k_y). \quad (16)$$

Therefore the scintillation spectrum in k space is directly proportional to the inhomogeneity wavenumber spectrum.

In practice the observations of scintillation spectra are referenced to a time domain, since single-fixed-station experiments are generally conducted. Thus we obtain a mapping of only one coordinate in wavenumber space (say K_x) as the irregularity screen moves across the ray path at a fixed velocity U . The other coordinate (say k_x) affects the mapping but is mathematically removed through integration. If it is assumed that the irregularity screen moves with respect to the ray path (or vice versa) at a velocity U in the x direction, it is possible to rewrite Eq. (16) as*

$$P_s(\nu) = \frac{8\pi L (r_e \lambda)^2}{U} \int P_N(k_x, k_y, 0) \sin^2 \left[\frac{\lambda z}{4\pi} (k_x^2 + k_y^2) \right] dk_y. \quad (17)$$

This is a general relation applicable to both isotropic and anisotropic inhomogeneities. Only k_x and k_y play a role in the power spectrum, as the z dependence is embodied in the Fresnel filtering term $\sin^2[\dots]$ and P_N is evaluated at the phase screen.

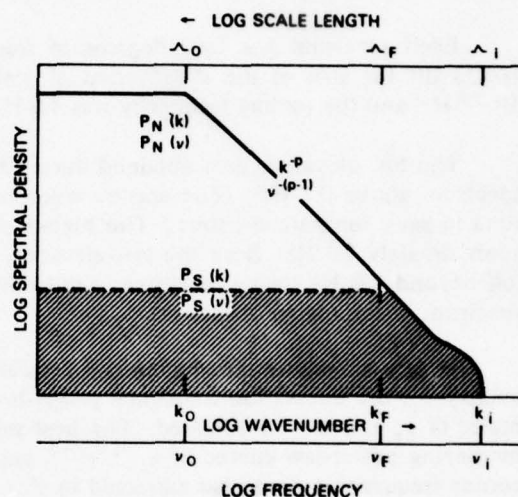
In performing this translation from k space to the frequency domain, the Fourier transformation was employed on the temporal autocorrelation functions of the $P_s(k)$ pattern as it traversed a prescribed observation point. Just as the Fresnel-zone distance was a convenient benchmark on the wavenumber spectrum, the Fresnel-zone frequency is the requisite parameter for the power spectrum:

$$\nu_F = \frac{U}{\sqrt{\pi \lambda z}}. \quad (18)$$

*D.G. Singleton, "Power Spectra of Ionospheric Scintillations," J. Atmos. Terrest. Phys. **36**, 113-133 (1974).

If a fluctuation frequency component is examined in the domain $\nu < \nu_F$, its value is found to be attenuated by Fresnel filtering. In fact the so-called corner frequency ν_c (where $\nu_c = \nu_F/\sqrt{\pi}$) theoretically defines the separation between a constant-spectral-density domain ($\nu < \nu_c$) and a power-law region ($\nu > \nu_c$). Ott* indicates that the medium appears "homogeneous" for $\nu < \nu_c$, since all irregularities in this domain fill the first Fresnel ellipsoid. On the other hand, if $\nu > \nu_c$, then a full range of irregularities moves through the first Fresnel ellipsoid. Figure 56 illustrates the concept of Fresnel filtering.

Fig. 56 - Hypothesized power spectrum. $P_N(k)$ is the inhomogeneity wavenumber spectrum, $P_N(\nu)$ is the frequency spectrum associated with $P_N(k)$, $P_S(k)$ and $P_S(\nu)$ are the power spectra in k space and the frequency domain respectively, Λ_0 is the outer scale dimension and ν_0 is the corresponding frequency, Λ_i is the inner scale dimension and ν_i is the corresponding frequency, Λ_F is the Fresnel dimension and ν_F is the corresponding frequency, and p is the power-law index.



The implications of Eq. (17) depend on the nature of the inhomogeneity wavenumber spectrum. For elongation in the x direction (the direction of inhomogeneity drift), the spectrum $P_N(k)$ will decrease very slowly with increasing k_y relative to k_x . For elongation in the y direction, the reverse is true. In the latter case (y -axis elongation) the $\sin^2[\dots]$ term, being controlled by k_x , may be removed from the integral and give rise to modulated spectra. In the former case (x -axis elongation) the $\sin^2[\dots]$ term is dominated by k_y in the domain for which the integrand is nonvanishing. Hence it must remain beneath the integral sign, and the modulation is averaged out. The Fresnel filtering term

$$\sin^2 [\dots] = \sin^2 \left[\frac{(k_x^2 + k_y^2) \lambda z}{4\pi} \right]$$

may produce modulation only above the Fresnel frequency ν_F , but it is extremely important below ν_F , where it attenuates the scintillation power. Hence modulated spectra would be expected under only special conditions—principally when the direction of motion is perpendicular to the semimajor axis of the irregularities (anisotropic case). Since irregularities are generally thought to be field aligned and since irregularity drift velocities are often east-west, this condition may often exist in nature. Isotropic spectra will not give rise to modulation in the power spectra observed, since the $\sin^2[\dots]$ term fluctuates throughout the entire range of k and averages to $1/2$.

*R.H. Ott, "Observed Temporal Amplitude and Phase Spectra From ATS-6 Radio Beacon Experiment at 40, 140, and 360 MHz," Radio Sci. 12 (2), 319 (Mar.-Apr. 1977).

Bessel spectra will produce extrema for isotropic spectra.

Scintillation Spectra Obtained at Keflavik

Fast-Fourier-transform spectra of the 30 files of data are presented in Fig. 57. Figures 57a through 57g are montages of the separate data groups 1 through 7. Figure 57h contains the data groups 8 through 10; these were obtained during the premidnight period on 1 Oct. 1976 (a single group) and the postmidnight period on 2 Oct. 1976 (two additional groups).

Each spectrum has four degrees of freedom, providing a spectral estimate stability of ± 4.33 dB for 80% of the distribution of estimates.* The resolution was approximately 5×10^{-3} Hz, and the folding frequency was 3.0 Hz.

The low-elevation data obtained during the summer had a noise floor which limited the spectrum above 0.2 Hz. (The spectra were averaged beyond the 0.3 Hz frequency in all the runs to save computation time.) The higher elevation data *did not* exhibit a noise floor out to approximately 2.0 Hz. Both the low-elevation and higher elevation data exhibited a steep rolloff beyond 3.0 Hz owing to system bandwidth characteristics imposed to reduce aliasing the spectrum in the region of interest.

With a view toward deducing any possible relationships between the so-called corner frequency ν_c , the fluctuation-frequency power-law index n , and the parameters ΣK_p and S_4 , estimates of ν_c and n were obtained. The best estimates of these two quantities were deduced by overlaying power-law curves of ν^{-1} , ν^{-2} , and ν^{-3} on the spectra presented in Fig. 57. The corner frequencies were also extracted in this operation by examination of the low-frequency departure from power-law behavior. Table 17 depicts the results and the average values of ν_c and n .

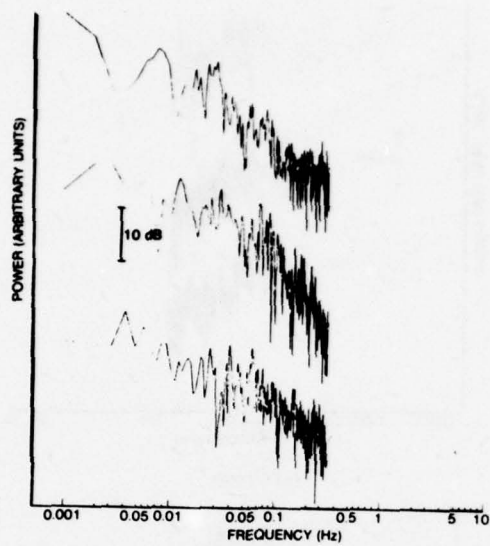
A correlation analysis was also performed on the data listed in Table 17. The values for R_z were from format 1 (past 24 hours), and those for ΣK_p were from format 4 (future 24 hours). These formats were deemed the most appropriate in that they provided the most reasonable (and significant) results. Table 18 lists the regression lines and correlation coefficients.

The index n is not correlated with anything to any significant degree. Also, the relationship between ν_c and S_4 is insignificant. The only two regression lines which may be regarded as having some degree of statistical significance are those which relate ν_c and ΣK_p and ν_c and R_z . In these two instances there is less than a 45% chance that the observed correlations would have been extracted from a random population.

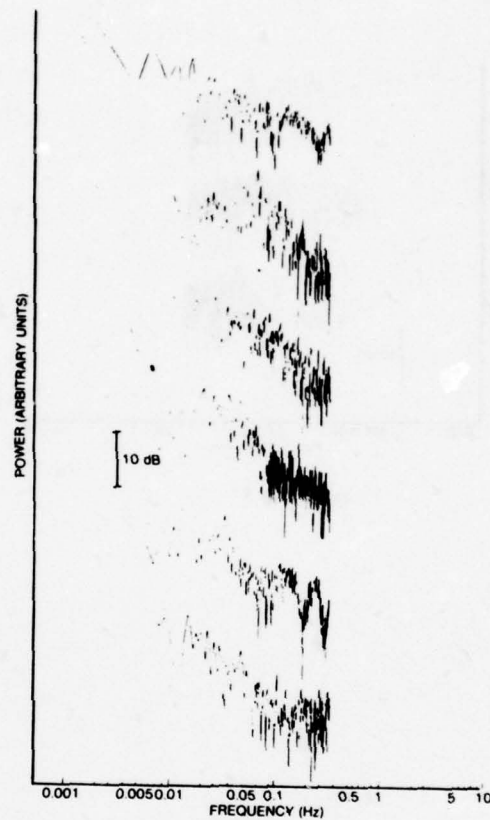
Rufenach and Pope* have suggested that ν_c is related to K_p at HF. They found that the correlation between K_p and ν_c was 0.63 with a high degree of confidence (they had 75 data points in comparison with ten in the NRL data presented here). This figure is close, perhaps fortuitously, to the NRL value of 0.66.

*R.B. Blackman and J.W. Tukey, *The Measurement of Power Spectra*, Dover, 1958.

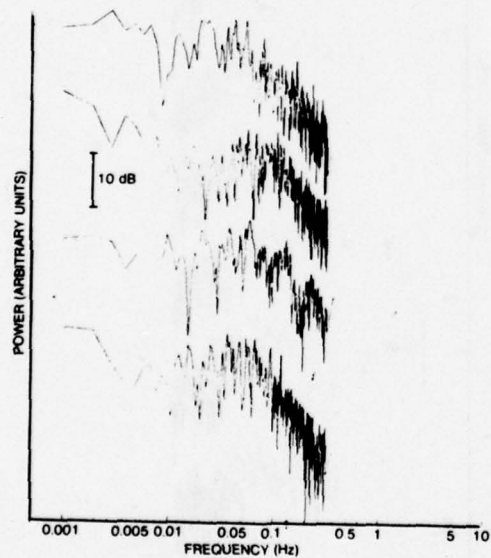
*C.L. Rufenach and J.H. Pope, "Interpretation of Single-Site Scintillation Measurements to Estimate F-Region Drift Velocities," *Planet. Space Sci.* 23, 560-562 (1974).



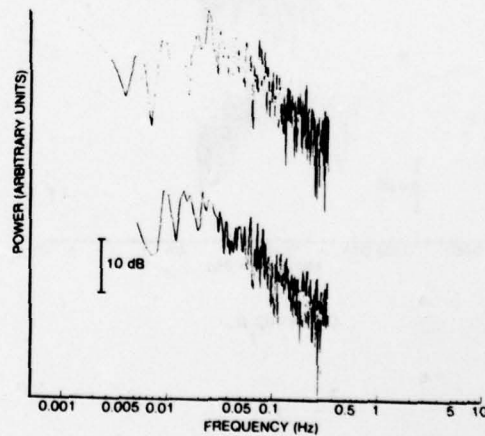
(a) Group 1



(c) Group 3



(b) Group 2



(d) Group 4

Fig. 57 - Power spectra

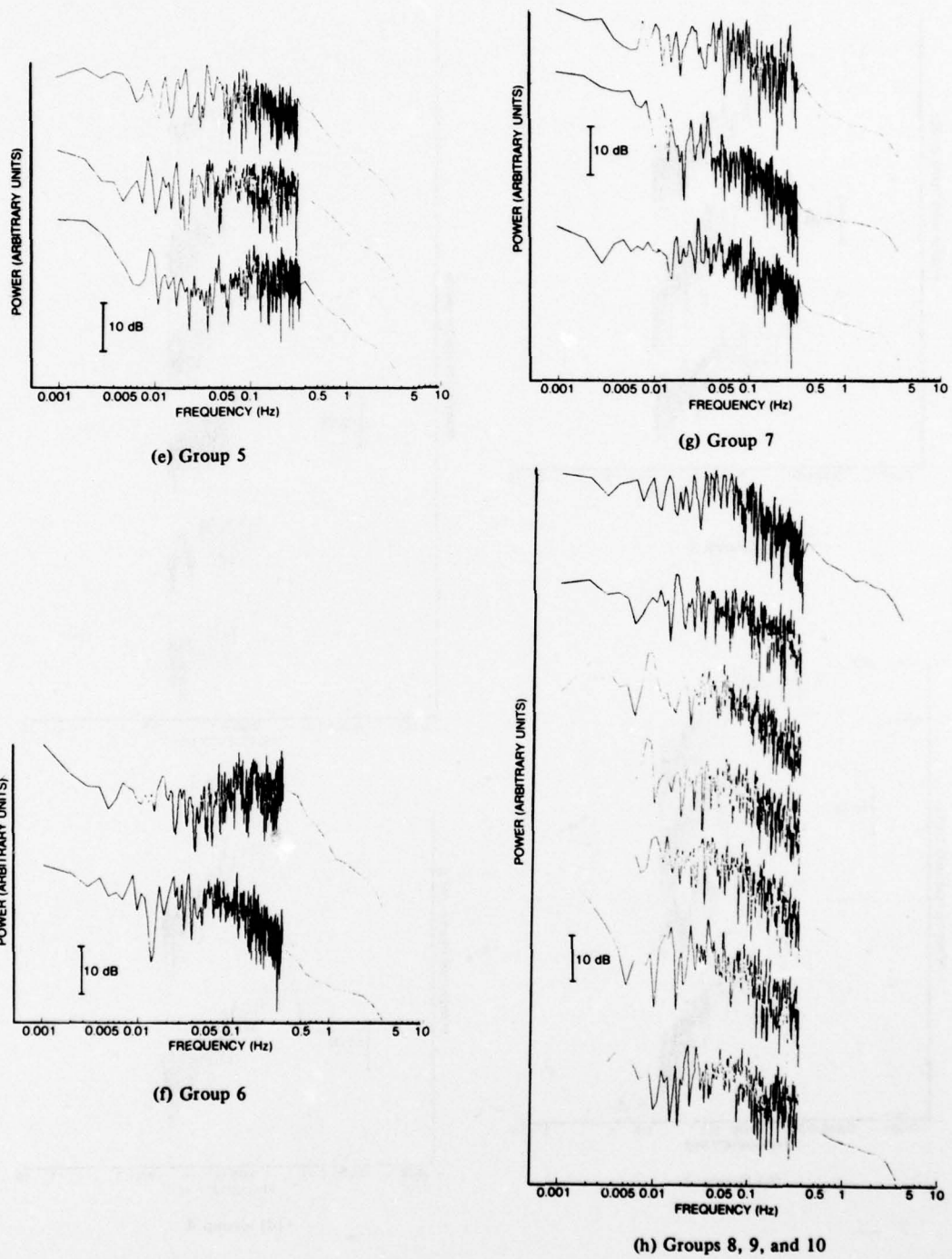


Fig. 57 (Continued) - Power spectra

Table 17 - Results Obtained From Fig. 57

Group	$\bar{\nu}_c$	\bar{n}	\bar{S}_4	$\Sigma k_{p,4}$	$R_{z,1}$
1	0.06	2.3	0.12	19+	23
2	0.05	2.4	0.20	26-	26
3	0.03	1.9	0.08	14-	19
4	0.22	2.2	0.20	30	7
5	0.09	1.7	0.13	20+	16
6	0.02	2.0	0.20	16+	25
7	0.03	2.0	0.18	21	31
8	0.05	1.8	0.15	25+	31
9	0.06	1.5	0.16	25+	31
10	0.07	1.8	0.18	25+	31

Since the Fresnel frequency is

$$\nu_F = \frac{U}{\sqrt{\pi \lambda z}}, \quad (19)$$

where U is the drift velocity, and

$$\nu_c \approx \frac{1}{\sqrt{\pi}} \nu_F, \quad (20)$$

we have

$$\nu_c \approx \frac{U}{\sqrt{\lambda z}}. \quad (21)$$

Taking $\sqrt{\lambda z} = 10^3$, we may deduce the drift velocity U from the values of ν_c in the current data base. For $\bar{\nu}_c \approx 0.067$ Hz we have that $U \approx 200$ m/s. Also from Table 18

$$U = 314 + 24 \Sigma K_p, \text{ for } \Sigma K_p \geq 14. \quad (22)$$

If $\Sigma k_p < 14$, negative values of U result which have no physical significance. If $\Sigma K_p \leq 16$, then the average 3-hourly K index is ≤ 2 . Our range of values for ΣK_p were 14- to 30; hence quiet magnetic activity was not sampled. Using the average ΣK_p of ≈ 20 and inserting this into Eq. (22), we find $U \approx 166$ m/s, which is close to the value $\bar{U} = 200$ m/s obtained directly from $\bar{\nu}_c$. Hence we regard Eq. (22) as a reasonable indicator of horizontal drift velocity as a function of magnetic activity.

It is well known that if the intrinsic inhomogeneity wavenumber spectrum is given by k^{-p} , then the fluctuation frequency (power) spectrum will vary as $\nu^{-(p-1)}$, leading to a radio-frequency dependence of $f^{-n} = f^{-(p-1)/2}$ for the scintillation index S_4 . Often the n exponent is seen to be in the range of $2 \leq n \leq 5$, with $n \approx 3$ taken as an average. Some support for an n value of 3 has been derived from in-situ measurements of the inhomogeneity spectral index. Ott, observing 360-MHz transmission from ATS-6 (as in the current study), found three sets of values for S_4 , n , and the corner frequency ν_c . In Table 19 the averages are compared with the NRL results.

Table 18 - Results of Correlation Analysis on the Data of Table 17

Parameters	Regression	Correlation	P* (%)
ν_c, n	$\nu_c = 2.1 \times 10^{-3} + 0.036n$	+0.17	87
ν_c, S_4	$\nu_c = 0.01 + 0.38S_4$	+0.27	81
$\nu_c, \Sigma K_p$	$\nu_c = 0.10 + 7.6 \times 10^{-3} \Sigma K_p$	+0.66	44
ν_c, R_z	$\nu_c = 0.20 - 0.01R_z$	-0.74	27
n, S_4	$n = 1.66 + 1.85S_4$	+0.27	81
$n, \Sigma K_p$	$n = 1.86 + 4.7 \times 10^{-3} \Sigma K_p$	+0.08	>90
n, R_z	$n = 2.22 - 0.01R_z$	-0.31	74

*Probability of observation of given correlation from a random sample.

Table 19 - Comparison of the 360-MHz Results at Keflavik by NRL With 360-MHz Results at Boulder by R.H. Ott*

Location	$\bar{\nu}_c$ (Hz)	\bar{n}	S_4
Keflavik (NRL)	0.067	2.0	0.15
Boulder (Ott)	0.04	2.37	0.08

*R.H. Ott, "Observed Temporal Amplitude and Phase Spectra From ATS-6 Radio Beacon Experiment at 40, 140, and 360 MHz," Radio Sci. 12 (2), 319 (Mar.-Apr. 1977).

The NRL values of ν_c and \bar{n} are comparable with the results obtained from Boulder. However the values of S_4 were greater at Keflavik than at Boulder. This is likely due to the difference in elevation angles, although it could also be due to geographical differences.

If n is the average exponent defining the power-law rolloff in the spectra, as would appear to be the case, then the three-dimensional inhomogeneity spectral index p is 3. Thus the radio-frequency law for S_4 is f^{-1} rather than $f^{-1.5}$ as usually supposed. The present result predicts more substantial scintillation at the higher frequencies than does the conventional law.

Scintillation Spectra and the S_4 Index

Figure 58 shows how the scintillation index varies with increasing fluctuation frequency. The scintillation-index calculation is strongly influenced by the system margin, and care must be taken to deduce S_4 using only those fluctuation frequency components which are not contaminated by tape or system noise. Figure 59 is an actual calculation of S_4 versus ν ; also shown is the specific S_4 density per elementary frequency band. Most of the spectral power is contained below 0.1 Hz, that is, in periodicities which are greater than 10 s. Indeed half of the scintillation index is provided by frequencies less than 0.03 Hz, or periodicities in excess of 33 s. The cumulative distribution fits an exponential law of the form

$$S_4(\nu) = S_4(1 - e^{-\lambda\nu}), \quad (23)$$

where λ is the exponential slope factor. In Fig. 59, $\lambda = 20$ s. This corresponds to the upper bound of all periodicities, or lower bound of all frequencies, for which S_4 is reduced to $1 - (1/e)$, or 63%, of the maximum value. This may be corroborated by inspection of Fig. 59.

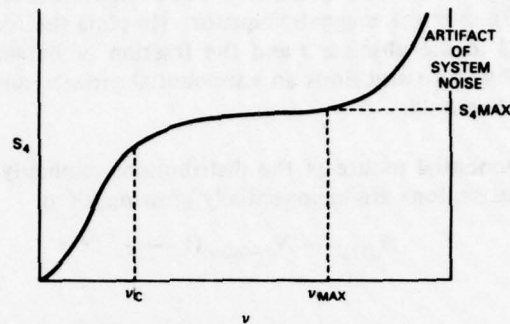


Fig. 58 - Simulated plot of the S_4 index versus fluctuation frequency ν

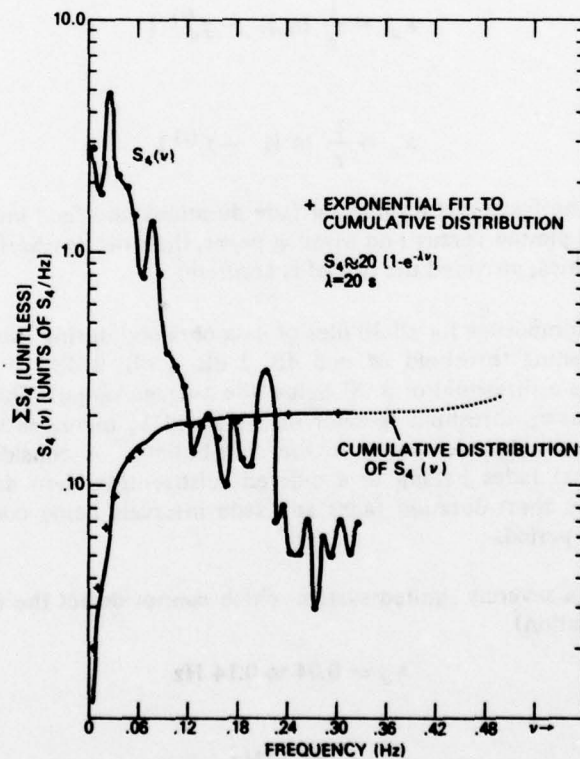


Fig. 59 - Actual plot of the S_4 index per elementary frequency band versus ν . The cumulative distribution of $S_4(\nu)$ asymptotically approaches S_4 .

Fading Statistics

There is some justification to suppose that the fade-duration and fading-interval distributions are exponential. Bucher* has postulated such distributions and found that they are reasonable for 250 MHz over the magnetic equator. He plots the fraction of fades having duration less than or equal to the abscissa t and the fraction of between-fade time intervals less than or equal to the abscissa t and finds an exponential growth curve for each distribution for fixed values of fading threshold.

To show the exponential nature of the distributions explicitly, a different presentation is used herein. If the distributions are exponentially growing, then

$$N_d(t) = N_{d-max} (1 - e^{-\lambda_d t}) \quad (24)$$

and

$$N_i(t) = N_{i-max} (1 - e^{-\lambda_i t}), \quad (25)$$

where N_{d-max} and N_{i-max} are the maximum number of fades and of fade intervals observed during the observation period, and λ_d and λ_i are the corresponding exponential exponents. Thus it may be shown that

$$\lambda_d = \frac{1}{t} \ln [1 - f_d^{(t)}] \quad (26)$$

and

$$\lambda_i = \frac{1}{t} \ln [1 - f_i^{(t)}], \quad (27)$$

where f_d and f_i are the fractional number of fade durations and fade intervals respectively. If $1 - f_i$ and $1 - f_d$ is plotted versus t on semilog paper, then the λ 's will appear as slopes of resultant straight lines, provided the model is accurate.

Figures 60 are composites for all 30 files of data obtained during the Keflavik experiments for fixed values of fading threshold $M = 3$ dB, 2 dB, 1 dB, 0 dB, -1 dB, -2 dB, and -3 dB (where +3 dB implies a threshold of 3 dB below the average signal). The graphs show that λ_d decreases with decreasing threshold (greater margin) and λ_i increases with decreasing threshold. There is also considerable scatter to the distributions. A considerable fraction of the short-duration (≤ 4 s) fades belong to a different distribution than do the longer duration fades—the λ 's for the short-duration fades and fade intervals being considerable larger than the λ 's for the longer periods.

For $M = 2$ dB (a severely limited system which cannot detect the downcoming signal in the absence of scintillation),

$$\lambda_d \approx 0.04 \text{ to } 0.14 \text{ Hz}$$

and

$$\lambda_i \approx 2.3 \text{ Hz.}$$

*E.A. Bucher, "UHF Satellite Communication During Scintillation," MIT Lincoln Laboratory Tec. Note TN 1975-10, 5 Aug. 1975.

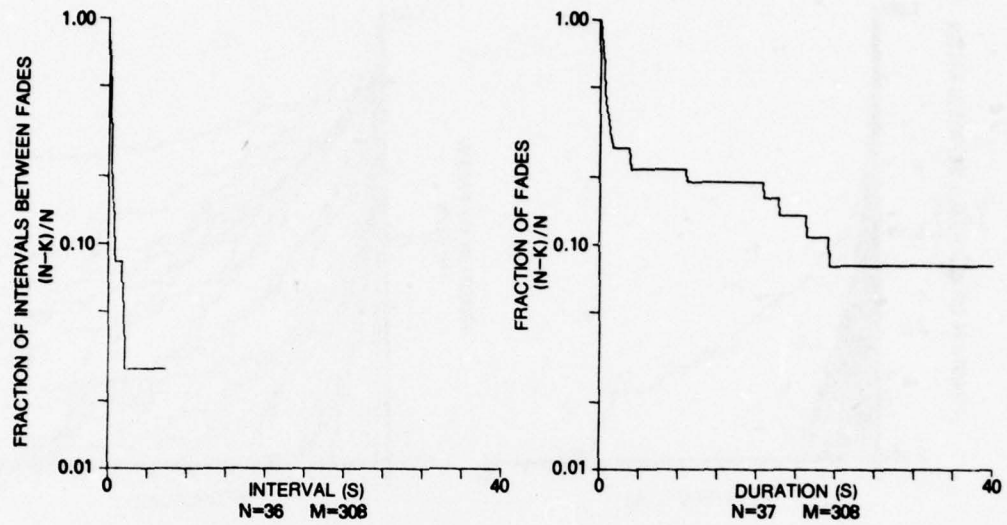


Fig. 60a - Fade-interval and fade-duration distributions for a threshold of $M = +3$ dB

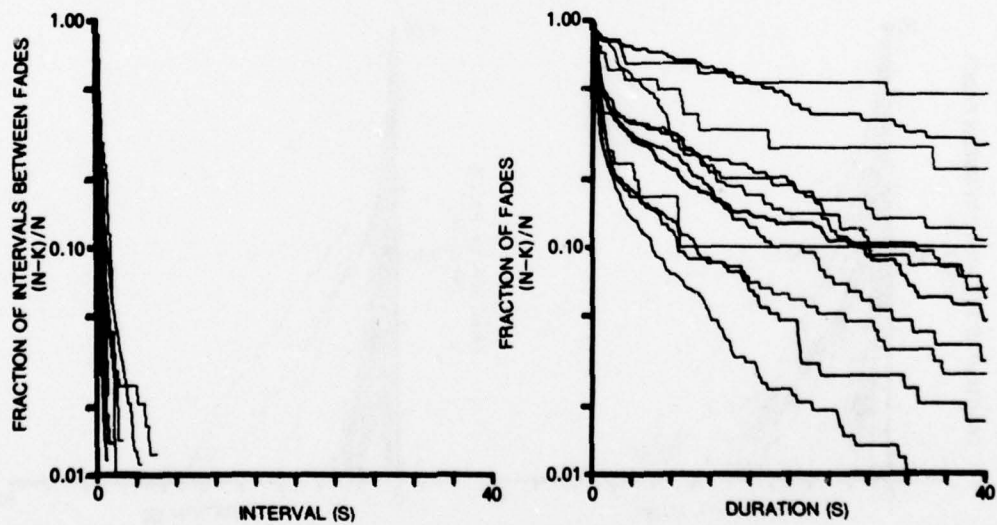


Fig. 60b - Fade-interval and fade-duration distributions for a threshold of $M = +2$ dB

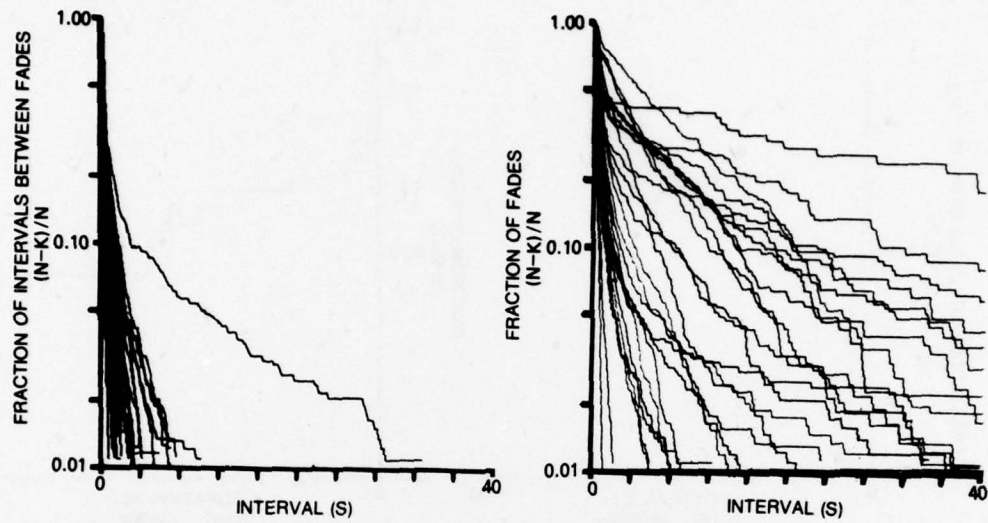


Fig. 60c - Fade-interval and fade-duration distributions for a threshold of $M = +1$ dB

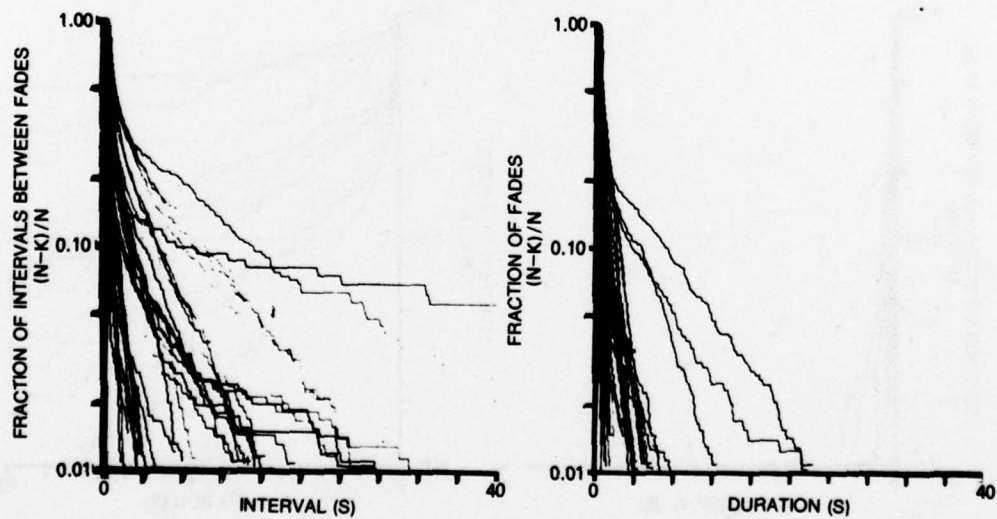


Fig. 60d - Fade-interval and fade-duration distributions for a threshold of $M = 0$ dB

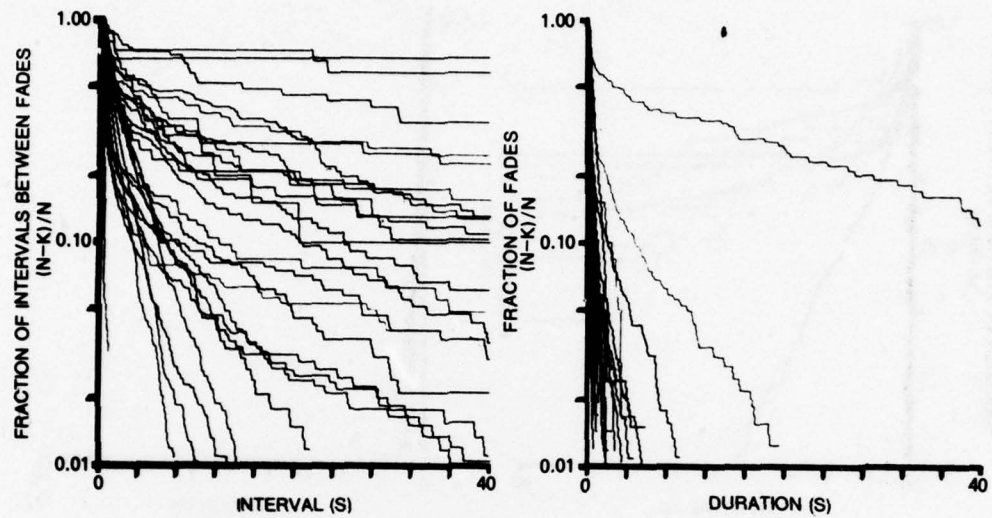


Fig. 60e - Fade-interval and fade-duration distributions for a threshold of $M = -1$ dB

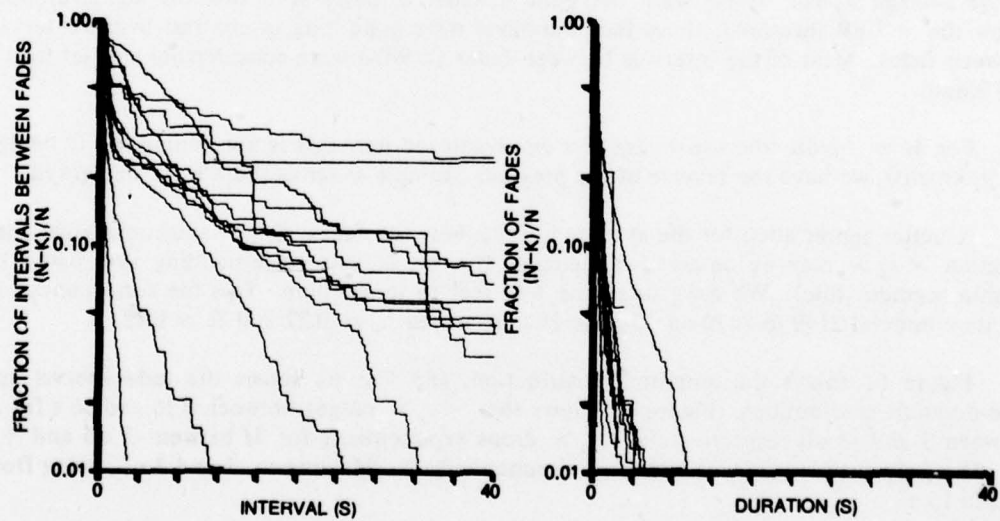
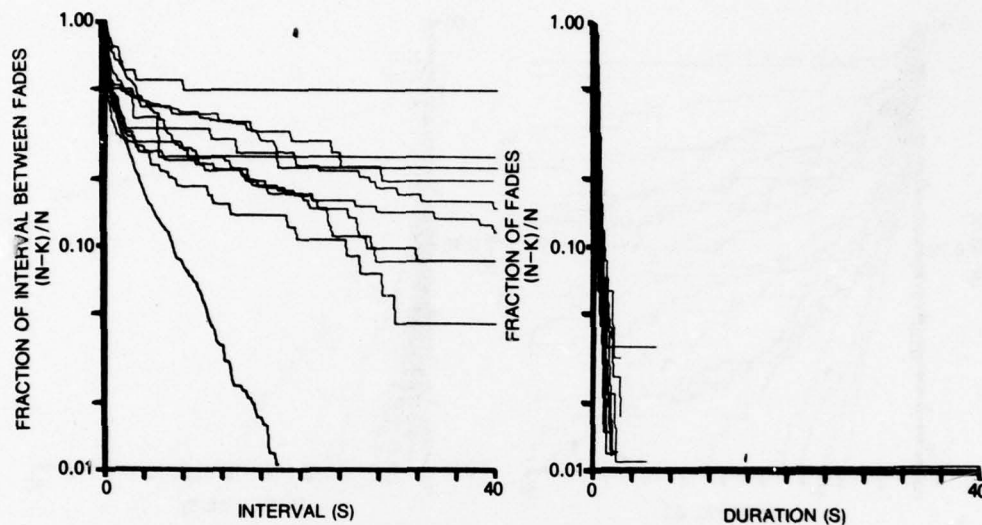


Fig. 60f - Fade-interval and fade-duration distributions for a threshold of $M = -2$ dB

Fig. 60g - Fade-interval and fade-duration distributions for a threshold of $M = -3$ dB

These values correspond to the "bandwidths" of the *fades* or *intervals between fades* respectively. Scintillation occurrences will allow communication for short intervals. For an average 30-min file of data obtained at Keflavik, there were 160 intervals for which the signal rose above 2 dB of the average signal. There were the same number of fades such that the signal dropped below the +2-dB threshold; these fade durations were quite long in contrast to the intervals between fades. Most of the intervals between fades ($\approx 90\%$) were considerably smaller than 1 s in length.

For $M = -2$ dB (the usual case of a disadvantaged user that is not limited in the benign environment), we have the reverse of the previous example as far as the λ 's are concerned.

A better appreciation for the average interval between fades $\langle t_i \rangle$ and the average fade duration $\langle t_d \rangle$ may be obtained by looking at a set of data corresponding to a particular 30-min segment (file). We have taken file 4 of reel 16 to examine. This file corresponded to the time interval 2149 to 2220 on 23 June 1976 in which $S_4 \approx 0.22$ and $SI \approx 0.42$.

Figure 61 shows the amplitude distribution, and Fig. 62 shows the fade-interval and fade-duration distributions. Figure 63 shows that $\langle t_i \rangle$ ranges between 0.36 and 36 s for M between 3 and -3 dB respectively; $\langle t_i \rangle$ drops exponentially for M between -3 dB and +1 dB. The fade duration $\langle t_d \rangle$ increases exponentially for M between -1 and 3 dB, going from 0.45 to 15 s.

Figure 64 is a plot of the number of fades for $M = 0$ and -2 dB as a function of fade duration for the three files during which the scintillation index was most pronounced (R27F2, where $S_4 \approx 0.24$; R21F12, where $S_4 \approx 0.26$; and R19F2, where $S_4 \approx 0.34$). Plots similar to this have been produced by Deckelman*.

*W.F. Deckelman 1974, "A Digital Simulation of the Statistical Properties of Ionospheric Scintillation," PhD thesis, University of Missouri, 1974.

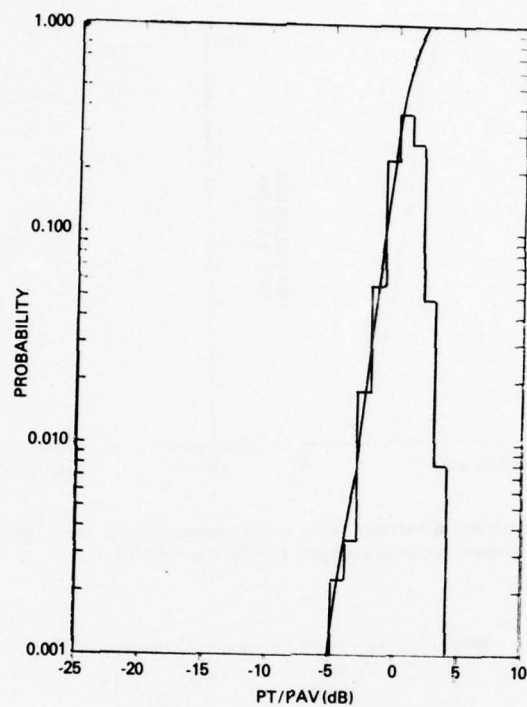


Fig. 61 - Amplitude distribution for file 4 of reel 16

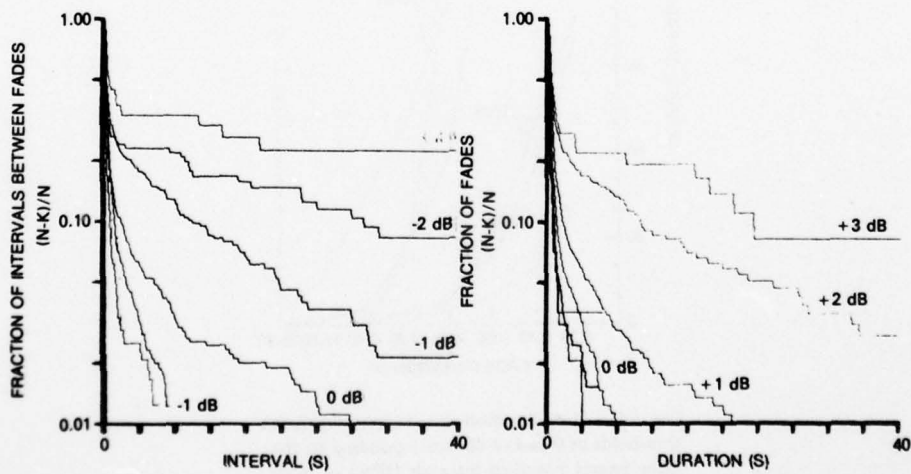


Fig. 62 - Fade-duration and fade-interval distributions for file 4 of reel 16

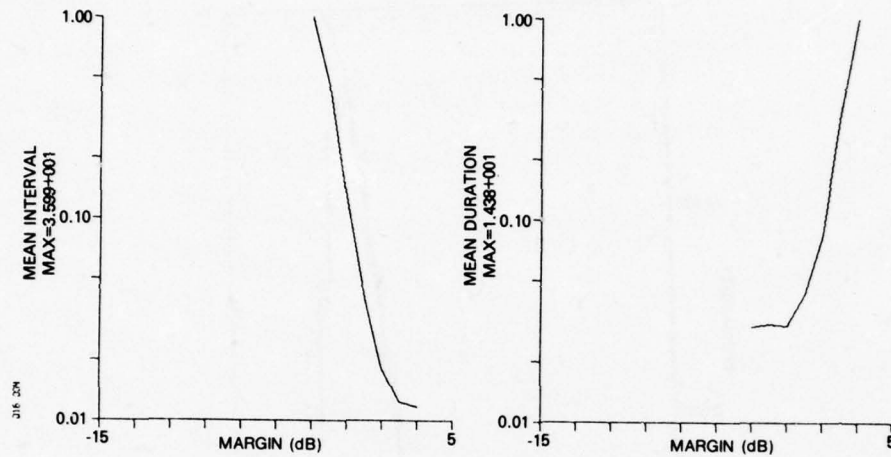


Fig. 63 - Mean interval between fades and the mean fade duration versus system threshold (margin) for file 4 or reel 16.

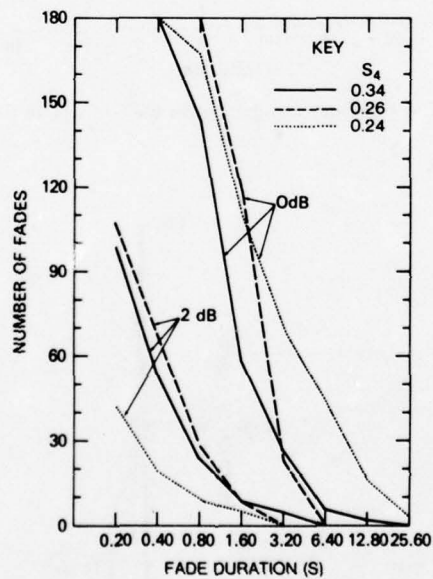


Fig. 64 - Fade-duration distributions for fade thresholds of 0 and -2 dB corresponding to the three largest observed intervals (files) of scintillation

Other Considerations

Because the Keflavik experiments described herein were conducted at such low elevation angles, a few remarks are in order. Castelli et al.* obtained scintillation data for low-elevation transits of radio stars and found that tropospheric scintillation is primarily confined to the first 5° of elevation. Crane† has found that signal-level fluctuations increase significantly at low elevation angles. He has observed ground-reflection problems due to multipath propagation at 400 MHz which produces angle-of-arrival periodicities lasting 5 min and approximately 1 hour. The amplitude scintillation was reduced somewhat due to aperture averaging since a 35-meter antenna was employed.

The question of low-elevation effects has recently been considered by Rees et al.‡ studying ATS-6 transmissions. They found a 5-min quasi-periodicity at 360 MHz which was predominantly a midday/midnight event. They contend that those periodicities are caused by ground reflections.

A periodicity of 5 min corresponds to a frequency of 5×10^{-3} Hz. Reinspection of the power spectra in this report does indicate that there is some texture in the neighborhood of 10^{-2} Hz and below. This problem is being given additional attention.

SUMMARY

An analysis of UHF scintillation data obtained at Keflavik, Iceland, during the summer and the autumn equinox of 1976 has been conducted. The source of radiowave transmissions at 360 MHz was the ATS-6 satellite, which was viewed at an elevation of approximately 5° during the summer and 14 to 16° during the equinox. The overall average S_4 scintillation index was $\bar{S}_4 \approx 0.15$; the average SI scintillation index was found to be roughly $2 \bar{S}_4$. The average standard deviation of S_4 was 0.75 dB, the 1-99% fading range was about 3.5 dB, and the 1% fading depth was approximately 1.8 dB on the average. On the basis of a correlation analysis we suggest the following relationship between S_4 and the parameters ΣK_p and R_z :

$$S_4 = 0.05 + 4.8 \times 10^{-3} (\Sigma K_p) + 5.7 \times 10^{-4} (R_z)_p,$$

where the future values of ΣK_p are used and the past values of R_z are used. Thus magnetic activity is seen to control S_4 more strongly than solar activity.

The amplitude statistics were clearly non-Rayleigh, and for the smaller scintillation levels observed in this study the distributions were roughly approximated by the Nakagami-m model.

The power spectra were characterized by an average corner frequency of 0.067, which suggests an inhomogeneity drift velocity of the order of 200 m/s. The power-law index was observed to be 2.0 on the average. This is somewhat lower than observed by other workers and implies a radio-frequency law for S_4 of the form

*J.P. Castelli, J. Aarons, and H.M. Silverman, "Ionospheric and Tropospheric Scintillations of a Radio Star at Zero to 5 degrees of Elevation," J. Atmospheric Terrest. Phys. 26, 1197-1213 (1964).

†R.K. Crane, "Low Elevation Angle Measurement Limitations Imposed by the Troposphere: An Analysis of Scintillation Observations Made at Haystack and Millstone," MIT Lincoln Laboratory Technical Note TN518, 18 May 1976.

‡P.R. Rees, L. Kersley, and K.J. Edwards, "Ground Reflections and the ATS-6 Radio Beacon Experiment", J. Atmospheric Terrest. Phys. 39, 545-549 (1977).

$$S_4 \propto f^{-1},$$

which suggests rather considerable amplitude scintillation at gigahertz frequencies when S_4 is large at UHF. Most of the energy in the spectrum is contained below 0.1 Hz, which is in the neighborhood of the Fresnel frequency. On the average, 50% of the scintillation power is provided by frequencies less than 0.03 Hz, or by periodicities in excess of 33 s. As a function of fluctuation frequency we suggest the relation

$$S_4(\nu) = S_4(1 - e^{-\lambda\nu}),$$

where λ is an exponential slope factor (seconds) which is related to S_4 . Typically, if $S_4 \approx 0.20$, then $\lambda \approx 20$ s.

The fade-duration and fade-interval distributions are also typically exponential, although some significant departures are observed.

These data were obtained over a relatively short time during rather low solar activity. Furthermore the low elevation angles during the study would be expected to produce some spurious interference effects due to multipath propagation arising because the beam illuminated the earth's surface along with the satellite.

RECOMMENDATIONS

In attempting to extract significant relationships between the various geophysical observables and the scintillation parameters such as S_4 , SI, ν_c , and n , we were handicapped by the insufficient number of data groups which had been analyzed. It is planned to continue the analysis of the raw data on hand to resolve this situation. However additional measurements are required when the solar activity is higher. Anticipated significant enhancements in S_4 during 1978 and the following years will lead to the maximum of the 11-year solar cycle in 1981-1983.

Also, phase-fluctuation data are needed simultaneously with the amplitude data. This is clearly of interest in phase-shift-keying systems even when the amplitude scintillation is modest; for it has been shown that the phase-fluctuation index is always equal to or greater than the amplitude-fluctuation index.

A comprehensive amplitude and phase scintillation program should be started that concentrates on the 200-to-400-MHz frequency band of interest to the NAVELEX PME 106. Data should be obtained at high latitude near the auroral oval (such as at NAVSTA Keflavik), at Middle latitudes (such as at NAVCAMSLANT Norfolk), and in equatorial regions (such as NAVCAMS WESTPAC Guam). Since the systems of interest are generally geostationary, synchronous satellite sources of UHF transmissions should be emphasized. The data-collection program should be coupled with experimental studies ongoing at AFGL, NOSC, MIT/Lincoln Lab, U.S. Army/Fort Monmouth, and elsewhere.

Channel modeling should be expanded and improved to include the new data. A program to synthesize the ionospheric channel at UHF has been initiated at NRL.

For maximum benefit from the comprehensive amplitude and phase scintillation program, steps must be taken to use existing or developing forecasting schemes to ascertain their efficacy in predicting SATCOM outages. Major ingredients in these evolving forecasting technologies include a first-principles modeling of the physics, solar monitoring, and ground-based sensors.